Probing water structure and transport in proton exchange membranes

Probing water structure and transport in proton exchange membranes

ACADEMISCH PROEFSCHRIFT

ter verkrijging van de graad van doctor
aan de Universiteit van Amsterdam
op gezag van de Rector Magnificus
prof. dr. ir. K.I.J. Maex
ten overstaan van een door het College voor Promoties
ingestelde commissie,
in het openbaar te verdedigen in de Agnietenkapel
op vrijdag 2 maart 2018, te 10:00 uur

door Xiao Ling

geboren te Hunan, Volksrepubliek China

Promotiecommissie:

Promotor:	prof. dr. M. Bonn	Universiteit van Amsterdam
Copromotor(es):	dr. K.F. Domke	Max-Planck-Institute für Polymerforschung
	dr. S.H. Parekh	Max-Planck-Institute für Polymerforschung
Overige leden:	dr. K.P. Velikov	Universiteit van Amsterdam
	prof. dr. W.J Buma	Universiteit van Amsterdam
	dr. N.F. Shahidzadeh	Universiteit van Amsterdam
	prof. dr. P. Borri	Cardiff University
	prof. dr. D.R. Dekel	Technion, Israel Institute of Technology

Faculteit der Natuurwetenschappen, Wiskunde en Informatica

Verlag Dietmar Fölbach, Koblenz
ISBN 978-3-95638-854-5

The work described in this thesis was carried out at the Max-Planck-Institute für Polymerforschung (MPIP, Ackermannweg 10 D-55128 Mainz Germany) and was financially supported by the European Commission FP7 (ITN-FINON #607842).

Cover picture: Changbai Mountain in P.R.China was used with the permission of the copyright holder.

Publications covered in this thesis

Chapter 4

X. Ling, M. Bonn, S. H. Parekh, K. F. Domke, "Nanoscale Distribution of Sulfonic Acid Groups Determines Structure and Binding of Water in Nafion Membranes", *Angew. Chem. Int. Ed*, *55*(12), 4011–4015. https://doi.org/10.1002/anie.201600219

Chapter 5

X. Ling, M. Bonn, K. F. Domke, S. H. Parekh, "Heterogeneous water transport in proton exchange membranes", in preparation

Chapter 6

L. M. Ostertag, X. Ling (co-first author), K. F. Domke, S. H. Parekh, M. Valtiner, "Surface density of charged sulfonic acid groups strongly affects hydrophobic forces in confinement", in preparation.

Other publications

A. Farrukh, F. Ashraf, A. Kaltbeitzel, X. Ling, M. Wagner, H. Duran, A. Ghaffar, H. Rehman, S. H. Parekh, K. F. Domke and B. Yameen, " Polymer brush functionalized SiO2 nanoparticle based Nafion nanocomposites: a novel avenue to low-humidity proton conducting membranes", *Polym. Chem.*, 2015, 6, 5782-5789.

C. Jia, Y. Cheng, X. Ling, G. Wei, J. Liu, C. Yan, "Sulfonic poly(ether ether ketone)/functionalized carbon nanotube composite membrane for vanadium redox flow batter applications", *Electrochim. Acta*, 153 (2015) 44-48.

Contents

CHAPTER 1
INTRODUCTION

1.1 Overview

This dissertation presents my results and associated background information from my Ph.D. research on water in proton exchange membranes. My Ph.D. project focused on exploring water structure and transport properties in Nafion® proton exchange membranes commonly used in fuel cell applications. A detailed outline of my thesis is provided below.

- **Chapter 1** provides a background of the project. Firstly, working principles of proton exchange membrane fuel cells (PEMFC) are introduced and the importance of water management in proton exchange membrane (PEM) of PEMFC is addressed. Then, the importance of studying water behavior in PEM and understanding the interplay of membrane structure and water behavior is discussed.
- **Chapter 2** provides a theoretical background of Raman scattering and coherent anti – Stokes Raman scattering (CARS) spectroscopy. The time-domain Kramers-Kronig transform for extracting quantitative Raman-like spectra from CARS spectra is included in this chapter. The algorithm of constrained non-negative least squares, which is used for deducing the spectral signature of an unknown component, is introduced and so is Multivariate Curve Resolution-Alternating Least Squares (MCR-ALS).

- **Chapter 3** includes the details of the Nafion® membranes, materials, and methods used in my Ph.D. project.
- **Chapter 4** discusses the structure and binding of water in Nafion® membranes. Two subspecies of water in Nafion® membranes are identified and spectrally distinguished. One of the water subspecies – bulk-like water – resembles the “normal” bulk water; the other – non-bulk water – is under-coordinated water that interacts directly with the constituents in Nafion® membrane. Our work shows that the fractional contributions of these two water species are determined by the nanoscale distribution of sulfonic acid groups in nanoscale water channels present in Nafion® membranes. The membranes with larger non-bulk water species exhibits larger proton conductivity and higher water mobility.
- **Chapter 5** discusses the heterogeneous water transport in Nafion® membrane. The nonbulk water in the membrane diffuses 5-fold faster than the bulk water. Our results show that the diffusivity of water in Nafion is a linear combination of diffusivity from two water subspecies (non-bulk and bulk). The diffusivity of non-bulk water is significantly faster than that of the bulk water in Nafion® membranes. The mechanism of faster diffusivity of non-bulk water in Nafion® membranes is discussed.
- **Chapter 6** focuses on investigating how the hydrophobic/hydrophilic mixture on the surface of the water channels in Nafion® membranes affects water organization in confinement using a planar model system and atomic force microscopy (AFM). The surface is emulated via self-assembled monolayers where sulfonic acid groups are gradually substituted for hydrophobic moieties. Surface-enhanced Raman scattering is used to characterize the micro-scale homogeneity of the surfaces and AFM is used to

characterize adhesion and the structure of water on the different surfaces at the molecular level.

- **Chapter 7** is a short summary of the future ideas for the follow-up work on this topic in the future.

1.2 Proton exchange membrane (PEM) fuel cells

Fuel cells (FCs), invented by William Robert Grove in 1839, have attracted increasing attention as an alternative renewable power source for applications including the portable power supply, the automobile industry, and stationary power generation. [1] FCs are noise-free in operation and are pollution free as well since water is the only by-product. Energy efficiency of FCs is up to 90% of the overall energy capacity and is much higher than other renewable power systems using solar or wind energy. Proton exchange membrane fuel cells (PEMFCs), operating at a temperature below 100 °C, are one of the most promising FC technologies for the automobile industry. In a PEMFC, hydrogen gas is used as fuel, and the proton exchange membrane (PEM), which serves as an electrolyte, is one of the key components. Application of PEMFC technology reached a milestone in 2014 when Toyota introduced the first PEMFC-powered vehicles to the consumer market. [2] Nevertheless, large-scale commercialization of these vehicles requires further improvement in the PEMFC performance and reduction in the cost, along with appropriate refuelling infrastructure of the H_2. In the following paragraphs, I describe the constitution and working principle of a PEMFC (Figure 1.1), and review the earlier reports on attempts to improve the PEMFC performance.

PEMFCs convert the chemical energy in the form of H_2 into electricity and are constructed by a PEM and two electrodes (anode and cathode). Both electrodes consist of a gas diffusion layer (GDL) and a catalyst layer (CL). H_2 and O_2 gas diffuse through the GDL to their respective CL, and an electro-chemical reaction occurs at each CL. The PEM (electron-isolator) conducts protons and simultaneously prevents the cross-transport of H_2 and O_2. Water is not only a product of the electrochemical reaction at the cathode, but water also plays an important role in PEMFC performance. [3, 4] In a PEMFC, the H_2 is humidified before given as input to the FC. The humidified H_2 provides necessary water content to hydrate the PEM. Here, the relative humidity of the H_2 has to be adjusted to maintain proper functioning of the PEM.

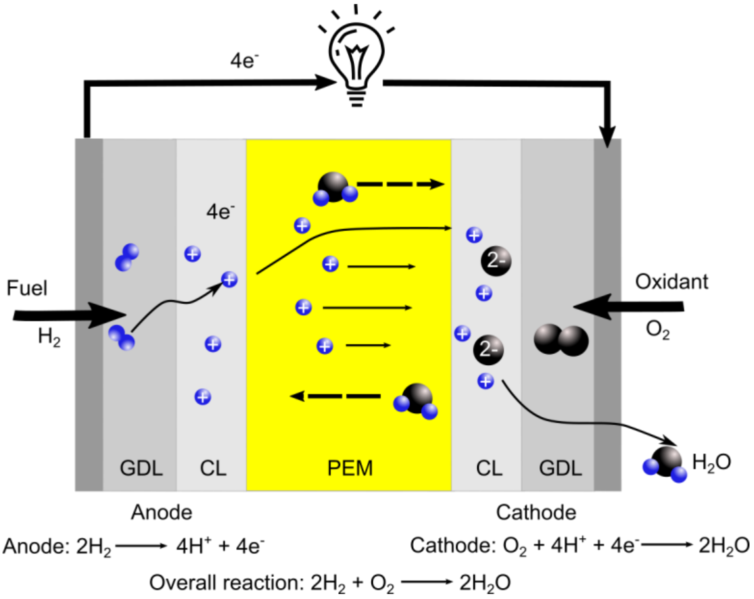

Figure 1.1. Schematic of a PEMFC. GDL and CL are gas diffusion layer and catalyst layer, respectively. The PEM transports protons from the anode to the cathode, and electrons transport through the external circuit driving a current to the load (the bulb). Water is produced at the cathode by recombination of the protons and electron and together with O_2. Transport of water in PEM is driven by the electro-osmotic drag (from the anode to the cathode) and a concentration gradient (from the cathode to the anode).[5]

One has to achieve a water balance in the PEM in order to ensure high proton conductivity and avoid flooding at the cathode. [3] Fast water transport driven by the electro-osmosis drag from the anode to the cathode is necessary for fast proton transport in the PEM, [6] while water transport from the cathode to the anode driven by the concentration gradient has to be efficient enough so that the water flooding at the cathode is suppressed. Ideally, instead of removing the water produced from the cathode, using this water to humidify the PEM can simplify the design of the cathode GDL and can potentially eliminate the cost in humidifying the input gas. Thus, understanding the water transport in PEMs and knowing how the membrane structure determines the water transport is important for designing a PEM with good water balancing ability and self-humidified capability.

1.3 PEM

An ideal PEM exhibits high proton conductivity and a stable chemical and physical structure to ensure long-term use of the PEMFC. As mentioned above, the membrane should also prevent the electron transport and the fuel (H_2) and oxidant (O_2) crossover. Nafion® membranes developed by DuPont Inc. in the 1960s [7] is the benchmark PEM material. Nafion® membranes are widely used in PEMFC because of the outstanding chemical stability compared to other aromatic-aliphatic membranes such as sulfonated poly (ether ether ketone) (SPEEK) [8] and sulfonated poly (ether sulfone) [9]. Hence, Nafion® membranes are the primary material studied in my Ph.D. project. Nevertheless, despite the superior performance of Nafion® membranes to other materials, the water transport in Nafion® membranes need further improvement in order to obtain a larger proton conductivity and maintain a better water balance in the membrane. [10, 11] The structure of the membrane, which determines the water transport, must therefore be modified, and the primary question becomes how to modify the membrane structure. To answer this question, one has to understand the how the membrane structure affects the water transport in the membrane in order to have a clear target for designing a membrane structure with accelerated water transport.

The following sections review the structure, the macroscale property (water transport) and structure and binding of water molecules in the Nafion® membranes. The structure of Nafion® membranes has been extensively studied with small angle X-ray/neutron scattering, and different structural models have been used to interpret these scattering profiles. These models have been used to explain the macroscale property of the membranes and delivered very important information for understanding the nanoscale membrane morphology. Studies on the structure and binding of water molecules in Nafion® membrane, while more scarce, have provided a qualitative understanding of water structure in the membrane.

1.3.1 Structure of Nafion

Nafion® membranes are composed of hydrophobic perfluorinated polyethylene backbones and hydrophilic sulfonic acid-terminated perfluorinated vinyl ether pendants polymers [12] (Figure 1.2), which form a well-accepted phase-separation structure [13]. The hydrophobic perfluorinated polyethylene backbones in Nafion® constitute the hydrophobic phase, while the clustered sulfonic acid-terminated side chains form the hydrophilic ionic phase. [12, 13] The geometry of the ionic phase in terms of its size and shape is known to affect the transport of the protons and the water residing in this phase. [14]

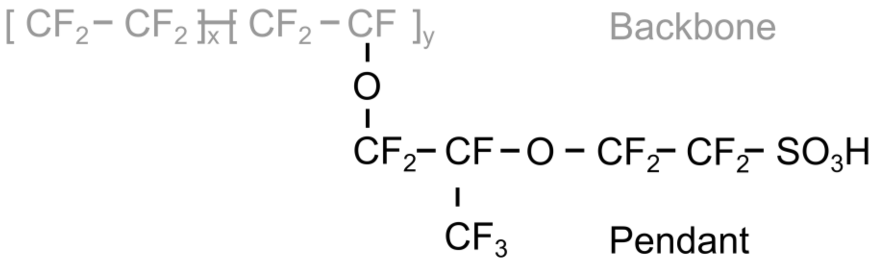

$[CF_2-CF_2]_x[CF_2-CF(-O-CF_2-CF(CF_3)-O-CF_2-CF_2-SO_3H)]_y$

Figure 1.2 Chemical structure of Nafion®

The phase-separation structure of Nafion® has been extensively studied by small angle X-ray (SAXS) and small angle neutron scattering (SANS) techniques. [12, 15-21] The origin of the two small-angle scattering maxima (Figure 1.3a) has been discussed by Gierke *et al* and others. [12, 15, 17] The scattering maximum at the small scattering angle (small scattering vector, Q) is believed to arise from the interference between crystalline structures, and the maximum at the larger scattering angle, from the ionic clusters [15, 21]. Location of the scattering maximum from the ionic clusters is related to the diameter and the inter-cluster distance through a spacing (d) between Bragg the planes given by 2π/Q.

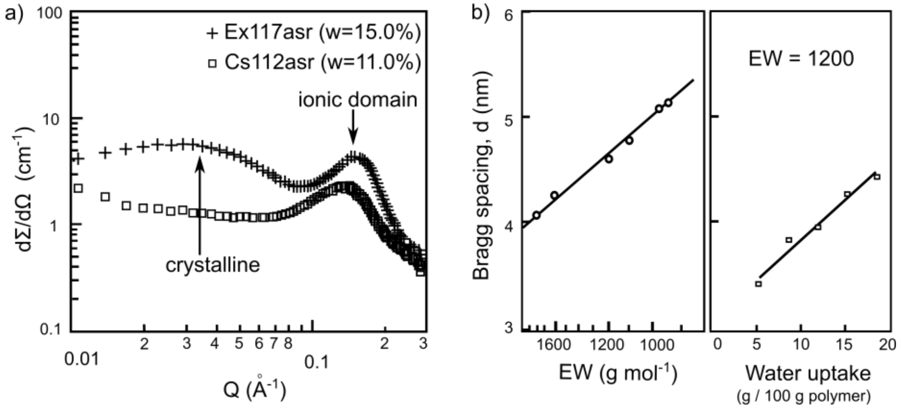

Figure 1.3 a) SANS profiles of Nafion® membranes with indicated water uptake: Ex117asr and Cs112asr are as-received extruded Nafion®117 and solution-cast Nafion®212; the image is adapted from the work of Kim *et al* [21] b) Variation of Bragg spacing (d) of the ionic clusters in various membranes with different equivalent weight (EW) (left) and different water content (right); the images are adapted from the work of Gierke *et al* (1981) [12]

Apparently, the scattering feature of the ionic clusters in Nafion® membranes is affected by the density of sulfonic acid groups in the polymer, a parameter called the equivalent weight ($EW = \frac{Weight_{dry\,membrane}}{mole_{SO_3^-}}$ g mol^{-1}). [22] A smaller value of EW means a larger amount of sulfonic acid groups. The scattering feature of the ionic clusters is also affected (increased) by the water content in the membrane. In order to clearly understand the scattering feature of ionic clusters and clarify the structural change caused by variations in EW and water content, many structural models of Nafion® membranes have been developed four of which are summarized in Figure 1.4. [13, 15, 17, 18, 20, 21, 23, 24]

A cluster-network model with spherical ionic clusters connected by water channels of 1 nm in diameter was proposed by Gierke and co-workers. [12, 23] In the model, the position of the maximum of the ionic scattering peak is assigned as the distance between two neighboring spherical clusters. Water molecules reside in both the ionic clusters and the 1 nm water channels. The model explains the swelling morphology of Nafion® after taking up water. As shown in Figure 1.4a, the spherical ionic clusters in Nafion® membranes swell with increasing water content. The interconnected water channels are added to the model to reconcile the excellent transport properties with regard to water and protons. Another model used to describe the ionic scattering peak in SAXS and SANS is the core-shell model. In the core-shell model, the position of the ionic scattering maximum (the larger scattering angle at the scattering profile) corresponds to the average diameter of the clusters. [15, 16] However, Gebel and Lambard [17] calculated the theoretical scattering pattern based on two models – the core-shell model and a local order model (Figure 1.4b) [25] – and found that the fit to the experimental scattering pattern based on the local order model was more accurate. The local order model contains spherical ionic clusters without any water channels (1 nm) connecting the ionic clusters. [17] Transmission electron micrographs (TEM) of ultrathin sections of the Nafion® membrane stained with metal ions seemed to provide a strong evidence for the ionic clusters to be spheres. [16, 23, 26, 27] However, critics of TEM results of Nafion® membrane raise the question, "is the structure of the ultrathin section of the membrane the same as that of the bulky Nafion® membrane with a microscale thickness?". Staining the membrane with metal ions can change the structure of Nafion®. The spherical ionic clusters have been biased by the results of Falk *et al*. [28] Falk and co-workers measured the IR spectra of a fully hydrated Nafion® membrane and found that roughly 25% of the total amount of OH from water molecules interact with the membrane structure. [28] The average diameter of the spherical ionic clusters deduced from Falk's results was 1.2 nm, which is nearly 4-folder smaller than that from the estimation of Gierke *et al*.

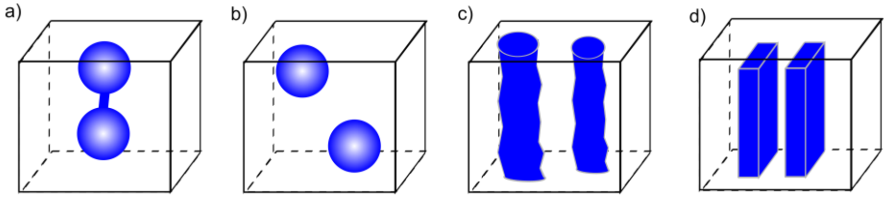

Figure 1.4 Morphological models of Nafion membranes: a) cluster – network model [12, 23]; b) local order model [17]; c) parallel cylindrical water-channel model [13]; d) flat water-"film" model [14].

More recently, Schmidt-Rohr and Chen [13] have proposed a model featuring parallel cylindrical water nanoscale channels, and the simulated scattering profile based on the model matches the ionic scattering profile for the scattering range. In the parallel water-channel model, cylindrical inverted micelles are lined with sulfonic acid groups (Figure 1.4c) and stabilized by the polymer backbones. The average diameter of the water channels is in the range between 1.8 nm to 3.5 nm. [13] Kreuer *et al* criticized the ambiguity of the procedure that Schmidt-Rohr and Chen used for simulating the SAXS pattern of

Nafion®, [13, 14] and pointed out that the value of the water volume fraction used in the calculations of Schmidt-Rohr *et al* was wrong. Schmidt-Rohr and Chen reported that the SAXS data used in their work was measured from a fully hydrated Nafion® membrane which should maintain a water volume fraction of 40 vol%, [14] while they constrained the value in the fit to 20 vol%. [13] Kreuer *et al* fitted the SAXS data to the water-channel model allowing the water volume fraction to be a free parameter in the fit, and they found that the fit of the scattering pattern failed to reproduce the ionic scattering peak within the experimental range. [14] Kreuer *et al* further proposed a new model with local float and narrow water domains (Figure 1.4d), and the fit based on the new model reproduced the SAXS data at the Q-range from 1 nm^{-1} to 3 nm^{-1}. [14] However, Kreuer *et al* did not discuss the deviation of the fitted scattering pattern based on their model form the SAXS data at $Q = \sim 4\ nm^{-1}$ and at $Q < 1\ nm^{-1}$.

In summary, simulated the scattering patterns based on different models are used to reproduce the single, broad ionic scattering peak in SANS data and SAXS data from Nafion® in order to extract the structural features of the membrane that gives rise to the peak. All structural models of Nafion® membranes discussed above have been proposed based on the SANS and SAXS experiments and have assisted in the understanding the structure of Nafion® membranes. Because of the complexity in choosing a model and simulating the scattering pattern, it is challenging to draw specific details from the ionic scattering peak. [29] In addition, different types of water molecules, which exist in Nafion® membrane due to the fact that water molecules are interacting with different constitutions (with either other water molecules or the membrane), constitute the overall water content in the membrane. Although the shift and intensity change of the ionic scattering peak with changing water content have been observed and indicate structural changes relating to the water content in the membrane, [12, 14] reports about the chemical constitution of water in the ionic cluster are scarce.

An obvious and convenient method to study water constitution and structure is vibrational spectroscopy as used by Falk *et al*. [28, 30] Vibrational spectroscopy probes the molecular vibrations of materials, e.g. water molecules themselves or the chemical bonds in Nafion® membranes, can provide information about the local water environment. Vibrational spectroscopy thus provides the ability to chemically identify molecular entities, and structural deduction can be made by detailed analysis of vibrational peak locations and shapes as both are environmentally dependent. [31] Vibrational spectra of water molecules in different molecular environments have different spectral features, and these spectral features provide abundant information about how the state of the water molecules relates to the local physicochemical environment and in turn, the membrane structure that gave rise to these features. [28, 30, 32]

1.3.2 Water transport in Nafion

The presence and transport of water in Nafion® is crucial for achieving effective proton conduction [33] and ensuring good performance of PEMFC. [34] Understanding the role of water in PEM, especially the water transport, is essential to optimize the proton conduction and performance of the FC. Numerous investigations exist on water transport (water diffusivity) in Nafion® membranes. [34-40] The reported value of water diffusivity – the diffusion coefficient (D) – in the same type of Nafion® differs significantly due to combined effects resulting from different manufacturing methods (extrusion versus solution cast), measurement conditions (e.g. different relative humidity of the environment to humidify the membranes), and measurement methods. This confusion makes establishing a fundamental understanding of water diffusivity in Nafion® membranes very challenging. Indeed, different types of Nafion® membranes may manifest different water diffusivity due not only to the above experimental challenges but also the fact that the structure of the membranes may be actually different. [41] Table 1.1 summarizes the diffusion coefficient (D) in various Nafion® membranes obtained from several methods. The values of D vary by two orders of magnitude.

From hydration/dehydration experiments where weight changes of Nafion® membranes have been measured, Takamatsu *et al* reported an D obtained from dehydration process being an order magnitude larger than that from the hydration process [35]. The D reported by Takamatsu *et al* is smaller than what Hallinan *et al* reported using the Fourier transform infrared – attenuated total reflectance spectroscopy (FTIR-ATR) [36, 42]. Hallinan *et al* recorded the time-lapsed IR spectra of Nafion® membrane and quantified the change in water content in the membrane by the absorbance of OH stretching vibration from water molecules in the membrane. The D reported by Hallinan *et al* is more credible because they incorporated both the diffusion and the reaction of dissociating sulfonic acid groups upon hydration in the membrane. The effect of polymer relaxation is induced by the absorbing water. [42] Reaction between water and sulfonic acid group dominate the water activity when initial water molecules are absorbed into dry Nafion® membranes, and polymer relaxation is induced by the absorbance of water. [28] For Nafion® membranes in hydration experiments, both the polymer relaxation and the dissociation of sulfonic acid groups of the membranes are not negligible. The interfacial effect that is related to the surface structure in the membranes is absent in the works of both Takamatsu *et al* [35]and Hallinan *et al*. [42]

Table 1.1Water diffusivity in Nafion® membranes

Researchers	Experimental details and results	Diffusion coefficient (m^2/s)
Takamatzu *et al* [35]	Water absorption of Nafion® membrane (acid form, $EW = 1155$ g mol^{-1})	1.8×10^{-10} (liquid water); 2×10^{-12} (water vapour)

	from liquid water at 20 ^{o}C and from water vapor with a relative humidity of 100% at 23 ^{o}C	
Tsushima *et al* [43]	NMR; Nafion® at various hydration state	2.0×10^{-10}
Klein *et al* [44]	NMR; Extruded Nafion® 1110 at acid form with $EW = 1100$ g mol^{-1}	$0.7\ to\ 1.6 \times 10^{-10}$
Suresh *et al* [39, 45]	Radiotracer; HTO diffusing out of Extruded Nafion® 117 in the acid form $EW = 1100$ g mol^{-1}) and in the Na^{+} from	3.87×10^{-10} (acid form) 2.85×10^{-10} (Na^{+} form)
Hallinan *et al* [36, 42]	FT-IR; mutual diffusion of methane and water in Extruded Nafion® 117; hydration and dehydration of Nafion® 117	4.15×10^{-10} (mutual); $4.44\ to\ 7.50 \times 10^{-11}$ (hydration/dehydration)
Davis *et al* [40]	FT-IR;H2O / D2O exchange in Nafion thin film (the thickness was less than 200 nm; $EW = 1100$ g mol^{-1})	$2.5\ to\ 4 \times 10^{-16}$

There are other studies that have attempted to eliminate effects related to the dynamic structure of Nafion® during the hydration experiments and thus interpreted water transport with Fickian diffusion model within the membrane. [39, 40, 43, 45, 46] Those works have primarily used methods of nuclear magnetic resonance (NMR), [34, 43] water permeability measurement and vibrational spectroscopy, [36, 40] and maintained the membrane in a steady state of hydration where the structural changes were negligible. Values of the D in Nafion® membrane from different NMR studies vary by a factor of two, [43, 46] 2 ~ 4 × 10 $^{-10}$ m^2/s, and are comparable to the D reported by Motupally *et al* which was determined using a permeability method. [47] Davis *et al* probed the isotopic exchange of H_2O and D_2O in Nafion® thin films (the thickness < 200 nm) using infrared absorption spectroscopy. [40] The D of H_2O and D_2O Nafion thin films was reported to be 4 to 6 orders of magnitude lower than that in the bulk Nafion® membrane (the thickness > 20 µm). Davis *et al* ascribed the significantly slow water diffusion in their work to the membrane structure. Davis *et al* claimed that the Nafion chain dynamics in the thin membrane was significantly slower than the bulk Nafion® membrane, and the slower chain dynamics led to slower water diffusion.

To summarize, NMR and water permeability techniques enabled sufficient characterization of D in terms of water transport in the membrane at a defined steady state. However, these techniques do not provide structural information about the membrane. FTIR-ATR measures the molecular vibrations of both the diffusants and the membrane, providing the possibility to obtain the chemical structural information. However, extracting structural information about the bulk Nafion® membranes is impossible due to the fact that FTIR-ATR captures the signal from both the surface structures and bulk structures of the membranes. An alternative vibrational spectroscopy technique is the Raman scattering microspectroscopy which provides vibrational fingerprints with the spatial resolution of an optical microscope and can easily probe bulk materials. [48] Although many research groups have studied the water distribution inside the Nafion® membranes in a static state by using Raman scattering microspectroscopy, [4, 49-53], it is challenging for these groups to probe the water transport in these membranes due to the fact that the temporal resolution of the Raman scattering microspectroscopy is limited. A long integration time is needed to obtain a spectrum with a reasonable signal-to-noise ratio because the Raman scattering is typically rather weak. The spectrum may also contain a strong fluorescence contribution which has to be removed from the spectrum in order to extract quantitative information from the spectrum. A time-lapsed Raman scattering spectroscopy apparatus with millisecond time resolution would be an ideal technique to probe water transport in Nafion® membranes because: 1) it can be configured to probe only the bulk membrane, and 2) it provides information about the water and membrane chemistry. Developing and applying a sufficiently fast Raman-based technique to study water structure and transport in Nafion® is the core subject of my thesis. I used coherent anti-Stokes Raman scattering (CARS), which has been developed to overcome both limitations mentioned above for traditional Raman microspectroscopy, to interrogate water-membrane chemistry in Nafion®. A theoretical overview of Raman and CARS scattering is provided in Chapter 2.

1.3.3 Water structure in Nafion

An increasing amount of water in PEM including Nafion® membranes is found to correlate with high proton conductivities, [48, 54] and numerous works have focused on maximizing the amount of water in PEM. [55-59] This leads us to a seemingly simple question: How does water affect proton conduction in the PEM? Qualitative studies of the vibrational FT-IR spectra suggested that the "state of water" in Nafion® changes with increasing water content and the changing state of water in the membrane is significantly related to its proton conducting ability. [60, 61] According to these studies, for Nafion® with low water content, the water molecules are only used for dissociating the sulfonic acid groups in the ionic clusters, while with increasing water content, some water molecules may also interact with the sulfonic acid groups and others may (very rarely) hydrate hydrophobic backbones. [28] The studies on FTIR spectra of Nafion® membranes have provided evidence that different water subspecies exist in the membranes. However, quantification of the water subspecies and their contribution to the total “state of water” are scarce. The ambiguity of the relationship between the state of water and the membrane properties in terms of proton conductivity and water transport necessitates further studies of water in Nafion® membranes.

Fayer and co-workers have investigated water in Nafion membrane using non-linear IR spectroscopy in an attempt to elucidate the water structure in these membranes. [62, 63] They used nanometer-sized anionic aerosol-OT (AOT) reverse micelles (Figure 1.5a) to mimic the ionic domains in Nafion® membranes and established the existence of two water subspecies with very different vibrational signatures and dynamics residing in the micelles [64, 65]. Their findings have led to the proposal of a core-shell model where bulk-like water (bulkW) existed at the core of the micelles and non-bulk (shell, nonbulkW) water exists at the micelle interface. [64, 65] Based on the vibrational signatures of the two water subspecies from the AOT reverse micelles, the nonbulkW was concluded to be less coordinated than bulkW. The core-shell model for explaining the water structure in the AOT reverse micelles can also be used to understand the water structure in the ionic domains (Figure 1.5b) in Nafion® membranes. [63, 66] Consistent with Fayer’s core-shell model for water structure in Nafion membranes, Benziger and colleagues [34, 67] have proposed a similar core-shell model for water structure in Nafion® membranes.

Indeed, the preceding studies have provided strong evidence for the existence of different water subspecies in Nafion® membranes. Nevertheless, the quantification of the fractional contribution and the spectral shape (chemistry) of different water subspecies in the bulk Nafion® membranes is absent.

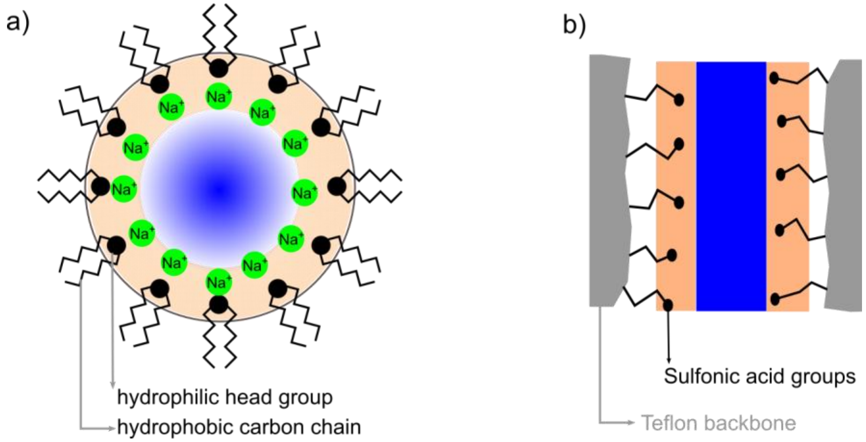

Figure 1.5 Schematic depiction of a core-shell model for water structure in: a) AOT reverse micelle; b) ionic clusters in Nafion® membranes. Blue denotes the core water; orange denotes the shell water. The black circles are the sulfonic acid groups.

CHAPTER 2

THEORETICAL BACKGROUND

2.1 Raman scattering

When light irradiates a material, its energy may be transmitted, absorbed or scattered. As shown in Figure 2.1 [31], absorption of an incident photon whose frequency is the same as the molecular vibrational frequency results in a transition between two energy levels – the ground state and excited state (Figure 2.1a). Scattering, on the other hand, is stimulated by an incident photon with a frequency that is not matched with a molecular vibrational frequency and leads to Rayleigh (elastic) scattering and Raman (inelastic) scattering.

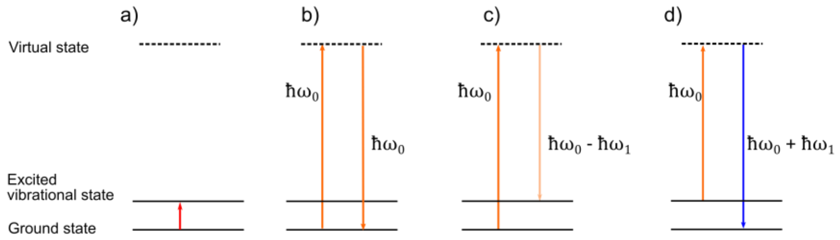

Figure 2.1 Energy diagram of: a) absorption; b) Rayleigh scattering; c) Stokes Raman scattering with scattered photon energy of $\hbar\omega_0 - \hbar\omega_1$; d) anti-Stokes Raman scattering with scattered photon energy of $\hbar\omega_0 + \hbar\omega_1$. $\hbar\omega_0$ is the energy of an incident photon. $\hbar\omega_1$ is the energy difference between the ground level and the first level.

In Rayleigh scattering, a molecule is excited to a virtual state and "instantaneously" returns to the ground state. The scattered photon has the same energy as the incident photon (Figure 2.1b); while in Raman scattering, the scattered photon has less (Figure 2.1c, Stokes Raman scattering) or more (Figure 2.1d, anti-Stokes Raman scattering) energy compared to the incident photon. The scattered photon energy in Raman scattering contains unique vibrational information of the molecule.

From a classical physics perspective, molecular vibrations are Raman active when there is a change in the molecular polarizability with nuclear coordinate for the bound nculei. The molecular polarizability is the deformability of the electrical environment of a molecule by an external electric field and is generally a function of the nuclear coordinates (and frequency, which is ignored for simplicity here). Variation of the polarizability (α) for a small displacement with vibrations of the molecules with the nuclear coordinate can be expanded to the first order in Taylor series as:

$$\alpha(Q) = \alpha_0 + (\frac{\partial \alpha}{\partial Q})_0 Q \qquad \text{Eq 2.1}$$

where α_0 is equilibrium polarizability when the atoms of a molecule are at the equilibrium position with respect to vibrational motion, Q is a normal vibrational coordinate and $(\frac{\partial \alpha}{\partial Q})_0$ is vibrational modulation of molecular polarizability with respect to Q around the equilibrium position. If we assume Q varies sinusoidally with a nuclear vibration (ω_{vib}), we can write Q as:

$$Q = Q_0 cos(\omega_{vib} t + \varphi) \qquad \text{Eq 2.2}$$

where φ is a phase factor and Q_0 is the amplitude.

$$\mu = \alpha(Q)E(t) \qquad \text{Eq 2.3}$$

The induced dipole moment (μ) represents the light-molecule interaction when looking at the charge in the local electrical environment caused by the incident radiation on the molecule. μ is the product of the polarizability (α) and external electric field $E(t)$ of the incident photons (Eq 2.3) to the first order and can be rewritten as:

$$\mu = \alpha_0 E(t) + \left(\frac{\partial\alpha}{\partial Q}\right)_0 Q_0\, cos(\omega_{vib}t + \varphi)E(t) \quad \text{Eq 2.4}$$

Substitution of $E(t) = E_0\ cos(\omega t)$ to Eq 2.4 yields

$$\mu = \alpha_0 E_0 cos(\omega t) + \left(\frac{\partial\alpha}{\partial Q}\right)_0 Q_0 cos(\omega_{vib}t)E_0 cos(\omega t) \quad \text{Eq 2.5}$$

where I have dropped the phase factor (φ) for convenience. Using a trigonometric identity, Eq 2.5 can be reformatted to as

$$\mu = \alpha_0 E_0\, cos(\omega_0 t) + \frac{1}{2}\left(\frac{\partial\alpha}{\partial Q}\right)_0 Q_0 E_0[cos(\omega_0 - \omega_{vib})t + cos(\omega_0 + \omega_{vib})t] \quad \text{Eq 2.6}$$

Rayleigh scattering arises from the dipole oscillating at ω_0 induced by field with the finite equilibrium polarizability of the molecular while the Raman scattering arises from the dipole oscillating at $\omega_0 \pm \omega_{vib}$. Note, the necessary condition for Raman scattering is that the term $(\frac{\partial\alpha}{\partial Q})_0 \neq 0$.

The intensity is linearly dependent on the number of scattering molecules (N) and can be used to quantify the abundance of the corresponding molecules. Increasing the laser flux power density (I_0) or using an incident laser with a shorter wavelength (due to the overall reduced Rayleigh scattering) can also increase the Raman intensity. The intensity of the spontaneous Raman intensity for a given molecular vibration is given as [68]:

$$I_{Raman} \propto \omega_0^4 N I_0 (\frac{\partial\alpha}{\partial Q})^2 \quad \text{Eq 2.7}$$

where N is the number of the scattering molecules.

Practically, a molecular vibration excited by an incident laser at a frequency of ω_0 produces a Raman scattering intensity as given by Eq 2.8. [69]

$$I_{Raman} \propto \frac{NA\Gamma}{(\Omega - \omega_0)^2 - \Gamma^2} \qquad \text{Eq 2.8}$$

where N is the number of scattering molecule, A, Ω, and Γ are the amplitude, frequency and line width of the vibration mode of the molecule.

2.2 Coherent anti-Stokes Raman scattering (CARS) spectroscopy

As the Raman cross-section for spontaneous Raman is very low and only ~ 1 out of 10^7 incident photons are inelastically scattered [69], long acquisition times are typically required to obtain a spectrum with a high signal-to-noise ratio. Moreover, the Stokes Raman signal is often overwhelmed by single-photon fluorescence (also Stokes shifted relative to incident light) that can be orders of magnitude more prominent. [69] One solution to the low Stokes Raman signal is to use nonlinear excitation such as coherent anti-Stokes Raman scattering (CARS) spectroscopy, which provides a signal enhancement of up to 6 orders of magnitude compared to conventional Raman, and has many other advantages over the spontaneous Raman spectroscopy as outlined below. The nonlinear excitation allows one to acquire a spectrum much more quickly than conventional Raman for a given signal-to-noise ratio, on the order of milliseconds rather than seconds per spectrum – when processed appropriately (as described in section 2.3). The CARS technique is intrinsically optically sectioned (due to the nonlinear nature), and CARS emission is directional. Moreover, the contamination of fluorescence is minimized in CARS, since the detected signal is blue-shifted.

Generating a CARS signal involves interaction of three photons – 1) pump beam at a frequency of ω_{pu}, 2) the Stokes beam at a frequency of ω_s, and 3) probe beam ω_{pr} – with the sample (Figure

2.2). The frequency of the generated CARS signal (ω_{as}) is dependent on the pump, Stokes and probe beams as described below:

$$\omega_{as} = \omega_{pu} - \omega_s + \omega_{pr} \qquad \text{Eq 2.9}$$

The CARS setup in this work used a degenerate configuration with the pump and probe at the same frequency, thus the relationship of ω_{as} with the frequencies of incident photons is simplified to the equation below:

$$\omega_{as} = 2\omega_{pu} - \omega_s \qquad \text{Eq 2.10}$$

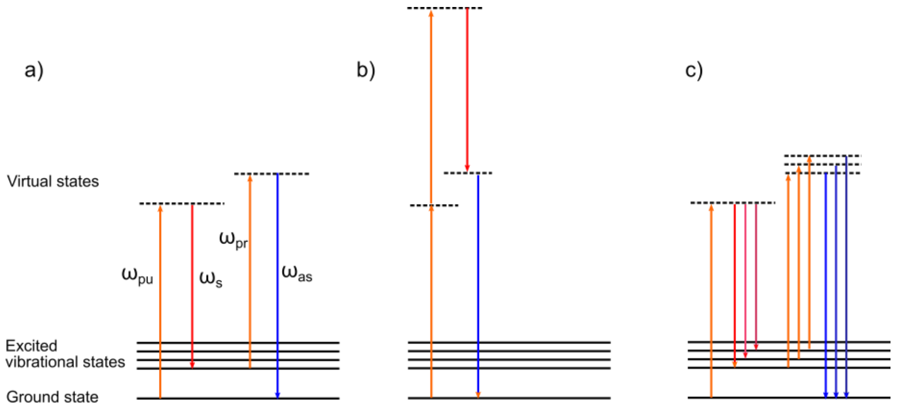

Figure 2.2 CARS energy diagram: a) vibrational resonant scheme for single-line CARS; b) nonresonant electronic contribution; c) vibrational resonant scheme for multiplex CARS (also called broadband CARS), where multiple transitions are addressed simultaneously.

The anti-Stokes process is resonantly enhanced when the frequency difference, $\omega_{pu} - \omega_s$, matches the frequency of a vibrational resonance (ω_{vib}) of a molecule, thereby giving a strong signal corresponding to the vibrational modes in the sample. However, the CARS signal does not directly provide quantitative composition information. [70] Additional data processing for the CARS signal must be conducted for extracting the quantitative chemical information. The CARS signal (I_{CARS}) is proportional to the squared modulus of the third-order induced polarizability ($P^{(3)}$) as shown below:

$$I_{CARS} \propto |P^{(3)}|^2 \qquad \text{Eq 2.11}$$

and $P^{(3)}$ is proportional to the squared modulus of the complex third-order susceptibility $\chi^{(3)}$ as:

$$|P^{(3)}|^2 = |E_{pr}|^2|E_{pu}|^2|E_s|^2|\chi^{(3)}|^2 \qquad \text{Eq 2.12}$$

where E_{pu} and E_{pr} are the pump and probe electric fields, E_s is the Stokes electric field.

The complex third-order susceptibility ($\chi^{(3)}$) contains two terms (Eq 2.13): 1) the resonant part containing the quantitative and chemically specific information about the sample including a real component and an imaginary component, and 2) the nonresonant ($\chi_{NR}^{(3)}$) part depending solely on the electronic properties of the sample. The $\chi_{NR}^{(3)}$ can be assumed to be strictly real and is generally considered to be frequency-independent.

$$\chi^{(3)} = \chi_{NR}^{(3)} + \chi_{R}^{(3)} \qquad \text{Eq 2.13}$$

Because of the squared dependence on $\chi^{(3)}$, the resonant and nonresonant responses interfere as described below:

$$|\chi^{(3)}|^2 = \left|\chi_{NR}^{(3)}\right|^2 + \left|\chi_{R}^{(3)}\right|^2 + 2\chi_{NR}^{(3)}Re\left[\chi_{R}^{(3)}\right] \qquad \text{Eq 2.14}$$

Thus, the nonresonant term cannot be removed by a simple background correction method. The presence of nonresonant contribution to the overall susceptibility means that there is no simple linear correlation between the CARS intensity (I_{CARS}) and concentration; it strongly depends on the ratio $\chi_{R}^{(3)}/\chi_{NR}^{(3)}$.

For a given vibrational resonance, $\chi_{R}^{(3)}$ describes the vibrational response of the sample and is given by the equation below: [69]

$$\chi_R^{(3)} = \frac{NA}{\Omega - \left(\omega_{pu} - \omega_s\right) - i\Gamma} \qquad \text{Eq 2.15}$$

where, N is the number of scattered photons per unit volume; A, Ω, and Γ are the amplitude, frequency and line width of the vibration mode.

The imaginary part of $\chi_R^{(3)}$, given by Eq 2.16 can be compared directly to I_{Raman} (Eq 2.8). [71] In other words, $Im\left[\chi_R^{(3)}\right]$ is chemically specific and depends linearly on concentration.

$$Im\left[\chi_R^{(3)}\right] = \frac{NA\Gamma}{\left[\Omega - (\omega_{pu} - \omega_s)\right]^2 - \Gamma^2} \qquad \text{Eq 2.16}$$

Hence, for obtaining corresponding quantitative information, it is crucial to extract $Im\left[\chi_R^{(3)}\right]$ from the CARS signal is crucial for obtaining corresponding quantitative information. In the following section, we describe one approach to extract $Im\left[\chi_R^{(3)}\right]$ from the CARS signal, which is the time-domain Kramers-Kronig transform (TD-KK) for spectral phase retrieval. [72] The $Im\left[\chi_R^{(3)}\right]$ of all CARS spectra in this work were extracted using TD-KK.

2.3 Time-domain Kramers-Kronig transform

The phase ($\varphi(\omega)$) of a complex function ($\chi(\omega)$) can be expressed by a Kramers-Kronig (KK) transform as:

$$\varphi(\omega) = -\frac{P}{\pi}\int_{-\infty}^{+\infty} \frac{ln|\chi(\omega'')|}{\omega'' - \omega}\, d\,\omega'' \qquad \text{Eq 2.17}$$

where P is the Cauchy principal value, and $\chi(\omega) = |\chi(\omega)|e^{i\varphi(\omega)}$ when $\chi(\omega)$ is causal.

To ensure causality, an operator $\psi(f(\omega))$ can be defined as:

$$\psi(f(\omega)) = F[u(t)F^{-1}[f(\omega)]] \quad \text{Eq 2.18}$$

where F and F^{-1} denote the Fourier and inverse Fourier transforms, respectively, and $u(t)$ is the Heaviside Function, and Fourier transform of $u(t)$ can be expressed as:

$$F[u(t)] = \frac{1}{i}\sqrt{2\pi}\omega + \frac{\sqrt{\pi}}{2}\delta(\omega) \quad \text{Eq 2.19}$$

Using convolution theorem and substituting Eq 2.19 to Eq 2.18, one obtains:

$$\psi(f(\omega)) = \frac{1}{2}\left[-\frac{i}{\pi}P\int_{-\infty}^{+\infty}\frac{f(\omega')}{\omega'-\omega}d\omega + f(\omega)\right] \quad \text{Eq 2.20}$$

Combining Eq 2.17 and Eq 2.20, the phase is expressed as

$$\varphi(\omega) = 2Im\left[\psi(ln|\chi(\omega)|) - \frac{ln|\chi(\omega)|}{2}\right] \quad \text{Eq 2.21}$$

where the CARS signal is proportional to $|\chi(\omega)|^2$. $u(t)F^{-1}[f(\omega)]$ is replaced with Eq 2.22 and the Fourier transform of the nonresonant background signal is used at negative time.

$$\eta(t{:}\, f(\omega)) = \begin{cases} F^{-1}[f(\omega)], & t \geq 0 \\ F^{-1}[f_{NR}(\omega)], & t < 0 \end{cases} \quad \text{Eq 2.22}$$

Thus, the spectral phase is given as:

$$\varphi(\omega) = 2Im[F(\eta(t{:}\, In|\chi(\omega)|) - \frac{In|\chi(\omega)|}{2}] \quad \text{Eq 2.23}$$

An example of this process is shown below (Figure 2.3). Here, we used the CARS signal of a dry Nafion® 212 membrane as a representative spectrum, and the nonresonant background (NRB) was taken from a membrane on top of a glass coverslip (Figure 2.3a).

Inverse Fourier transformation of both the square root of the CARS spectrum and that of the NRB, $F^{-1}[f(\omega)]$ and $F^{-1}[f_{NR}(\omega)]$ is the initial step (Figure 2.3b). Then $\eta(t\colon f(\omega))$ was obtained by replacing $F^{-1}[f(\omega)]$ at negative time with the negative-time $F^{-1}[f_{NR}(\omega)]$. Then, the time-domain signal $(\eta(t\colon f(\omega)))$ was Fourier-transformed back into the frequency domain and substituted the results to Eq 2.23; such the phase was reconstructed (Figure 2.3c). Slight errors or noise in the measured NRB result in a non-constant error phase, which has to be removed. [73] The Raman-like spectrum $Im\left[\chi_R^{(3)}\right]$ is produced after subtracting the error phase from the reconstructed phase as $Im\left[\chi_R^{(3)}\right] = sin(|\chi(\omega)|e^{i\varphi'(\omega)})$, where φ' is the retrieved phase after error phase subtraction.

The Raman-like spectrum was compared with a spectrum taken from the dry Nafion® 212 membrane via a spontaneous Raman spectroscopy (the excitation laser is 633 nm with a laser power of 21 mW). The spontaneous Raman spectrum after background subtraction (with an iterative moving window of 293 cm^{-1} wide) is shown in Figure 2.3d.

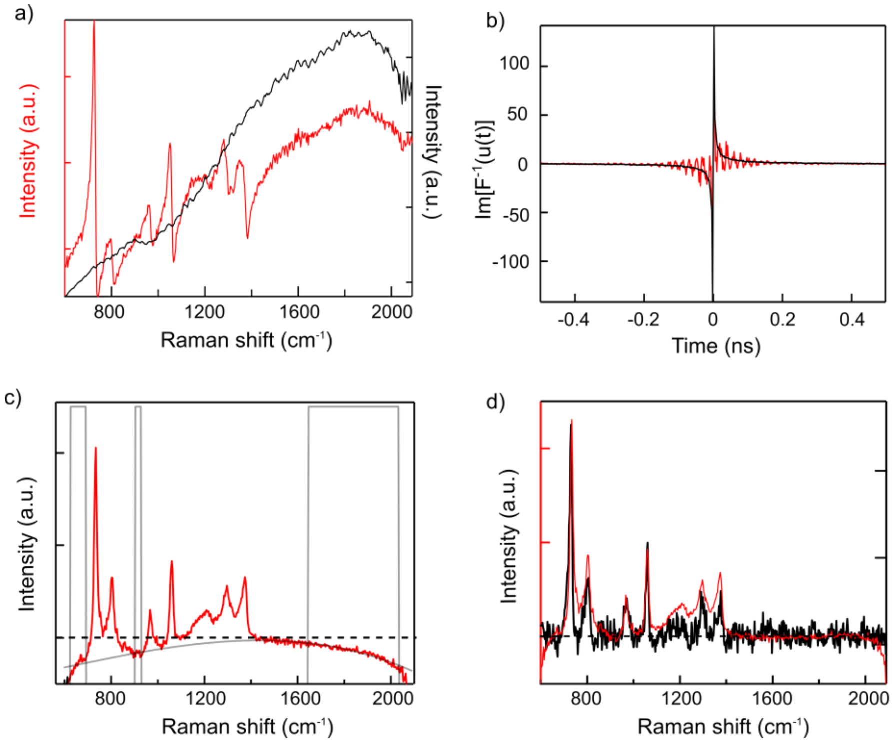

Figure 2.3 a) the CARS spectrum from the dry Nafion® 212 membrane (red) and the nonresonant background (NRB) from glass coverslip (black); b) the imaginary part of $F^{-1}[f(\omega)]$ and $F^{-1}[f_{NR}(\omega)]$; c) the phase given by Eq 2.23, and a third-order polynomial accompanied by a fit mask (gray) was used to fit a slowly varying error phase, as shown in red; d) red, the Raman-like (RL) spectrum (red) produced after subtracting the error phase, and black, the spectrum of Nafion membrane measured by spontaneous Raman spectroscopy (excitation laser: 633 nm, 21 mW, integration time 10s).

2.4 Constrained non-negative least squares algorithm

2.4.1 Multivariate curve resolution–alternating least squares (MCR-ALS)

In linear systems, a spectral data matrix can be reconstructed with a linear combination of spectral shapes of “pure” components weighted by their scaling factors as: [74]

$$M = \sum_{i=1}^{n} c_i \, s_i + E \qquad \text{Eq 2.24}$$

where M is a measured spectrum of the mixture of s_i components in that are weighted by c_i the scaling factors (or concentrations) where j is the index for n total components; E is the experimental error. If one knows the spectral shape of all pure components, the corresponding set of c_i can be readily extracted by the fit the of the spectral data matrix to Eq 2.24.

However, the above concepts cannot be applied in a straightforward format to all systems because the number and the spectral shape of the pure components in many systems are unknown. For the systems with limited or even no *prior* knowledge for the pure components in terms of the number and the spectral shapes, one has to develop a method able to decide the number and spectral shape of the possible pure components. Multivariate Curve Resolution-Alternating Least Squares (MCR-ALS) reported by Anna de Juan and co-workers is a sophisticated way to work with such unknown systems. [75] In MCR-ALS, the spectral data matrix M is reconstructed by a linear combination of unknown components weighted by a scaling factor (the linear combination is an analogue to Eq 2.24; c_i and s_i are referred to as matrix instead of one spectrum). As applied in this thesis, the number of components for MCR-ALS was chosen by assessing the singular values from a singular value decomposition (SVD) for M. In the SVD, M is decomposed to three matrices as: [76]

$$M = \ U\Sigma V \qquad \text{Eq 2.25}$$

where M is a matrix of dimension m×p; U is an m×m unitary matrix (left singular vectors), Σ is an m×m diagonal matrix relating to the average contributions of the singular vectors (singular values) and V is a p×p unitary matrix (referred to the spatial distribution of the singular vectors of M). A larger singular value means a larger contribution to M from the corresponding singular vector, which can be referred to as chemical contributions, while a small value generally implies that it involves a contribution from noise. In the graphical user interface (GUI) of MCR-ALS provided by Anna *et al*, the singular values of all singular vectors are shown in a decreasing sequence. Then, one can define the threshold singular value above which the singular values are retained. The number of components that have larger singular values is therefore chosen as the total number of components. Prior knowledge of the system can certainly help decide the number of pure components. After deciding the number of components, initial guesses for either c_i or s_i are obtained using various methods to start the iteration algorithm. The initial guesses are optimized until a convergence criterion is fulfilled. The MCR-ALS GUI provides two ways to set the criterion: 1) a pre-set number of iterations; 2) to set the threshold value of the difference between consecutive interactions.

MCR-ALS provides a reasonable way to decide the number of pure components for the unknown systems and to obtain the spectral shape as well as the fractional concentration for each pure component. However, MCR-ALS is not the best way for analysing multi-component system where the spectral shape of one or more pure components is known. For the system with known components, the spectral shape of the known components has to remain constant, meanwhile that of unknown components has to be deduced. With the MCR-ALS GUI implementation, it is impossible to fix the spectral shape of the known components because the concentration and the spectral shape for all components are optimized quasi-simultaneously. A different method is required to deal with systems consisting of known components and unknown components. We propose a related method called constrained classical least squares (CCLS) to deal with the systems with known components.

2.4.2 Constrained classical least squares (CCLS)

The idea behind CCLS is that data matrix M is represented by a linear combination of known components (a) and unknown components (b) weighted by their scaling factors as described below:

$$M = \sum_{a=1}^{A} c_a s_a + \sum_{b=1}^{B} c_b s_b + E \qquad \text{Eq 2.26}$$

where a and b are the indices of the known and unknown components, respectively; A and B are the total numbers of the known and unknown components, respectively; E is the deviation between the experimental data and model data and will be minimized to optimize the fit data to Eq 2.26. In CCLS, we want to obtain the spectral shape of B (s_b) as well as the scaling factors (c_a and c_b). It should be noted that with more known than unknown components the spectral shape of unknown component can be determined more precisely. Ideally, we need the number of data spectra in M to be the same as, or larger than, the undetermined variables in Eq 2.26, such that we will obtain an unique solution to Eq 2.26 with the smallest error (E). Practically, CCLS works well to obtain one unknown component from a system with one or more known components and with a M comprising less than 20 data spectra. However, using CCLS to deduce the more than one unknown component from a larger M requires substantial amount of computational time.

To initiate CCLS, one needs to determine the total number ($n = A + B$) of the pure components in the system. We can use the SVD to yield an estimated value for n. The value of B is given as ($n - A$). Then, we have to provide, as an input, an initial guess for the independent variables, c_a , c_b and s_b . There are ($n + B \times wv$) independent variables in total, given the frequency range of the spectrum wv. Given β_0 as the initial guess of the vector composed with the independent variables, CCLS uses a global fit to find a solution to β by minimizing the ϕ^2 as defined below:

$$\phi^2 = \| M - M' \|^2 \qquad \text{Eq 2.27}$$

where M' is the estimated data (from the fit) [77].

An iterative procedure, e.g. Levenberg-Marquardt algorithm (LM) [77, 78], is used to find the solution. In the LM algorithm, ϕ is represented by a function $F(x)$ as shown below:

$$\phi^2 = \| F(x) \|^2 \qquad \text{Eq 2.28}$$

where x is an independent variable.

For a small δ, a Taylor expansion yields the approximation as:

$$F(x + \delta) \approx F(x) + J\delta \qquad \text{Eq 2.29}$$

where $J = \frac{\partial F(x)}{\partial x}$. [79]

Substitution of Eq 2.29 to Eq 2.28 yields:

$$\begin{aligned}\phi^2 \approx \|F(x) + J\delta\|^2 &= [F(x) + J\delta]^T\,[F(x) + J\delta] \\ &= [F(x)]^T[F(x)] + [F(x)]^T J\,\delta + \delta^T J^T F(x) \\ &\quad + \delta^T J^T J\,\delta\end{aligned} \qquad \text{Eq 2.30}$$

where T denotes transposition of the respective matrix

$$\frac{\partial(\phi^2)}{\partial\delta} \approx \frac{\partial([F(x)]^T[F(x)] + [F(x)]^T J\,\delta + \delta^T J^T F(x) + \delta^T J^T J\,\delta)}{\partial\delta} \qquad \text{Eq 2.31}$$

Taking the partial derivative with respect to δ gives:

$$\frac{\partial([F(x)]^T[F(x)] + [F(x)]^T J\,\delta + \delta^T J^T F(x) + \delta^T J^T J\,\delta)}{\partial\delta} = 0 \qquad \text{Eq 2.32}$$

Simplifying Eq 2.32 gives:

$$J^T J\,\delta = J^T F(x) \qquad \text{Eq 2.33}$$

It should be noted that a damping term $\lambda\, Diag(J^T J)$, [77] is appended to Eq 2.33 yielding Eq 2.34 as described below:

$$(J^T J + \lambda Diag(J^T J))\delta = J^T F(x) \qquad \text{Eq 2.34}$$

where $Diag(J^T J)$ is the diagonal element of $J^T J$.

The LM algorithm iteratively repeats 5 steps as described below:

1) at i-iteration, giving $x = \beta_i$, $F_i(\beta_i)$ and J is updated;

2) $Diag(J^T J)$ and the damping parameter at i-iteration λ_i is updated;

3) δ_i is proposed and $F_{i+1}(\beta_i + \delta_i)$ is evaluated;

4) if $F_{i+1} < F_i$, accept, otherwise reject;

5) stop when the algorithm meets the desired convergence criteria or exceeds a specified number of iterations.

λ is adjusted at each iteration in LM to assure a reduction in $F(x)$ and to determine the iterative step size (δ) as δ is a monotonically decreasing function of λ.

$$\delta = (J^T J + \lambda\, Diag(J^T J))^{-1}\, J^T F(x) \qquad \text{Eq 2.35}$$

If step 4 is rejected, λ is raised otherwise is reduced (Eq 2.35).

It is crucial to initiate LM with a sensible starting point, which requires one to choose an appropriate initial guess for both β and δ. An inappropriate initial guess β_0 may lead the value of ϕ^2 to a local minimum (Figure 2.4). As shown in Figure 2.4, if $\phi^2(\beta)$ is closer to the local minimum than to the global minimum, its minimization would direct the value to the local minimum.

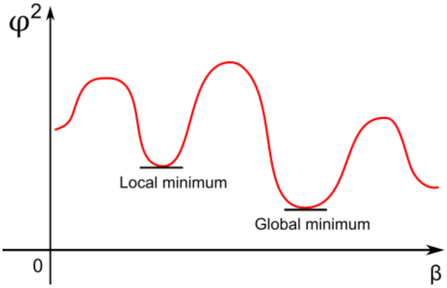

Figure 2.4 Schematic of local minimum and global minimum of ϕ^2.

APPENDIX I contains the source code for processing the CCLS global fit in Igor Pro 6.32 A.

CHAPTER 3
MATERIALS AND METHODS

3.1 Materials

Nafion® 117 (DuPont, 183 µm thick, 360 g m^{-2}) [80] and Nafion® 212 (DuPont, 50.8 µm thick, 100 g m^{-2}) [81] membranes (named as N117 and N212, respectively), both of 1100 g equivalent weight, were cut into pieces (1 cm × 5 cm in size) and boiled for 0.5 h in each of the following solutions separately and subsequently: H_2O_2 (34.5-36.5%, SIGMA-ALDRICH Chemie GmbH), MilliQ H_2O, 0.5 M H_2SO_4 (95.0-98.0%, SIGMA-ALDRICH Chemie GmbH), and MilliQ H_2O again. Then all samples were washed with MilliQ H_2O until the pH of the wastewater was about 7 (pH paper, dispenser 1.0-11.0). Samples were stored in MilliQ H_2O before measurements for a maximum of 5 days. D_2O (99.8 ATOM%D, SIGMA-ALDRICH Chemie GmbH) was used as received in diffusion experiment.

3.2 Broadband CARS

In my thesis, a dual-output laser source (Leukos-CARS, Leukos) provides the pump and Stokes beams. The laser source is a passively Q-switched 1064 nm microchip laser generating sub-nanosecond in pulses at a 32 kHz repetition rate. The beam is split into two parts: 1) one part is introduced into a photonic crystal fiber creating a supercontinuum of a bandwidth of 1050 – 1600 nm; 2) the other part is used as the pump/probe beams at 1064 nm. The Stokes and pump/probe beams were overlapped at a dichroic mirror (LP02-

1064RU-25, Semrock), and introduced into a modified inverted microscope (Eclipse Ti-U, Nikon). The beams were focused onto the sample by an air objective (LCPlan N, 100X / 0.85 IR, Olympus). The forward CARS signal was collected with a 10 X magnification, 0.25 NA air objective (Newport).

3.3 Flow cell for water diffusion experiments

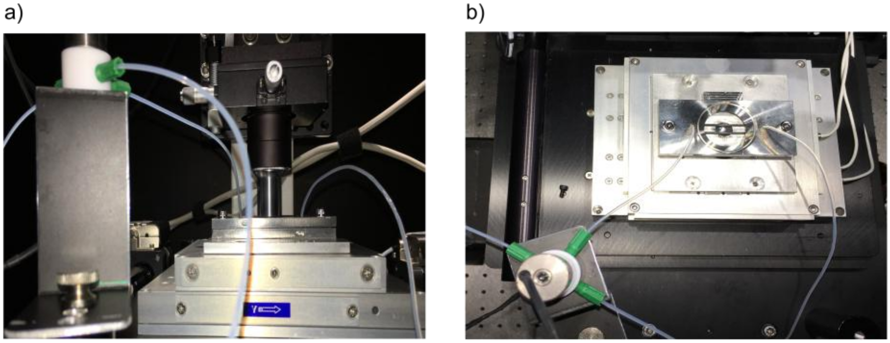

Figure 3.1 Flow cell: a) side view; b) top view.

A microfluidic flow cell was used for the water diffusion experiments. As shown in Figure 3.1 a (top left), a Y-valve (080T212-32, Bio – Chem Fluidics) connected with three Teflon tubes (0.8 mm inner diameter, Bio–Chem Fluidics). Two Teflon tubes were connected to reservoirs filled with H_2O and D_2O, respectively; and only one type of water was chosen by the Y-valve flowing into the output tube that fed the microfluidic channel (1 mm × 0.30 mm × 42 mm, width × height × length). The channel was carved into Perspex slide. The membrane was placed underneath the channel. By switching the water flow from D_2O to H_2O, or vice versa, the H / D exchange experiment was initiated. The geometry of the microfluidic flow cell with a Nafion membrane was shown in Figure 3.2.

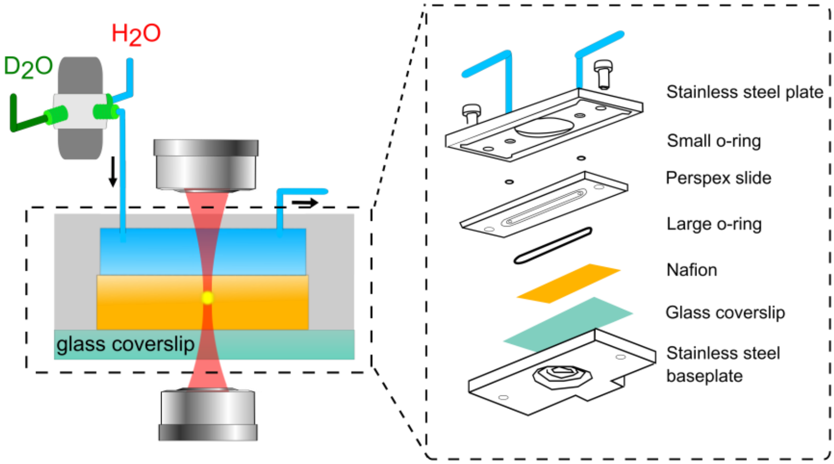

Figure 3.2 The zoomed in view of the flow cell used in the water diffusion experiments.

The flow rate in the channel was calculated based on [82]:

$$Q = \frac{\pi d^4 \Delta P}{128 \mu L} \qquad \text{Eq 3.1}$$

where d is the diameter of the Teflon tubes connecting the reservoirs ($d = 0.8$ mm) to the to the microfluidic channel, ΔP is the pressure difference between two ends of the Teflon tubes, μ is the dynamic viscosity of flowing liquid in the channel ($\mu = 8.9 \times 10^{-4}$ Pa s for H_2O and 1.25×10^{-4} Pa s for D_2O), and L is the length of the microfluidic channel. The flow in the microfluidic channel was gravity-driven, with ΔP being defined by the difference in height between the D_2O and H_2O reservoir as:

$$\Delta P = \rho g H \qquad \text{Eq 3.2}$$

where ρ is the density of water (ρ = 1 × 10^3 kg m^{-3} for H_2O and 1.1 × 10^3 kg m^{-3} for D_2O), g = 9.8 m s^{-2} and H is the relative height between the end of the reservoir and that of the output tube of the Y-valve (H = 45 cm for both H_2O and D_2O due to that the reservoirs were hang at the same height). Using these parameters, the flow rate of H_2O in the microfluidic channel is 5.53 × 10^{-8} m^3 s^{-1} or 5.53 × 10^{-2} mL s^{-1}, and that of D_2O is 3.9 × 10^{-7} m^3 s^{-1} or 0.39 mL s^{-1}. The mean fluidic velocity of water is calculated as:

$$v = \frac{Q}{\pi(\frac{d_H}{2})^2} \qquad \text{Eq 3.3}$$

where Q is the flow rate, d_H is the hydraulic diameter, $d_H = \frac{2 \times width \times height}{width + height}$ for microfluidic channel with a rectangular cross-section, and d_H = 0.23 mm. Thus, the mean fluidic velocity of H_2O and D_2O is 0.33 m s^{-1} and 2.35 m s^{-1}, respectively. The Reynolds number (Re) at the flow rate in the microfluidic channel was calculated using:

$$Re = \frac{\rho d_H v}{\mu} \qquad \text{Eq 3.4}$$

Therefore, $Re = 100$ for H_2O flow and $Re = 475$ for D_2O flow. The Re for both H_2O and D_2O are smaller than the threshold for laminar flow ($Re < 2300$) [83], thus the flow is laminar in the microfluidic channel.

Based on these flow conditions and the volume of the microfluidic channel, we found it took ~ 5 s for the fluid to fully exchange in the channel (Figure 3.3).

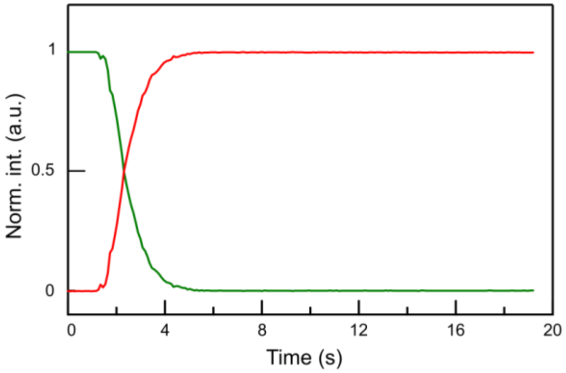

Figure 3.3 Hydrogen-deuterium exchange in a bare microfluidic channel. The exchange is completed in a few seconds. The OD (green) and OH (red) concentration vs. time were obtained by integrating the respective regions (2918 – 3810 cm^{-1} for OH and 2182 – 2780 cm^{-1} for OD) of the Raman-like (RL) spectra.

3.4 Diffusion model

In our geometry (Figure 3.4), water can only diffuse into the membrane through the interface in contact with the microfluidic water flow channel, which allows us to treat the diffusion as a one-dimensional problem. Because the side opposite the water channel is a glass coverslip and the sample is physically constricted on all other boundaries, we use reflective boundary conditions in solving Fick's second law. The Fick's second law reads:[84]

$$\frac{\partial c}{\partial t} = D\frac{\partial^2 c}{\partial^2 z} \qquad \text{Eq 3.5}$$

where c is the concentration of diffusate. The diffusion rate within the volume is proportional to the local curvature of the concentration gradient as described by Fick's second law.

In the water diffusion experiments in this work, the water channel is effectively an infinite reservoir of diffusate since fresh water is constantly being supplied in the flow channel. As the membrane is equilibrated in pure water (or deuterium oxide) before starting an experiment, we assume no diffusate is present in the membrane before switching the fluid in the flow channel. With the given boundary and initial conditions, the analytical solution to Fick's second law is given as: [85]

$$c(t) = (1 - \frac{4}{\pi}) \sum_{n=0}^{\infty} \frac{(-1)^n}{2n+1} exp(-ADCf^2 t) cos(fz) \qquad \text{Eq 3.6}$$

where f=((2n+1)π)/2L, L is the thickness of the membrane, t is the time after switching, ADC is the apparent diffusion coefficient, and z is the distance from the reflective boundary, i.e. the distance from the membrane-glass coverslip interface to the measurement (focal) point. We used finite terms of Eq 3.6. Since the initialization of flow after switching the fluid reservoirs takes ~ 5 s, the data between 0 and 5 s after switching are affected by both diffusion and channel dynamics. Therefore, the fit was performed only for those times greater than 5 s after switching, when the channel has stabilized. This leads to the deviation at early times between the fit and the experimental data, as expected. Nevertheless, using equation (1) with these constraints, we can accurately fit the concentration vs. time profiles of the diffusate moving into the membrane.

We obtained z by calibrating the location of the membrane-water interface (z_0) at a particular piezo extension (z') and by measuring L of the membrane from a caliper measurement. The mounted sample was axially scanned with the piezo near the membrane-channel interface before the H/D-exchange experiment, and the region of the spectrum containing the intensity of C-F stretch vibration (700 – 750 cm^{-1}) was integrated and plotted as a function of z' (Fig. S2B). The water-membrane interface (z_0) was determined by fitting the left half data points with a sigmoid function: $(base + \frac{max}{1+exp^{(\frac{xhalf-x}{rate})}})$ where

$xhalf = z_0$. We then moved the piezo deeper into the membrane (larger z' values) by 25 µm, and thus, $z = L - (z' - z_0)$.

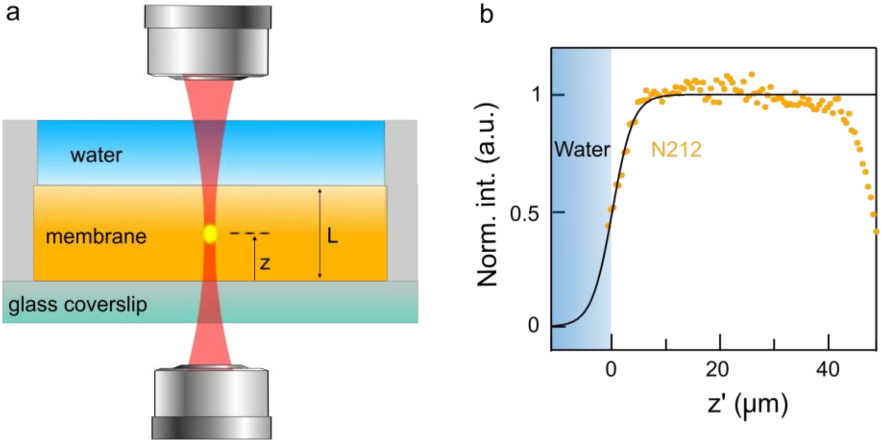

Figure 3.4 a) experimental geometry. b) the intensity of the CF stretching vibration (700 – 750 cm^{-1}) from the RL spectrum (orange dots) as a function of the axial position (z'); the black line is the fit to the sigmoid function for the data from the blue shaded region until the signal saturated from which $xhalf = z_0$.

3.5 Measuring water diffusion in Nafion® membranes

In situ, real-time water transport in Nafion® membranes was initiated by the H/D exchange in the microfluidic channel – D_2O was exchanged for H_2O (or vice versa). CARS spectra from a single voxel (500 nm × 500 nm × 3.5 µm) in the membrane were measured over time starting just before the HDX. We obtained a broadband CARS spectrum (BCARS) from 700 to 4000 cm^{-1} at time intervals of ~ 100 ms. The data processing routine to extract the quantitative Raman-like spectra was described in Chapter 2. Briefly, each raw BCARS spectrum was converted into a Raman-like spectrum using a modified

Kramers-Kronig phase-retrieval transform as described in section 2.3, with the CARS spectrum from glass serving as the non-resonant background. [72] After the transformation, a third-order polynomial was used to fit a slowly varying error phase to the regions of the spectra without resonances. This fit was subtracted from the transformed data to yield the retrieved Raman-like (RL) data shown in this work. For all data, the fingerprint (600 – 1850 cm^{-1}) and water (2850 – 3850 cm^{-1}) regions of the spectra were processed independently to minimize the error phase from the transformed CARS spectra. Therefore, we could directly measure OH and OD concentrations over time in fully hydrated membranes to quantify the effective water diffusion (Figure 3.5). The concentrations of OH/OD in the membrane were obtained by integrating the corresponding OH/OD peaks (Figure 3.5, left). Figure 3.5 shows the result of a H_2O/D_2O exchange experiment measured from N212. The apparent diffusion coefficient (ADC) of OH was extracted by fitting the data to the Fickian diffusion model discussed above.

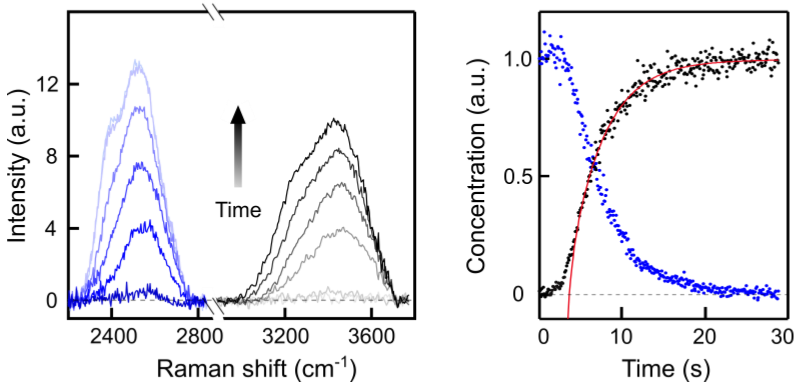

Figure 3.5 H_2O flow through a microfluidic channel over a D_2O-saturated N212 membrane. CARS spectra were continuously collected from the same focus spot in the membrane. Left: Intensity of the OH stretching vibration (black) increases with time while the intensity of the OD stretching vibration (blue, measured in parallel) decreases. Right: the OH (black) and OD (blue) concentration changes vs. time obtained by integrating the respective spectral regions; solid red line is a fit to the Fickian diffusion model described in the text. The apparent diffusion coefficient (ADC) of N212 is $3.6 \pm 0.4 \times 10^{-10}$ m^2/s (N = 6 independent experiments)

3.6 Deducing lineshapes of unknown water species using CCLS

3.6.1 Nonbulk water in fully hydrated Nafion® membranes

The spectral shape of nonbulk water (nonbulkW) in Nafion® membrane was deduced using the CCLS described in section 2.4.2 carried out with Igor Pro 6.37 (Wavemetrics). Matrix M including the measured spectra was represented with a linear combination of two components: 1) bulk-like water (bulkW), the spectral shape S_{bulk} was taken from the MilliQ H_2O; 2) nonbulkW, with unknown line shape $S_{nonbulk}$ (Eq 3.7). C_{bulk} and $C_{nonbulk}$ are respective scaling factor for bulkW and nonbulkW. The iterative CCLS global fit minimized E in order to obtain $S_{nonbulk}$. The scaling factors were also obtained from the fit.

$$M = C_{bulk} \times S_{bulk} + C_{nonbulk} \times S_{nonbulk} + E \qquad \text{Eq 3.7}$$

M contained two ($M1$) or more ($M2$) differently measured spectra to deduce the line shape of nonbulkW $S_{nonbulk}$. The nonbulk line shapes $S_{nonbulk}$ deduced from $M1$ or $M2$ are practically identical to each other, as described below.

$M1$ contains only two spectra measured from fully hydrated N212 and N117, respectively. [86] The overall intensity of OH peak in both N212 and N117 was normalized to 1, as was each component (bulkW and Unknown1). This was done to ensure that each component was equally weighted in the fit. The only constraint for nonbulkW was that all spectral components were non-negative. The initial guess for nonbulkW was either a constant value at all frequencies or the bulkW spectrum. In both cases, the fit converged successfully and yielded only one single component with a finite contribution (Figure 3.6, black).

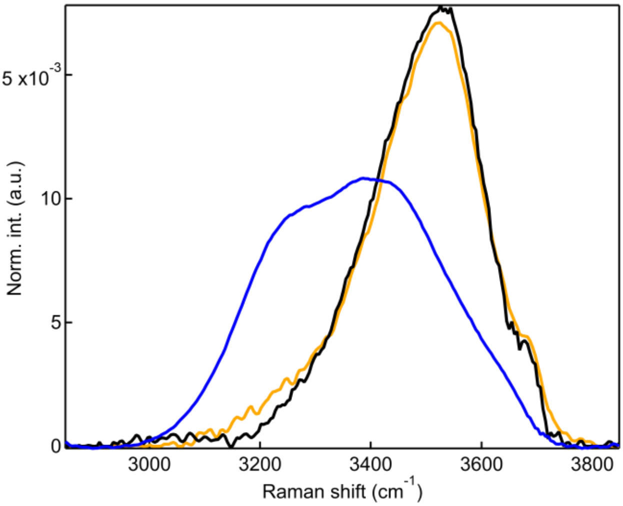

Figure 3.6 Reference OH spectrum of: bulkW (blue) captured from a water reservoir and nonbulkW (orange) derived from M2 obtained from the dry-to-wet hydration experiments, where 8 BCARS spectra were captured continuously upon hydration from N212 and another 8 BCARS spectra were captured from N117 upon hydration. The black spectrum of nonbulkW was derived from M1, which includes the hydrated OH spectra of N212 and N117. [86]

M2 contains 16 spectra that were measured from dry–to–wet hydration experiments in N212 and N117 – 8 spectra from N212 and 8 spectra from N117, and all spectra were normalized to the peak height of the CF stretching vibration. A piece (1 cm × 1 cm) of Nafion® membrane was dried under ambient condition and was placed between two glass coverslips, which were sealed with parafilm, to prevent the swelling of the membrane with one edge exposed. A droplet of water was placed in contact with the exposed membrane, and water diffused into an ambient dried Nafion® membrane as shown in Figure 3.7A.

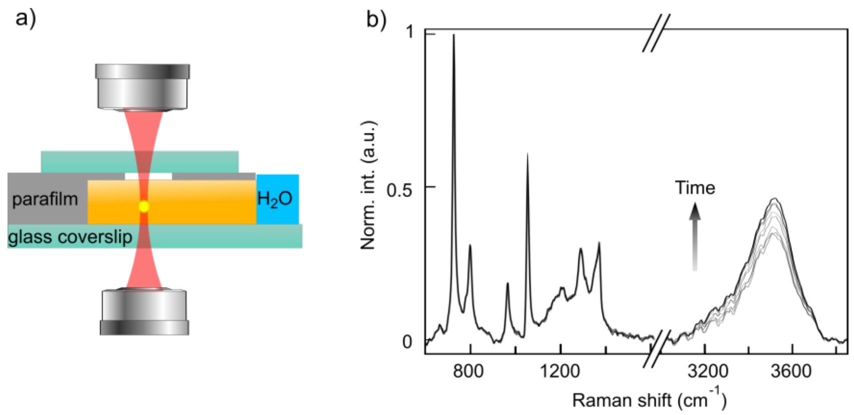

Figure 3.7 a) Setup of the dry-to-wet experiment. N212 (orange) was sandwiched by two glass coverslips and sealed by parafilm; the right edge of N212 was exposed to the water source. b) The RL spectra of the OH stretching intensity that increases as a function of time. All spectra were normalized to the peak height of the CF stretching vibration.

BCARS spectra were measured at different times during the hydration of the membrane. While not appropriate for a diffusion analysis, this experiment produced the RL spectra of N212 at various states of hydration, allowing for the derivation of the spectral shape of nonbulk water (nonbulkW) in the membrane. The sample was raster-scanned across the focal volume (21 × 21 pixels) in x-y steps of 0.5 × 0.5 µm in plane with the piezo-driven stages, and a full broadband coherent anti-Stokes Raman scattering (BCARS) spectrum was captured at each location with an acquisition time of 50 ms per pixel and with a time interval of 30 minutes between raster scans. The raw BCARS spectra were converted into Raman-like (RL) spectra using the time-domain Kramers-Kronig transform (details in Chapter 2). A BCARS spectrum taken from the bottom glass coverslip was used as the nonresonant background. RL spectra form 49 spatial pixels were averaged for all spectra shown in B.

The constraint for the nonbulkW was only non-negativity. In order to ensure each component to be reasonably weighted, each component was always normalized to have an area of 1. The initial guess for nonbulkW was randomized from 0 to 0.01 for all frequencies in the fit. The initial guess of the weight for the unknown component ($C_{nonbulk}$) was randomly chosen between 0.1 – 0.5 and that of the bulk (C_{bulk}) was 0.5. The sum of the weights of the bulkW and the unknown spectral response were constrained to be less than or equal to 1. The fit always converged successfully and yielded the spectral response shown in Figure 3.6 (orange).

3.6.2 Lineshape of HOD in water mixture

Constrained classical least squares (CCLS) global fitting was done in Igor Pro 6.32A to the spectra of the equilibrium mixtures of H_2O and D_2O. The fitting deduced a spectrum of the HOD. The inputs to the CCLS were three components: H_2O and D_2O were known, and the respective spectral shapes of pure H_2O and pure D_2O, and HOD was unknown. To ensure that all components were appropriately weighted, the total area of the spectra of the water mixture was normalized to 1, and the area of the three components was always normalized to 1. The constraint for the HOD spectral shape at all frequencies was non-negativity, and non-negative values were applied to the fit weight of each component. The initial guess for the HOD shape was either a randomized value in the range between 0 to 0.001 at all frequencies or the spectrum of the mixture with equal volume fraction of H_2O and D_2O. In both cases, the fit converged successfully and yielded the same spectral shape. The mixture spectra and residuals from the CCLS fitting routine are shown in Figure 3.8.

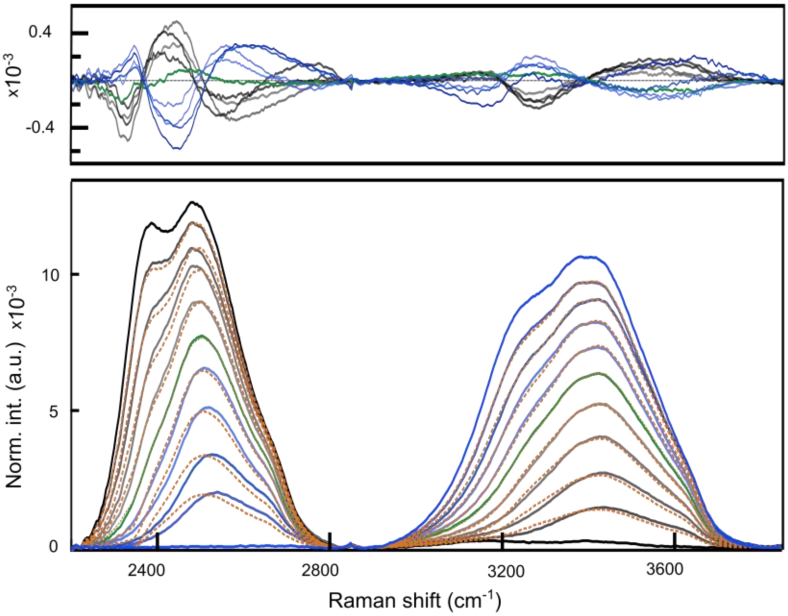

Figure 3.8 Area normalized RL spectra of H_2O-D_2O mixtures (bottom), graduated color from black to gray denoting increasing volume fraction (vol %) of added H_2O in the mixture; the green spectrum is from the mixture (50/50 vol. mixture); the dark blue is pure H_2O, and black is pure D_2O. Fit curves from the global fitting process are brown dashed lines. Top, the residuals between the fit curves and the respective spectrum.

The spectral shape of pure H_2O, pure D_2O (both were measured) and HOD (extracted from the fit) are shown in Figure 3.9. The total peak area of each spectrum in Figure 3.9 was normalized to 1, and the fractional peak area of OH region in the deduced HOD was 0.442.

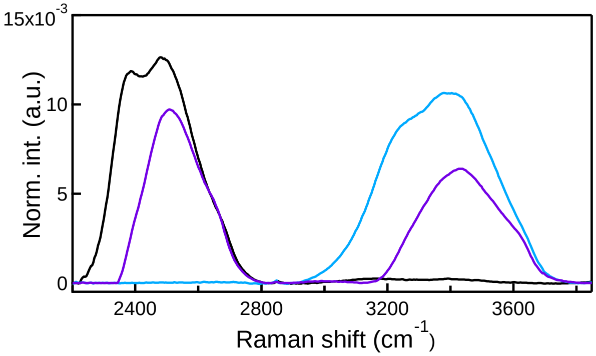

Figure 3.9 Reference spectra of the components in the H_2O-D_2O mixtures: pure H_2O (blue) and pure D_2O (black) were collected from a water reservoir, and HOD (purple) was deduced from the constraint nonnegative global fit, with the constraint that the response must be positive for all frequencies. The total peak area of these spectra was normalized to 1, and the OH peak of the HOD spectra contributes 0.442 to the total peak area of HOD.

The fractional concentration of H_2O, D_2O and HOD produced during the CCLS process are plotted as a function of volume fraction of added H_2O in the H_2O-D_2O mixtures in Figure 3.10. A theoretical concentration profile of the three components is also included in Figure 3.10 where the values of theoretical concentration were calculated based on the equilibrium of the isotopic scrambling between H_2O and D_2O as described by the following reaction:

$$\mathrm{H_2O + D_2O \rightleftharpoons 2HOD} \qquad \text{Eq 3.8}$$

The equilibrium constant of the reaction was assumed to be 4 – the geometric mean – and the theoretical concentration profiles were derived from binomial. [87] The experimental contribution profiles of bulkW and H-HOD deviate slightly from the theoretical values.

Nevertheless, the experimental values of H_2O, D_2O and HOD were very close to the theoretical values (Figure 3.10).

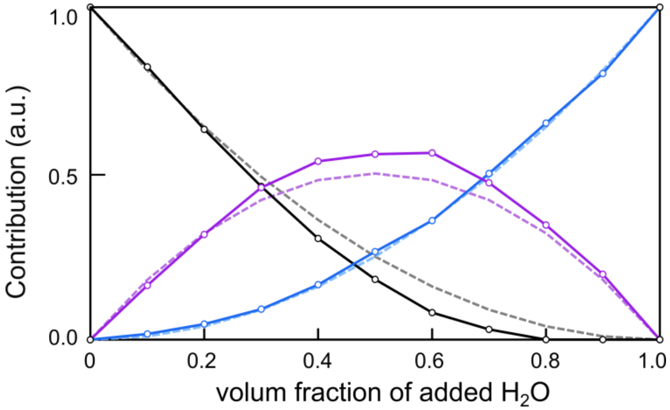

Figure 3.10 Contributions of H_2O (blue), HOD (purple) and D_2O (black). The dash lines are theoretical values of the contributions calculated based on the binomial distribution.

CHAPTER 4

STRUCTURE AND BINDING OF WATER IN NAFION® MEMBRANES

In this chapter, we study two chemically identical (N117 and N212; equivalent weight, EW = 1100 g mol^{-1}), but differently processed (N117: extruded, N212: solution cast) commercial Nafion membranes that show different water and proton transport properties. [21, 80, 81] Nafion membranes are the most widely used and studied PEMs because of their superior chemical and thermal stability and transport properties.[13, 14] The chemical structure and morphological structure of Nafion have been discussed in Chapter 1.

We demonstrate the connection between nanoscale structure and macroscopic chemical properties in two chemically equivalent, yet morphologically distinct Nafion membranes. We quantify chemical interactions between water and Nafion to deduce that extruded membranes have smaller water channels and, surprisingly, reduced sulfonic acid head group density therein compared to dispersion cast membranes. As a result, a disproportionally large amount of non-bulk water molecules exists in extruded membranes. Interestingly, these membranes also exhibit larger proton conductivity and larger water mobility compared to cast membranes. The differences in membrane physico-chemical properties, i.e. the water channel chemical constitution and local water structure, and the accompanying differences in macroscopic water and proton transport suggest that nanoscale channel chemistry is an important, yet largely overlooked parameter that influences fuel cell membrane functionality.

The results have been published at *Angewandte Chemie - International Edition*, 55 (12), 4011–4015. https://doi.org/10.1002/anie.201600219.

4.1 Experimental

4.1.1 Proton conductivity

In-plane proton conductivity of the membranes was measured by impedance spectroscopy with a two-electrode geometry using an SI 1260 impedance/gain-phase analyzer and a Novocontrol broadband dielectric converter. The membranes were immersing in MilliQ H_2O in order to ensure they were fully saturated with water during the measurement. The measurements were carried out under room temperature. The resultant proton conductivity is calculated from the Cole-Cole and Bode plots. [33]

4.1.2 Water diffusion in Nafion® membranes

Water diffusion in Nafion®212 membrane and Nafion®117 membrane was measured using the method described in Chapter 3. And the total intensity of OH and OD were quantified by integrating respective region described in Chapter 3 and the apparent diffusion coefficient (ADC) of OH was extracted by fit the time-dependent intensity of OH to the analytical solution to the Fick’s second law obtained according to the initial and boundary condition in the diffusion experiments. We used n = 2 terms of the infinite series of the analytical solution as described in section 3.4 in this chapter.

4.1.3 Deducing lineshape of unknown component

The CCLS was carried out with Igor Pro 6.37 (Wavemetrics) using an iterative global fit to the OH region of the Raman-like spectrum for the average spectrum of N117 and N212 (N = 3 spectra from three sample preparations). Details can be found in section 3.6.1. The lineshape of the deduced component (nonbulkW) as well as the known component (bulkW) are shown in Figure 4.1.

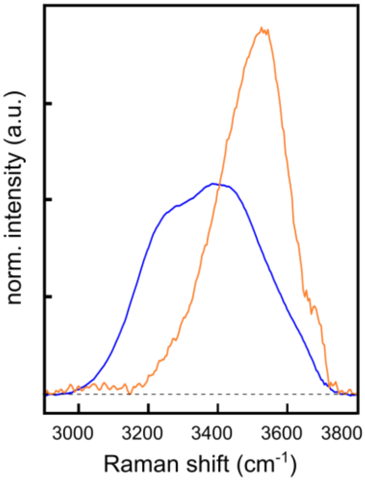

Figure 4.1 Reference spectra for CCLS fits: bulkW (blue) was collected from a water reservoir; nonbulkW (orange) was deduced in the decomposition process. Spectra were normalized to the total integrated intensity.

The shape of nonbulkW spectrum resembles reference spectra recorded from an aqueous solution of perfluoro butane sulfonic acid (Figure 4.2 red) and of air-dried Nafion (Figure 4.2 black). The lineshape of bulkW and nonbulkW has been used for decomposing the OH peak of fully hydrated N212 and that of N117 in order to maintain quantitative information of water constitution in the Nafion® membranes in this chapter.

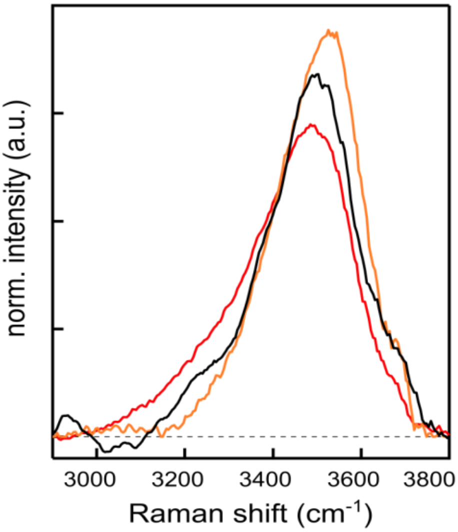

Figure 4.2 Raman-like spectrum of nonbulkW (orange line), of water in perfluoro butane sulfonic acid (1:1 molar ratio perfluoro butane sulfonic acid:water, red line) and in dry Nafion® membrane (dried for 3 days at 25 °C, 30% relative humidity, black line) in the OH region. The main peak in the perfluoro butane sulfonic acid is located at 3498 cm-1, very close to that in the nonbulkW at 3530 cm-1 and for the air-dried spectrum. All spectra show a shoulder at 3628 cm-1. Spectra were normalized to the total integrated intensity.

4.2 Distinct water constitution in N212 and N117

Using CARS spectroscopy, we measure broadband vibrational spectra of fully hydrated Nafion membranes. Figure 4.3 shows the RL spectra obtained from within fully hydrated N117 (green) and N212 (black) normalized to the CF_2 stretch band intensity of the Teflon backbone (Figure 4.3, right). Data processing procedure to obtain the RL spectra has been discussed in Chapter 3. The membranes are mounted in a homebuilt microfluidic flow cell that ensures complete hydration of the membrane during acquisition (Figure 4.3, left). Importantly, the spectral peak intensities are directly proportional to the concentration of vibrational moieties in the focal volume, allowing for quantitative band analysis.

The RL spectra of N117 and N212 are nearly identical in the fingerprint region (700 to 1600 cm^{-1}) which contains prominent Nafion stretch vibrations arising from CF_2, CS, COC and SO_3^- at 731, 803, 970 and 1057 cm^{-1}, respectively. [30] The difference spectrum between N117 and N212 (Figure 4.3, top) shows that all Nafion band positions and relative intensities are virtually indistinguishable for N117 and N212, as one might expect for identical EW polymers of the same chemical composition. The slight deviation between 1100 and 1250 cm^{-1} arises from imperfect error phase correction in our data processing routine and is not considered further in this work. [73]

At higher wavenumbers, the spectra show a broad response from the OH stretch of water that extends from ca. 3000 to 3700 cm^{-1} and reflects the water chemistry. The broad OH peak from N117 appears blue-shifted with respect to that from N212 as seen from the dispersive lineshape in the difference spectrum. Integration of the CF_2-normalized OH band over the entire range in N117 and N212 yields the same total band intensity to within 2.5%, i.e. the total number of OH groups (typically extrapolated to the number of water molecules) per CF_2 group is the same for both samples in the probe volume. The peak shift and different spectral shape, however, indicate two different chemical environments of water molecules in N117 compared to N212.

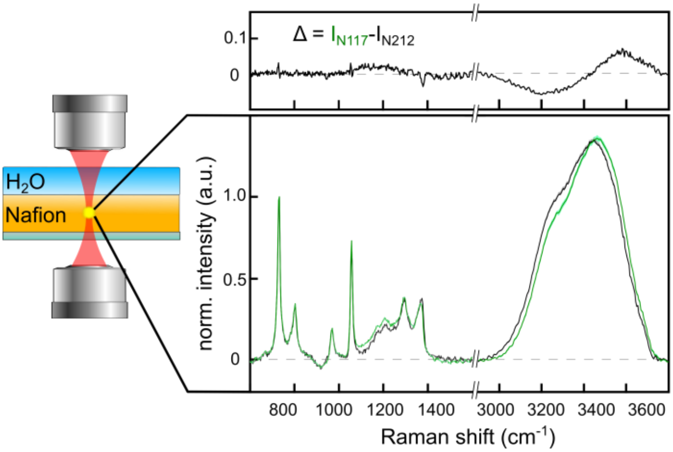

Figure 4.3 Left: Sketch of forward-scattering CARS experiment. Right bottom: Processed CARS spectra from fully hydrated N212 (black) and N117 (green) Nafion membranes. Variability from three different membrane slices of the same batch is shown as shadows to the solid line spectra. Right top: Difference spectrum I_{N212}-I_{N117}.

To gain insight into the differences in chemical interactions between water and Nafion and to identify the contribution of different water species, i.e. water molecules in different chemical environments, to the total OH stretch signal, we decompose the OH region using the CCLS routine described in *2.4.2*. [88] As a starting point, we assume that water molecules inside fully hydrated Nafion either 1) are completely surrounded by – and hydrogen bonded to – other water molecules (‘bulk-like water’, bulkW), or 2) interact (at least partially) with the Nafion membrane and therefore less with water, which we term undercoordinated non-bulk water (nonbulkW). [28] Other water species may exist, but starting with a minimum number of two components is reasonable to determine the appropriate number of sub-species that make up the total signal, in line with recent work on Nafion-water interaction. [34]

The CCLS routine employs a global fit to both N117 and N212 spectra with two component spectra: 1) a common reference spectrum from a water reservoir for bulkW (Figure 4.1 blue) and 2) a common nonbulkW spectrum that is deduced in the fitting process itself (Figure 4.1 orange). This CCLS approach constrains both N212 and N117 to contain the same two sub-species of water and produces a unique nonbulkW spectrum, as well as the fractional contributions of the bulkW and nonbulkW components to the total OH spectral intensity in each membrane.

The results of the CCLS fitting are shown in Figure 4.4. The deduced nonbulkW component has its peak maximum at 3530 cm^{-1} with a shoulder at 3678 cm^{-1}. Such high-wavenumber OH stretch bands are typically assigned to water molecules that are not tetrahedrally coordinated to four other water molecules (as is the case for bulkW molecules). [89, 90] Prominent examples for such under-coordinated OH groups are those of water in vapor, or in contact with hydrophobic interfaces where one of the two OH bonds of water molecules points towards or into the hydrophobic phase and on average experiences less hydrogen-bonding to other water molecules. [89, 91, 92] The shoulder at 3678 cm^{-1} is reminiscent of a non-hydrogen-bonded OH species. [93] Taken together, these observations strongly suggest that the nonbulkW is under-coordinated water located in proximity to the SO_3^- and CF_2 moieties of the membrane.

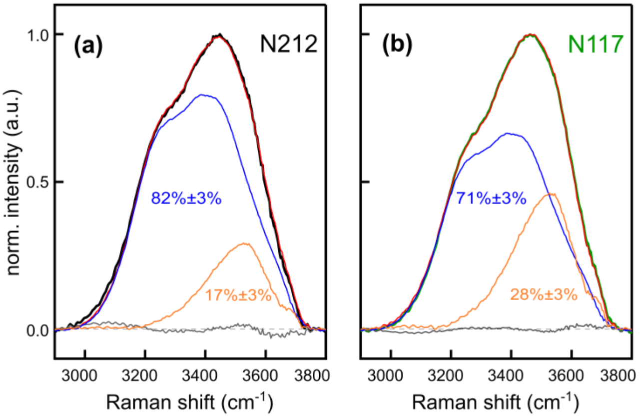

Figure 4.4 Relative contributions of bulk (blue) and nonbulk (orange) OH intensities to the overall OH stretching signal of N212 (a, black) and N117 (b, green) as obtained from CCLS. Red (green): CCLS fit to the overall OH signal of N212 (N117). Gray: fitting residual. The uncertainty in the percentages comes from three independent measurements on three different samples.

The overall water response from both N212 (Figure 4.4a, black) and N117 (Figure 4.4b, green) are fit excellently using the input spectrum from bulkW and the nonbulkW spectrum obtained from CCLS. The fit error is on average less than 3% of the measured spectral intensity at each frequency over the entire fitting range (Figure 4.4, gray). Comparing the proportion of bulkW and nonbulkW in the respective membranes, the fractional contribution of bulkW to the total amount of water in N117 (71%) is significantly smaller than the bulkW contribution of found in N212 (82%) while the nonbulkW species contribution is correspondingly higher in N117 compared to N212. The higher contribution of nonbulkW in N117 indicates a larger amount of undercoordinated water molecules that are presumably in contact with the sulfonic acid head groups and/or the hydrophobic Teflon backbone of the membrane.

The fitting results raise an interesting question: how can two Nafion membranes with identical chemical composition, i.e. chemically identical in EW and spectroscopically, have different relative contributions of bulk and nonbulk water? Molecular dynamics simulations have suggested that the nanoscale physical-chemical properties, e.g. the size [13, 14, 94] and chemical constitution [95, 96] of water channels and hydrophobic domains, play a crucial role for the overall physical-chemical properties of PEMs, in addition to the macroscale membrane chemistry and pore connectivity of water channels. However, direct experimental proof relating nanoscale chemical constitution with membrane physical chemistry for Nafion is scarce. [95-98]

4.3 Nanoscale structure determines water binding and structuring

Small-angle scattering experiments (SAXS/SANS) have shown the radius of cylindrical water channels to be 5-13% smaller in extruded than in solution-cast hydrated Nafion of 1100 g EW. [21, 24, 41, 99] It follows that the circumference of an idealized, cylindrical channel (as well as the channel surface area) is accordingly 5-13% larger for N212 compared to N117. Thus, the channel surface area-to-volume (*A/V*) ratio is 5-13% larger for N117, assuming the total length of the channels is the same, and much larger than the channel radius, for the two membranes. Recall that the Raman-like responses from the two fully hydrated membranes (Figure 4.3) show the same concentrations of Nafion (SO_3^- and COC moieties) and water (integrated OH) per CF_2 group within the focal volume. Combining our spectroscopy data with the SAXS/SANS results, we deduce relative differences in the nanoscale physical-chemical architecture of the two Nafion membranes. Since the water channels in N117 are smaller than those in N212, but both membranes show the same concentration of Nafion and water, N212 must contain fewer water channels of larger diameter and have a larger surface density of sulfonic acid head groups (SO_3^- surface density). Conversely, N117 contains more, but smaller water channels with a lower surface density of hydrophilic SO_3^- moieties across the water channel surface compared to N212. These nano-architectural differences in the chemical constitution of N117 and N212 are schematically depicted in Figure 4.5.

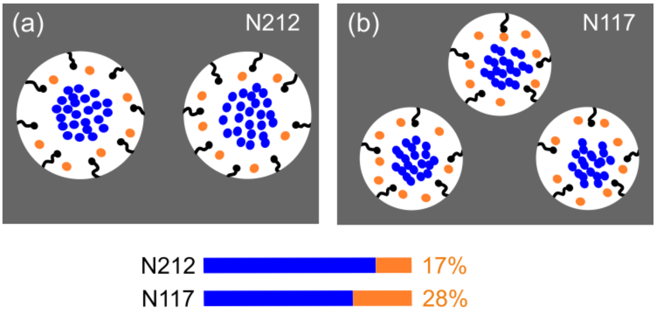

Figure 4.5 Schematic cross-sections of the different nanoscale chemical constitutions of N212 (a) and N117 (b) water channels. The total amount of water and the relative water-to-Nafion concentrations are the same for both membranes within the slab, i.e. the focal volume. Blue: bulk water; orange: nonbulk water; black: SO_3^-/COC groups; gray: Teflon backbone.

Let us now return to the different water spectra from the fully hydrated N117 and N212 membranes. The relative amounts of bulkW and nonbulkW as extracted by CCLS (Figure 4.4) for each membrane are *qualitatively* consistent with the architectural differences proposed above for the two membranes. The smaller water channel diameter (and thus larger *A/V* ratio) in N117 accommodates less bulkW species, favoring nonbulkW, i.e. water molecules that are in contact with the channel surface (with hydrophilic head group and/or hydrophobic polymer backbone) rather than with each other.

By assuming a core-shell model for the water in the channel where bulkW is core water and nonbulkW is shell water, our spectroscopic data allows us to *quantitatively* assess the thickness of the nonbulkW shell in N117 and N212 under fully hydrated conditions. Such a core-shell model was successfully employed to describe water chemistry and vibrational population dynamics of water in nano-emulsions of 1.7 to 28 nm in diameter, which is similar to the size of the Nafion channels. [65]

In our analysis, I_{nbw} (contribution of nonbulkW component) and I_{bw} (contribution of bulkW component) are fractional quantities of the total OH spectral intensity $(I_{nbw} + I_{bw})$. Each quantity is proportional to the percentage of bulkW and nonbulkW molecules, respectively, which themselves are further proportional the fractional volume of shell (nonbulkW) and core (bulkW) water in the channels (assuming a constant water density). This allows writing the nonbulkW contribution as $I_{nbw}/(I_{nbw} + I_{bw}) = (V_t - V_{core})/V_t$, where V_t and V_{core} are the total channel volume and the core water volume in the channels, respectively. Plugging in formulas for core-shell cylindrical channels, and since $I_{nbw} + I_{bw} = 1$, we arrive at $I_{nbw} = (2r_c\,t - t^2)/r_c^2$, where r_c and t are the channel radius and shell thickness, respectively. Since we know I_{nbw} from our measurements, we can estimate the thickness of shell water in the two Nafion® membranes. Starting with N212 where $I_{nbw} = 0.17$ and assuming r_c^{212} ~ 2 to 5 nm, [21, 24, 100] we calculate a shell thickness t = 0.2 to 0.4 nm which corresponds to ~ 0.5 to 1 water molecule (using a water molecular radius of 0.19 nm calculated from at a density of 1 g / mL). Note that for a flat channel structure as suggested by Kreuer et al., [14] the analogous calculation results in a slightly thicker layer of nonbulkW of about 1 to 5 water molecules.

SAXS/SANS studies report a ratio of water channel size between N117 and N212 under hydrated conditions between 0.87 and 0.95.

[24, 99] Assuming a water channel size ratio of $r_c^{117}/r_c^{212} = 0.9$, the same calculation for N117 reveals a shell thickness that is 50% larger than that of N212. This disproportionate increase in shell thickness for N117 is possibly explained by a change in water channel surface chemistry. Recalling that the concentration of SO_3^- groups is the same in N117 and N212, and that channels in N117 are smaller than in N212, the SO_3^- surface density in N117 must be lower than in N212 (Figure 4.5). Apparently, the decrease in SO_3^- surface density accompanying the reduction in water channel size in N117 causes an increase in the thickness of shell water. This change in the water arrangement likely contributes to differences in water and proton transport between the two materials (Table 4.1).

Table 4.1. Apparent water diffusion coefficients (ADC) and proton conductivities (σ). Errors are the standard deviation from 5 different measurements on different membrane sections from the same batch of membrane.

Membrane	ADC×10^{-10} (m^2/s)	σ (S/cm)
N212	3.6±0.4	0.033±0.008
N117	5.3±0.3	0.072±0.010

There have been few attempts to understand how membrane nanoscale architecture affects the (macroscopic) water and proton transport properties of PEMs. [94, 101, 102] In a full atomistic MD simulation, Jang et al. showed that different chemical constitutions, i.e. varying the spatial distribution of the same number of SO_3^- groups along polymer backbones, of N117 membranes of the same EW have a strong influence on the proton and water transport properties. They found enhanced water transport in nanostructures with segregated (non-uniformly distributed) hydrophilic domains, compared with hydrophilic domains that are equally spaced along the polymer. [95]

Our results reveal a lower SO_3^- surface density – larger distance between hydrophilic groups – in N117 compared to N212. Translating the effect predicted by Jang et al. to our experiment, it is reasonable to assume that water near the channel surface is most affected by the channel chemical constitution. As such, the motion of nonbulkW (shell water) in N117 should be less hindered along the channel surface compared to that in N212 due to lower SO_3^- surface density. Since N117 also contains a larger proportion of shell water than N212, this would lead to overall faster water transport for N117 compared to N212 – which is consistent with the diffusion results. Dynamic CARS experiments to extract ADCs of bulkW and nonbulkW and relate these with the macroscopic ADCs has been measured and the results will be discussed in Chapter 5.

4.4 Conclusions

Microscopic nonlinear Raman spectroscopy allowed us to collect vibrational spectra *in situ* within two differently cast, fully hydrated Nafion PEMs of identical chemical composition, N117 and N212, to study water-membrane physical chemistry. From spectral analysis of the Nafion region of the Raman spectrum (700 to 1600 cm^{-1}) combined with previous SAXS/SANS data, we deduce the relative differences in the nanoscale chemical constitution between the membranes. N212 has larger water channels with a denser surface coverage of SO_3^- groups compared with N117. This differential architecture manifests itself in different shapes of the water spectra (3000 to 3700 cm^{-1}) of the two PEMs. Quantitative analysis of the spectra reveals that N117 and N212 have the same total amount of water in the focal volume but contain different contributions of two distinct water species, namely bulk and nonbulk water. We observe that the relative amount of nonbulk water is disproportionally increased in N117 compared to N212.

Nanoscale chemical constitution and corresponding molecular-scale water-membrane interaction, in addition to morphology, is substantially changed for extruded (N117) versus solution cast (N212) membranes with the same EW polymer. An increase in the amount of nonbulk water beyond that expected from geometry (channel size reduction) alone in the context of a core-shell model necessitates a thicker shell of under-coordinated water in N117. Interestingly, N117 also exhibits faster water and proton transport compared to N212. The extent to which the observed transport properties result from nanoscale architectural changes and subsequent water-membrane interaction differences, or from channel tortuosity and alignment is an unresolved question that certainly requires further investigation. Nevertheless, our results highlight that future theoretical and experimental studies comparing different PEMs should include parameters that capture the impact of nanoscale channel architecture on physical chemistry to accurately interpret the underlying physics of water and proton transport in PEMs.

CHAPTER 5

HETEROGENEOUS WATER TRANSPORT IN PEM

In this chapter, we show that water transport in Nafion® PEMs is heterogeneous, with different water subspecies exhibiting distinct diffusivities with the more weakly-hydrogen-bonded nonbulk water subspecies exhibiting 4-fold faster apparent diffusivity. The overall water diffusivity in two separate Nafion® membranes was shown to be accurately described by a linear combination of the bulk and nonbulk water diffusivities weighted by the corresponding fractional amount of each species in the respective membranes. The faster diffusivity in N117 (extruded Nafion®) compared to N212 (solution-cast Nafion®) can be rationalized by N117 containing a larger fraction of nonbulk water, which results from the nanoscale constitution in N117 from extrusion processing. Our results highlight the connection of the nanoscale channel architecture on the transport properties of Nafion® PEMs and provide a clear design target of maximizing the amount of nonbulk water to optimize transport properties of PEMs.

The following results are being prepared for submission to *Angewandte Chemie International Edition*.

5.1 Experimental

5.1.1 Water diffusion in Nafion® membranes

Total water diffusivity in Nafion® membranes (N212 and N117) were measured by the H_2O / D_2O exchange experiments. The experimental details can be found in Chapter 3. The apparent diffusion coefficients

(ADC) of OH and OD were extracted by fit the quantitative time-dependent total intensity of OH and OD peaks to the analytical solution of Fick's second law as described in section 3.4. We used N = 6 terms of the infinite series of the analytical solution described in section 3.4.

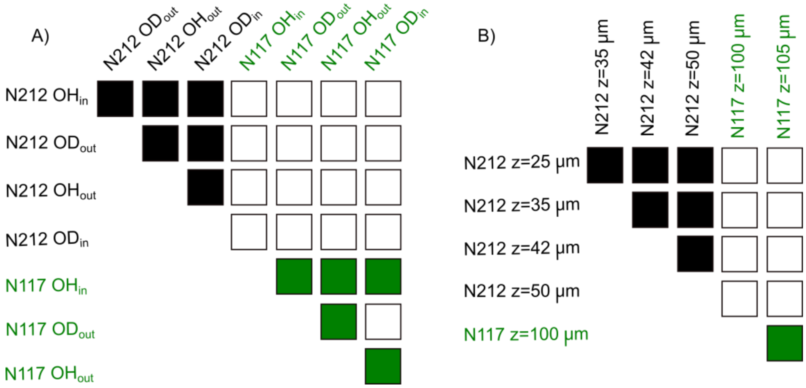

Figure 5.1 Statistical analysis of: A) ADC(OH) and ADC(OH) of respective membrane, N212 (black) and N117 (green); B) ADCs at different locations within respective membrane of N212 and N117. Black squares and green squares show statistically identical ($p<0.05$, ANOVA with Tueky's), whereas open squares show statistically significant different. The subscripts of in and out denote diffusants of OH/OD diffuses in or out of the membrane. In one typical exchange experiment, OH diffusing in a PEM is accompanied by OD diffusing out of the PEM.

The ADC(OH) is statistically identical the ADC(OD) in each Nafion membrane (N212 and N117) (Figure 5.1A), and the value of the ADC in each membrane is independent of the measurement volume in them (Figure 5.1B). The ADC in N212 is significantly smaller than that in N117 (Figure 5.1B).

5.1.2 Mutual diffusion of water

We measured the mutual diffusion of water using the experimental apparatus (Figure 5.2). A 4.2 mm thick plastic plate with a pinhole of 1.0 in diameter was mounted in our home-made flow cell. Parafilm (~ 0.15 mm thick) was used to seal the plate and glass coverslip preventing the water leakage between them.

The pinhole was pre-filled with D_2O using a syringe with 27G needle, and a D_2O flow was initiated on top of the plastic plate using our microfluidic channel. The diffusion of water into the pinhole was initiated by switching the water flow in the channel from D_2O to H_2O. BCARS spectra were recorded at 128 ms time intervals from which the quantitative RL spectra were retrieved. The exchange of water flow took approximately 5 s (see section *3.3* and Figure 3.3), while it took ~ 100 min for completing the exchange at the measurement focal volume at the bottom of the pinhole. Since the pinhole was significantly thicker than the water flow (~ 0.3 mm thick), and we measured at position almost 4.2 mm away from the water flow, the disturbed flow profile at the pinhole inlet can be neglected. Thus, the H-D exchange of the measured volume can be treated as 1-D Fickian diffusion model with a reflective boundary condition. (see section 3.4) The apparent diffusion coefficient (ADC) of OH species ADC(OH) = $(3.4 \pm 0.2) \times 10^{-9}$ m^2/s (mean ± standard deviation, N = 3 independent measurements). Decomposing the OH band into bulkW and HOD, and calculating the ADC of bulkW gave ADC(bulkW) = $(2.2 \pm 0.4) \times 10^{-9}$ m^2/s (mean ± standard deviation).

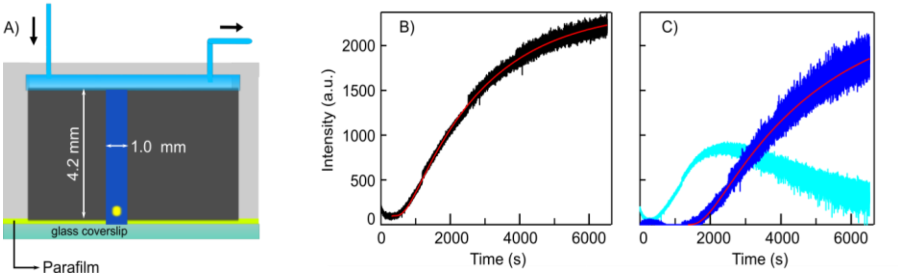

Figure 5.2 A) Diffusion apparatus for measuring water diffusion in D_2O. The pinhole diameter was 1.0 mm and the thickness of plastic plate was 4.2 mm. Parafilm (approximately 0.150 mm) was used to seal the plastic plate and glass coverslip. The yellow dot shows the focal (measurement) point. B) Time-lapsed OH peak intensity of H_2O diffusing into a D_2O-filled pinhole. Red curve is the fit of the profile to 1-D Fickian diffusion model with an ADC(OH) = 3.3×10^{-9} m^2/s. C) bulkW (dark blue) and HOD (light blue) profiles during water diffusion. The red line shows the 1-D Fickian diffusion model with an ADC(bulkW) = 2.3×10^{-9} m^2/s.

5.1.3 Decomposition of the time-lapsed RL spectra

The spectral shape of nonbulkW in this chapter was deduced from M2 as described in section 3.6.1 (Figure 3.7 orange). We deduced the HOD RL spectrum using the CCLS algorithm on spectra from a series of D_2O/H_2O mixtures (see section 3.6.2, Figure 3.8 and Figure 3.9). Using the deduced HOD lineshape with bulkW and a bulk D_2O spectra to decompose the isotopic mixtures produced concentration profiles of H_2O, D_2O, and HOD nearly identical to those predicted by the established binomial mixing rule [87, 103] (Figure 3.10), verifying the accuracy of the HOD lineshape for bulk solutions. A fourth component, in addition to bulkW, nonbulkW, and HOD, was derived by CCLS.

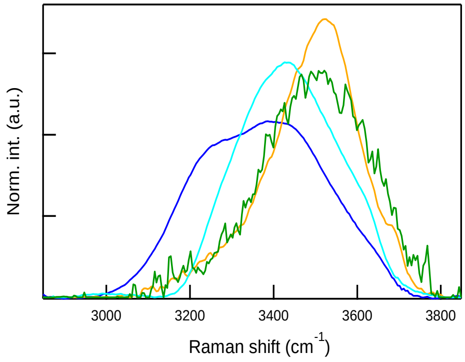

Figure 5.3 Reference spectra of bulkW (blue), nonbulkW (orange), HOD (cyan) and component4 (green). The peak area of all spectra was normalized to 1. The bulkW, nonbulkW and HOD were known components in the global fit, and component4 was derived.

Five OH spectra were taken from the dynamic data of N212 at different time points and were used for the fit. The fit had three known components (bulkW, nonbulkW and HOD are shown in Figure 5.3 as blue, orange and cyan) and one unknown component (component4). Component4 and its fit weight were constrained to non-negative. The spectral shape of component4 deduced from the fit was shown in Figure 5.3 (green). Adding component4 to decompose OH spectra did not significantly improve the fit quality as shown by the very similar residual spectrum root mean square (RMS) and % error between the fitted and measured OH spectra for 3-component and 4-compent decomposition from a time-lapsed a N212 exchange experiment (Figure 5.4).

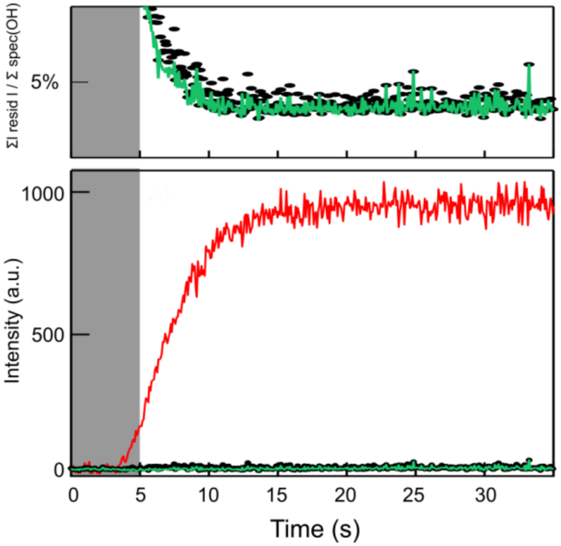

Figure 5.4 Error quantification from spectral decomposition of OH region RL spectra of H_2O-D_2O in N212 exchange using three components and four components. (Bottom) Red line shows OH intensity increase starting from ~ 4 s while black and green lines show integration of the absolute value of residual spectrum for the decomposition with three and four components, respectively. (Top) % error, defined as the ratio: (integration of the absolute value of the residual spectrum) / (sum of the OH peak), for each acquired spectrum. These quantifications show almost no improvement upon inclusion of a fourth component.

5.1.4 Other perfluorosulfonic acid (PFSA) membranes

The water transport in other perfluorosulfonic acid (PFSA) membranes was measured via the H_2O/D_2O exchange experiment. The chemical structure and the macroscale properties of these membrane are shown in

Table 5.1

Table 5.1 Properties of other PFSA-based membranes

Membranes	Polymer	EW (g mol^{-1})	Density (g cm^{-3})	Water uptake in liquid at 100 ^{o}C
Aquivion® E87-05 (E87) [104]	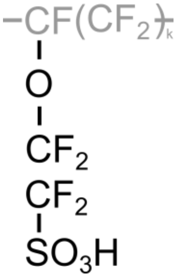 $-CF(CF_2)_k-O-CF_2-CF_2-SO_3H$	870	1.93	35 *wt*%
Aquivion® E98-05S (E98) [105]		980	1.93	25 *wt*%
NE1035 [106]	The same as N212 and N117 (Figure 1.2)	1000	1.97	43 *wt*%

As shown in Table 5.1, the Aquivion® membranes – E87 and E98 – have shorter side chain compared to the Nafion® membranes used in this work. The NE1035 is another type of Nafion®-based membrane that has more sulfonic acid groups than N212 and N117.

In order to measure the H_2O/D_2O exchange in the membranes mentioned in Table 5.1 we cut these membranes into pieces (1 cm × 5 cm in size). All membranes were cleaned using the same method discussed in section 3.1 and the cleaned membranes were stored in MilliQ H_2O before the H_2O/D_2O measurements.

5.2 H_2O/D_2O exchange in N212 and N117

We measured *in-situ*, time-dependent water transport in Nafion® membranes using the microfluidic setup (Chapter 3) to initiate H_2O-D_2O exchange within an immobilized a PEM in our BCARS microscope, as in our previous work [86]. Figure 5.5 (top left) shows a schematic of the measurement wherein a Nafion® membrane, in this case dispersion cast Nafion® 212 (N212, equivalent weight = 1100 g), was initially saturated by D_2O, representing a D_2O-equilibrated state. After switching a Y-valve to initiate exchange, BCARS spectra from the membrane were acquired at 100 ms intervals. Switching the microfluidic channel solution to H_2O took ~ 5 s in our gravity-driven, laminar flow conditions (see section 3.3 and Figure 3.3), after which H_2O diffused into the membrane and D_2O in membrane diffused out.

BCARS spectra from the Nafion® membrane during the exchange (Figure 5.5A) were processed into RL spectra (see section 2.3 and section 3.5 for experimental details) and used to quantify transport by plotting the OH and OD concentrations from the integrated amplitudes of the OH (2918 – 3810 cm^{-1}) and OD (2182 – 2780 cm^{-1}) stretching vibrations, respectively (Figure 5.5B). The time-dependent OH and OD concentrations show that the diffusion process in (N212) was complete within ~ 30 s of initially detecting the OH signal. Fitting the time-dependent OH and OD traces with an analytical solution to Fick's second law, similarly to our previous work [86] (see section 3.4 and section 5.1.1), allowed us to quantify the transport by extracting an apparent diffusion coefficient (ADC) from the traces (Eq 3.6).

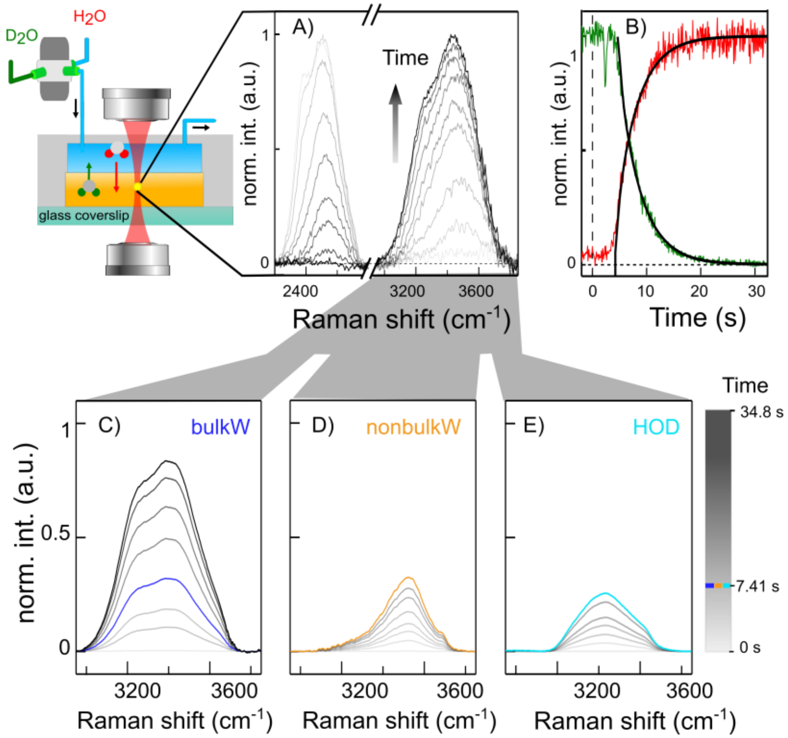

Figure 5.5 A) RL intensity of the OD stretching vibration decreases with time while the intensity of the OH stretching vibration increases during exchange. All RL spectra were normalized to the maximum value in the respective regions. B) OD (green) and OH (red) concentrations vs. time obtained by integrating the respective spectral regions; solid black lines are fits to the Fickian diffusion model described in section 3.3. Concentration profiles were normalized to their maximum value. D-E) Time-dependent spectra showing water subspecies contributions during H_2O-D_2O exchange in N212. All spectra are divided by the maximum of the OH band at t = 30 s (after exchange is complete) to show different temporal evolution.

The ADC for the integrated OH amplitude (ADC(OH) = 3.75 ± 0.10 × 10^{-10} m^2/s (mean ± standard deviation)) was statistically identical to the ADC of the integrated OD amplitude (ADC(OD) =

$3.89 \pm 0.20 \times 10^{-10}$ m^2/s (mean ± standard deviation)) in N212 (Figure 5.1) from N = 6 different membrane samples. These numbers are quantitatively consistent with our previous measurements using a slightly modified fitting protocol [86] and are consistent with other values reported for water diffusion in Nafion. [35, 39, 85, 107] Moreover, the reverse experiment – D_2O diffusing in an H_2O equilibrated membrane also shows statistically identical results (Figure 5.1), which confirms that OH and OD exchange simultaneously. Accordingly, both the OH and OD regions can be used to analyze the diffusivity of water in Nafion®; however, for simplicity, we focus on the OH region for experiments of H_2O diffusing into a D_2O-equilibrated membrane for the remainder of this work. Finally, we note that experiments from different depths and lateral positions within N212 (relative to the channel-membrane interface) showed that ADC(OH) was not depth-dependent (Figure 5.1), as expected for a nanoporous membrane that is uniform over micrometer length scales (the size of our focal volume).

5.3 Origin of the increasing OH signal

In principle three distinct sources can contribute to the signal we observe: 1) H^+ transport, 2) OH^- transport, and 3) H_2O transport in the membrane wherein mass transport is a requirement in all cases. Because we detect the OH stretching vibration, we are unable to distinguish between these different transport species and their various mechanisms. Nevertheless, since mass transport is a requirement, and the $[H^+]$ and $[OH^-]$ are more than 10^9 smaller than $[H_2O]$ for pH 7 MilliQ water, we conclude that H_2O transport is the likely dominant contribution we observe.

Proton transport and water transport in bulk water show a diffusion coefficient of ~ 4 - 8 × 10^{-9} m^2/s [108] and ~ 2.3 x 10^{-9} m^2/s, respectively, which is similar to the ADC(OH) = $3.4 \pm 0.2 \times 10^{-9}$ m^2/s

for H_2O diffusing into a D_2O-filled aperture measured in our experimental apparatus (Figure 5.2). All of these values are nearly 10-fold faster than the ADC(OH) in either of the two Nafion® membranes measured here (~ 4 × 10^{-10} m^2/s), which is consistent with the ADC of water in Nafion® determined by other methods [34, 39, 85, 109, 110]. The 10-fold discrepancy between water diffusivity in Nafion versus water (or proton) diffusivity in water can be explained by the physical barriers in the material: the tortuosity (or connectivity) and constrictions of ionic channels within the Teflon polymer matrix that certainly slow down transport [111].

Beyond quantifying the kinetics of OH appearance by integrating the OH-stretch region, time-lapsed BCARS spectroscopy allowed us to analyze the shape of the OH-stretch resonance during exchange. Previous work has revealed at least two distinct subspecies of water in Nafion® membranes: bulk water (bulkW) and nonbulk water (nonbulkW), each with a distinct spectral shape in the OH-stretch region [34, 86]. Therefore, analyzing the shape of the OH-stretch region during exchange can reveal how different water subspecies transit the membrane.

5.4 Diffusivity of water subspecies in N212 and N117

We used spectral decomposition of the OH-stretch region to analyse water subspecies transport during the H_2O-D_2O exchange. BulkW is represented by the RL response of MilliQ water, and the nonbulkW spectrum was deduced by analysing many RL spectra of N212 in different hydration states (Figure 3.7) with the CCLS global fitting algorithm (see section 3.6.1 for fitting details). In addition to bulkW and nonbulkW subspecies, exchange of D_2O for H_2O will necessarily result in an intermediate HOD species that also contributes to the OH-stretch vibration. [87, 103, 112] Therefore, for analyzing the shape of the time-dependent RL spectra, a spectral component for HOD is also required. The HOD spectral shape was deduced from a series of D_2O/H_2O mixture using CCLS as described in section 3.6.2. In principle, one would expect a bulk and nonbulk HOD subspecies for Nafion®, and therefore, we checked whether the binomial mixing held for H_2O, D_2O, and HOD in N212 equilibrated in different H_2O/D_2O mixtures using the deduced HOD lineshape. Good agreement was observed between the decomposition concentrations and those predicted by the binomial mixing rule using bulkW, nonbulkW, and HOD lineshapes (Figure 5.6). These results show that the OH-stretch mode in Nafion® during H_2O-D_2O exchange can be described in a consistent manner using these three lineshapes: bulkW, nonbulkW, and HOD.

Having established spectral shapes for the primary water subspecies contributing to the OH-stretch in the membrane, time-dependent RL spectra of H_2O-D_2O exchange in N212 were decomposed using non-negative least squares according to:

$$S_{meas} = C_{bulkW} \times S_{bulkW} + C_{nonbulkW} \times S_{nonbulkW} + C_{HOD} \times S_{HOD} + E$$

where S_{meas} is the experimental RL spectrum, C_{X} is the concentration of subspecies X, S_{X} is the subspecies X RL spectrum, and E is the error between experimental and calculated spectrum (see section 2.4.2). The time-dependent spectral contributions to the overall RL spectra OH-region from N212 during the H_2O-D_2O exchange are shown in Figure 5.5C-E. Interestingly, the HOD and nonbulkW components reach their maximum value much earlier (at t = 7.4 s) compared to bulkW.

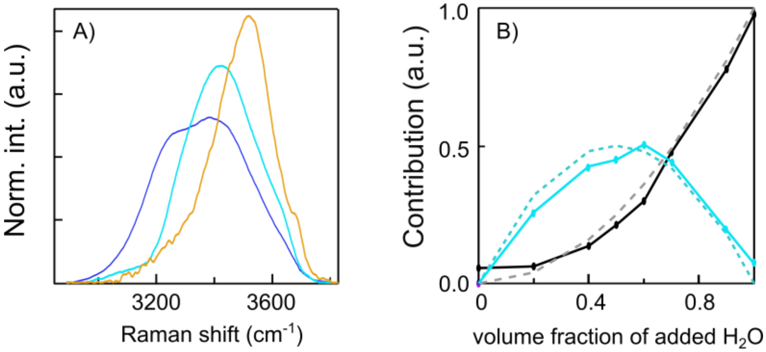

Figure 5.6 A) RL spectra used for OH region decomposition: bulkW (blue) and nonbulkW (orange); OH spectrum of HOD (cyan). Peak areas of these spectra were normalized to 1. B) Contribution of OH from H_2O (black) and that from HOD (blue) to the overall OH intensity in N212 equilibrated in different H_2O-D_2O mixtures. Dashed lines (with same color) show predicted contributions calculated from binomial mixing based on the geometric mean. Note H_2O contribution is the sum of bulkW and nonbulkW contributions.

Figure 5.7A shows the *C* values for each subspecies in N212 from all RL spectra in a representative exchange experiment. The residuals from these decompositions (Figure 5.7A insets, grey curves) are less than 5% of the total spectral amplitude, and adding a fourth component to the decomposition did not improve the fit (Figure 5.4). Figure 5.9A confirms the observation that nonbulkW (orange) appears more quickly than bulkW (dark blue) in N212. The concentration of HOD (light blue) at first increases with the appearance of nonbulkW and decreases to zero upon complete exchange, as expected, since it is a transient species that should disappear as the membrane completely fills with H_2O. The transport behavior of water was observed in three individual experiments within one N212 membrane and across N = 6 different N212 membrane samples.

Prior to analysing the concentration profiles of the subspecies with the diffusion model, we performed a control experiment to verify that the isotopic scrambling reaction $H_2O + D_2O \rightleftharpoons 2HOD$ was fast relative to our millisecond measurement timescale. With the same microfluidic setup, we measured H_2O diffusion into a 4.2 mm deep × 1 mm wide D_2O-filled aperture (Figure 5.2), decomposed the time-dependent spectra into HOD and bulkW, and calculated the ADC(bulkW) from the 1-D Fickian model (Eq 3.6). Should isotopic exchange strongly influence the bulkW signal we detect, one would expect the ADC diffusion-only (as opposed to reaction-diffusion) analysis to strongly disagree with the mutual diffusion coefficient of water. We found an ADC(bulkW) ~ $2.2 \pm 0.4 \times 10^{-9}$ m^2/s (N = 3 independent experiments) from this experiment, which is very close to the well-accepted H_2O mutual diffusion constant ($D_{H_2O} \sim 2.3 \times 10^{-9}$ m^2/s) reported in numerous experimental and theoretical studies [113, 114]. This close agreement demonstrates that a diffusion-only analysis sufficiently captures the H_2O / D_2O transport phenomena in the exchange experiments. Thus, the 1-D Fickian diffusion model was used to calculate the ADC of bulkW and nonbulkW from the time-dependent concentration profiles. We found that ADC(bulkW) = $10.1 \pm 0.9 \times 10^{-10}$ m^2/s and ADC(nonbulkW) = $2.5 \pm 0.3 \times 10^{-10}$ m^2/s (mean ± standard deviation), respectively, from N = 6 independent membrane samples (Figure 5.7B, solid bars and Figure 5.8).

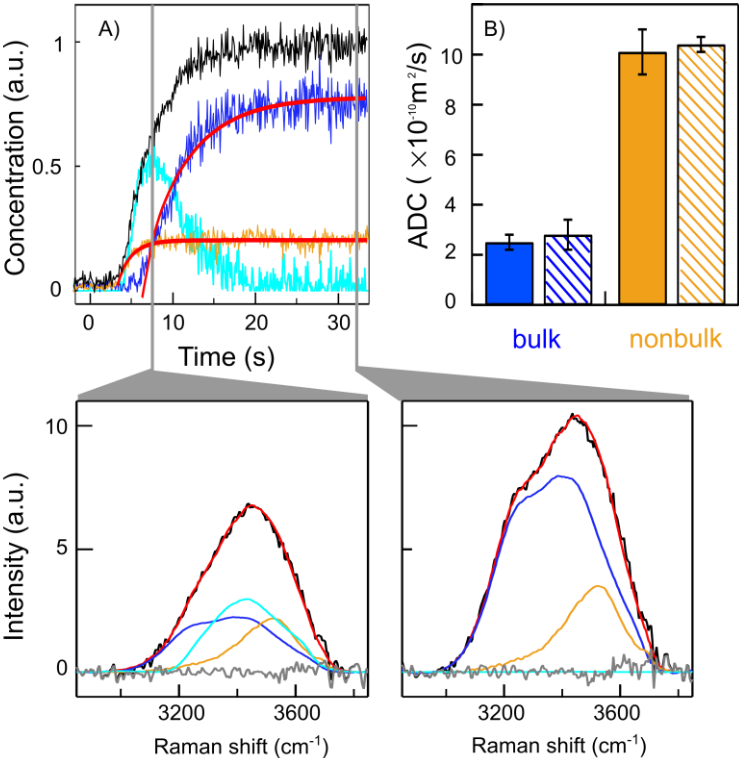

Figure 5.7 A) Decomposed concentration profiles of bulkW (blue), nonbulkW (orange) and HOD (cyan); the total normalized OH signal is shown in black. Red lines show fits to 1-D Fickian model for bulkW and nonbulkW. (Bottom) RL spectra (black) and calculated spectrum (red) at times indicated by gray vertical lines. RL spectra of subspecies of bulkW (blue), nonbulkW (orange) and HOD (blue) as well as residuals (gray) are shown on the spectral plots. B) ADC of bulkW and nonbulkW computed from diffusion fitting for N212 (solid bars) and for N117 (lined bars). ADC(bulkW) and ADC(nonbulkW) in the two PEMs were statistically identical. Error bars are standard deviations of the ADCs from three measurements in each of N = 6 independent membrane pieces for each PEM.

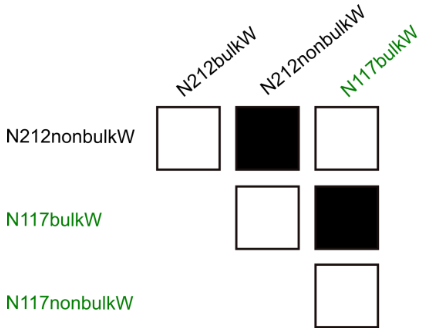

Figure 5.8 Statistical analysis of ADC(bulkW) and ADC(nonbulkW) of N212 (black) and N117 (green). Black squares indicate statistically identical ($p<0.05$, ANOVA with Tueky's), whereas white squares indicate statistically significant different.

Interestingly, at the early stages of the H_2O-D_2O exchange (Figure 5.7A), we observed that the [bulkW] / [nonbulkW] ratio was substantially smaller compared to the infinite-time (equilibrium) situation at t > 20 s. Such a long-lived non-equilibrium points to physical separation of nonbulkW and bulkW: if the two types of water coexist within the same nano channel, one would expect exchange dynamics between these populations on at least a ~ 100 picosecond time scale [64]. This would lead to instantaneous equilibration on our measurement timescale and effectively indistinguishable ADC for both bulkW and nonbulkW – which is not the case (Figure 5.7B). Based on previous work in Chapter 2 showing that N117, which has smaller ionic clusters (on average), has more nonbulkW [86], and given the broad distribution of ionic cluster sizes seen in scattering traces [12, 13], we hypothesize that smaller channels contain mainly nonbulkW while larger channels have mainly bulkW (Figure 5.9). If these channels are physically separated and only meet at intersecting points, this would support the long-lived non-equilibrium ratio of [bulkW] / [nonbulkW] observed in both N212 (Figure 5.7A) and N117 (Figure 5.10). Further support for physical separation of bulkW and nonbulkW is provided by the accurate calculation of the ADC(OH) by ADC(OH)’ – a weighted linear combination of ADC(nonbulkW) and ADC(bulkW) by the amount of each subspecies in each membrane, which indicates that the subspecies transit the membrane as separate species.

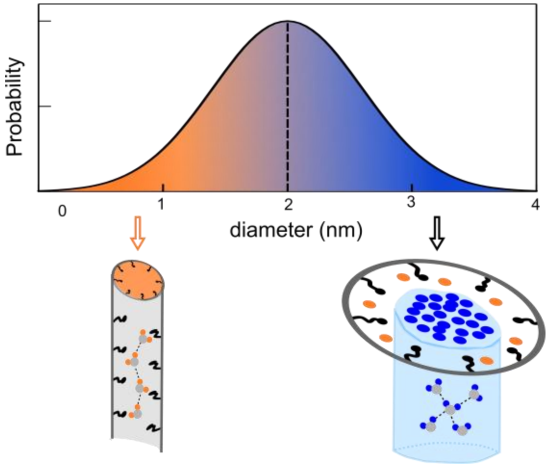

Figure 5.9 The average and full width half maximum of the distribution is from reference 4. Channel schematics (bottom) show the structure and binding of water in larger and smaller Nafion® ionic water channels. BulkW (blue) is the primary species in in larger channels while smaller channels contain mainly nonbulkW (orange). BulkW maintains interactions characteristic of bulk water, and nonbulkW forms less coordinated water network confined by the polymer (gray and black) in the smaller channels.

The finding that nonbulkW exhibits 4-fold faster transport than bulkW is qualitatively similar to other measurements (even in Nafion® membranes) showing that ‘slippery’ water has faster diffusivity than bulk water. [115, 116] Closer inspection of the spectral shape of nonbulkW in Nafion® shows that it exhibits ‘slippery’ features; it is clearly less strongly hydrogen bonded (and/or less coupled) to other water molecules compared to bulkW because the peak is strongly blue-shifted and narrower relative to that of bulkW (Figure 5.3 orange for nonbulkW and blue for bulkW) [93, 117]. Under the assumption that smaller channels contain nonbulkW, we hypothesize that the faster ADC of nonbulkW arises from a similar mechanism to that proposed for enhanced water transport in highly confined water geometries. The proposed mechanism for enhanced water transport properties in confinement is via 1-D water wires that exhibit lower barriers to hydrogen bond breaking and water rotation due to water molecules in the network having less hydrogen bonds [118] Indeed, super-diffusive water transport has been experimentally shown in carbon nanotubes (CNTs), which possess sub-nm diameters.[119] The diameter of narrow water channels (~ 1 nm) in Nafion® meets the criterion for confinement on this scale, and the shape of the nonbulkW spectrum shows that it is undercoordinated. Thus it is plausible that water confinement in smaller Nafion® channels – making it nonbulkW – may result in the strongly enhanced transport characteristics on nonbulkW. Further experiments along these lines is need to test this hypothesis.

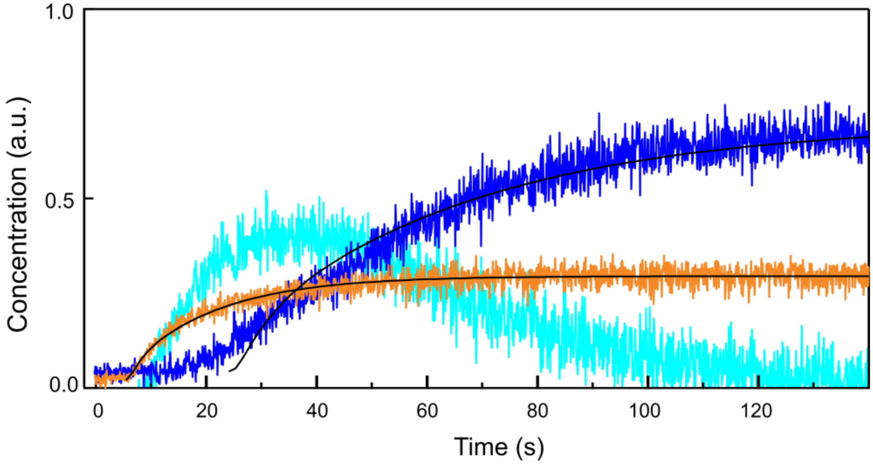

Figure 5.10 Decomposed concentration profiles of bulkW(blue), non-bulkW(orange) and HOD(cyan) for N117. Black lines show fits to 1D Fickian model for bulkW and nonbulkW.

5.5 The total water diffusivity is determined by the water subspecies

We have proposed in Chapter 4 that a weighted linear sum of the ADCs for bulk and nonbulkW could potentially reproduce the measured ADC(OH) values in N117 and N212 [86]. From the fractional concentration of each subspecies at long times after exchange (equilibrium), we observed that the amount of nonbulkW is 67% greater in N117 compared to N212 while the amount of bulkW was reduced by 15% compared to N212 – consistent with what we observed previously from static H_2O-saturated spectra [86]. Indeed, a weighted sum of the ADC(bulkW) and ADC(nonbulkW) by the equilibrium concentration of each subspecies: $\mathrm{ADC(OH)'} = \mathrm{C_{bulkW}} \times \mathrm{ADC(bulkW)} + \mathrm{C_{nonbulkW}} \times \mathrm{ADC(nonbulk)}$ almost perfectly reproduces the total measured ADC(OH) in N212 and N117. As the ADCs of the corresponding subspecies in the N212 and N117 are the same (Figure 5.7B), this shows that the faster overall OH diffusivity in N117 can be ascribed to a larger proportion of nonbulkW subspecies.

We measured the H_2O/D_2O exchange in other PFSA membranes, and decomposed the time-lapsed OH peak of the results from which we extracted the ADC of the water subspecies in these membranes. The overall water diffusivity of the PFSA membranes was also extracted from the overall intensity of the OH peak. We found that the weights sum of the ADC(bulkW) and ADC(nonbulkW) by the equilibrium concentration of each water subspecies also reproduced the total measured ADC(OH) in these membranes. (Figure 5.11A).

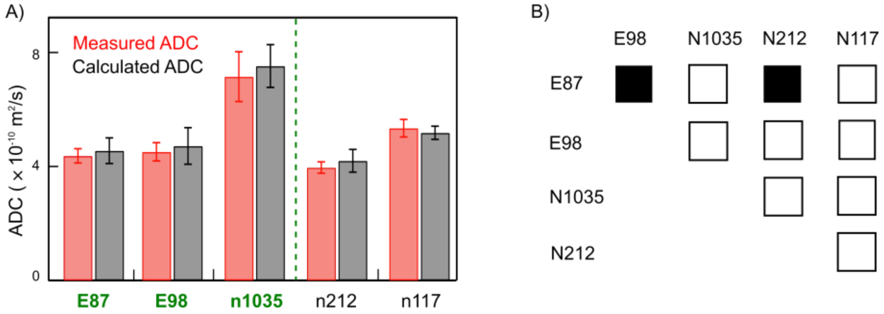

Figure 5.11 A) The total ADCs of different PFSA membranes: measured values (red bars) and calculated values (gray bars) as a linear combination of ADC(bulkW) and ADC(nonbulkW) weighted by their fractional concentration in the membrane under H_2O-saturated conditions. B) Statistical analysis of total ADCs in different PFSA membranes: black squares denote that the compared ADCs are statistically identical ($p<0.05$, ANOVA with Tukey's), whereas open squares are statistically different.

N1035 (EW of 1000 g mol^{-1}), which was made from the same Teflon backbones and sidechain structure as the N212 and N117 were with an increased amount of the side chains (as the EW in N1035 is 1000 g mol^{-1}), exhibits an accelerated overall water diffusivity which is about 1.8-fold faster than N212. As the fractional contribution of each water subspecies in N1035 is statistically identical to that of the respective subspecies in N212 (Figure 5.12). The substantially faster overall water diffusivity in N1035 results from the accelerated diffusivities of the bulkW and nonbulkW in N1035 (Figure 5.13A).

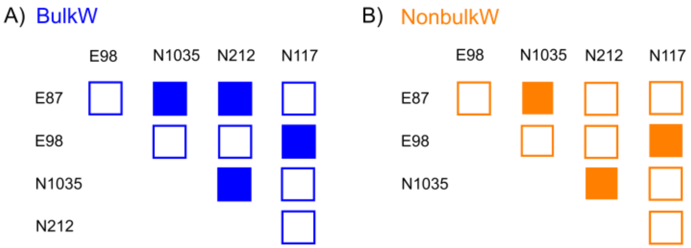

Figure 5.12 Statistical analysis of the fractional contribution of each water subspecies in different PFSA membranes: A) bulkW; B) nonbulkW. The blue and orange squares denote that the compared fractional contribution are statistically identical ($p<0.05$, ANOVA with Tukey's), whereas open squares are statistically different.

5.6 Heterogeneous water transport in different PSFA membranes

The different diffusivity of each water subspecies between N1035 and N212 (Figure 5.13) raised a question: why can the water subspecies exhibit different diffusive property? Since we used the same spectral lineshape of the subspecies to decompose the OH peak from different PFSA membrane, we (naively) expected the intrinsic diffusivity of the respectively subspecies to be the same in various PFSA membranes.

One factor known to affect transport in different Nafion® membranes in distinct ways is the tortuosity and connectivity of the water channels in the membrane, which is purely a physical barrier to the water diffusion. Indeed, the tortuosity was shown to be reduced by the decreased EW in N1035. Benziger and coworkers reported that N1035 takes up more water and exhibits a larger volume of the hydrophilic domains than N212. [41] The fractional contribution of the nonbulkW in N1035, which is determined by the surface density of sulfonic acid groups at the hydrophilic domains (or water channels), is statistically identical to that in N212, which is supported by analysis of the ratiometric quantities in the RL spectra from the polymer regions. Specifically, the $I(SO_3^-)/I(CF_2)$ are nearly identical in the two membranes. Combining our results with the results from Benziger and coworkers, we speculate that additional total water volume fraction in N1035 which reduces the tortuosity of the membrane significantly increases the diffusivity of water subspecies in N1035.

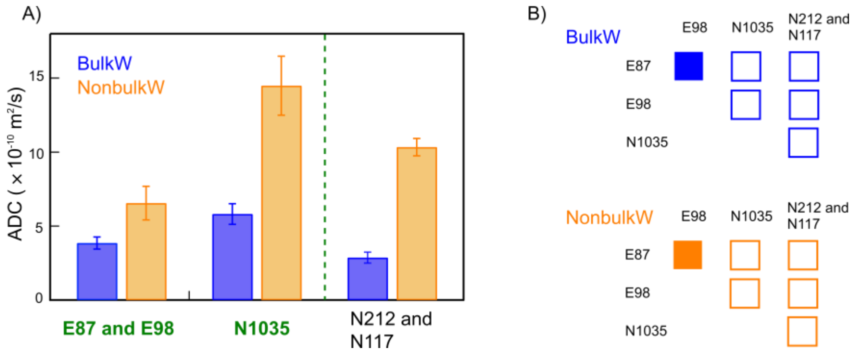

Figure 5.13 A) The ADC of the bulkW and nonbulkW in different PFSA membranes. B) Statistical analysis of the ADCs of each water subspecies in different PFSA membranes: the blue and orange squares denote that the compared ADCs are statistically identical ($p<0.05$, ANOVA with Tukey's), whereas open squares are statistically different.

Turning our attention to the Aquivion® (previously known as Hylion), we observe the following: 1) the ADC(nonbulkW) > ADC(bulkW), 2) both subspecies diffusivities and the total ADC(OH) are the same regardless of the EW (870 g mol^{-1} and 980 g mol^{-1}) and 3) the ADC for both subspecies decreased ~ 2-fold compared to N1035 (Figure 5.13). Again assuming the respective subspecies exhibit the same intrinsic diffusivity in different membranes based on that we used the same spectral lineshape of each subspecies to decompose the OH peak in Aquivion® membranes. The fact that the ADC(nonbulkW) is greater than the ADC(bulkW) (by 1.7-fold), suggests that the nonbulkW has intrinsically faster diffusivity in PFSA channels. Now, thinking about how the ADC for each subspecies compares to N1035, the fact that both decrease by nearly 2-fold suggests that the physical barriers to diffusion – the tortuosity in the Aquivion® membranes is much larger compared to N1035. Small angle X-ray scattering of Aquivion® E87-12S (E87-12S) shows broader features compared to that of N115 of which the SAXS was measured under the same condition, indicating a less-ordered phase-separated structure. Moreover, the average diameter of the water channels in E87-12S is smaller than that in Nafion® 115 membrane (N115) [120] as well as the diameter reported in other Nafion® membranes. [24, 121] The less-ordered structure of the Aquivion® membranes may result in a larger tortuosity in the membranes decreasing the diffusivity of the water subspecies.

A reasonable question at this point is why does EW seem to strongly affect Nafion® membranes but not Aquivion® membranes? Based on the ADC of the two subspecies being identical in both Aquivions®, apparently the tortuosity in both membranes is similar. Thus, the short side chain in Aquivion® strongly determines the membrane physical structure where the EW regulates the amount of total water uptake and the fractional contribution of each water subspecies. In Nafion®, with a longer side chain, the EW appears to influence not just the amount of water (and the subspecies concentration) but can also physically affect the pore tortuosity.

Last but not least, the contrast between ADC(nonbulkW) and ADC(bulkW) ($\frac{ADC(nonbulkW)}{ADC(bulkW)}$) in Aquivion® membranes is 1.7 which is smaller than that in N1035 ($\frac{ADC(nonbulkW)}{ADC(bulkW)} = 2.5$). The shorter side chains in Aquivion® membranes has been shown to exhibit slightly different structure causing a shorter distance between the water molecules compared to the N1035. [122] This could potentially induce a decrease in the diffusivity of the nonbulkW since they are believed to interact more strongly with the polymer side chains. Following this argument, the intrinsic diffusivity of the bulkW would be less affected because the bulkW do not directly interact with polymer side chains. In addition, simulation work has reported that the short side chains in PFSA membranes induces a worse connectivity in the small water channels which contain a small amount of water. [122, 123] Combined with our hypothesis that small channels contain mainly nonbulkW and larger channels contain mainly bulkW, the diffusivity of the nonbulkW is again disproportionally decreased by the decreased connectivity of the small channel network. Thus the decreased contrast between the nonbulkW and bulkW ADC in Aquivion® can be traced to a stronger effect of the change in the side chain length on nonbulkW diffusivity.

5.7 Conclusions

In this work, we quantified water and water subspecies diffusivity by the change of the OH-stretching vibration in time-lapsed BCARS vibrational spectra during H_2O-D_2O exchange. This is conceptually similar to previous work measuring water permeability in, e.g. biological cells using CARS microscopy with the added ability to spectrally analyse the OH signal. [124] Compared to our previous study [86], the current study experimentally confirms our prediction that different subspecies of water exhibit different transport rates. The diffusivity of nonbulkW is observed to be larger than that of bulkW in various PFSA membranes. In two PEMs – N212 and N117 – with identical chemical composition but different nanostructures, the subspecies diffusivities are identical and the nonbulkW diffuses about 4-fold faster than the bulkW. Increasing the total amount of sulfonic acid groups in the Nafion®-base membranes accelerate the diffusivity of each water subspecies. The diffusivity of nonbulkW in Aquivion® membranes is greatly suppressed because of the shortened side chain in these membranes.

The total water diffusivity for five different PFSA membranes can be quantitatively represented by a linear combination of the bulk-like and nonbulk-like diffusivities weighted by their fractional amount. We have shown that one efficient way to modulate overall water transport in a Nafion® membrane is modulating the chemical constitution of water in the membrane, i.e. producing a membrane with a certain EW, an increased contribution of nonbulkW is preferred to accelerate the total water transport in the Nafion® membrane.

CHAPTER 6

SURFACE DENSITY OF CHARGED SULFONIC ACID GROUPS STRONGLY AFFECTS HYDROPHOBIC FORCES IN CONFINEMENT

The surface density of charged sulfonic acid groups in ionic channels of Nafion® membrane is critical for the structuring of water and ions (protons) residing in the channels and plays an important role in the molecular transport. The mechanism through which this density affects the structuring of the water and ions is unknown largely due to experimental challenges in establishing an appropriate model system for ionic channels.

In this chapter, we present a model system for Nafion® ionic channels using self-assembled monolayers with a tunable surface density of sulfonic acid groups. Atomic force microscopy (AFM) force-distance (approach) measurements were used quantify the tip-substrate interaction between identically functionalized cantilevers and substrates, and an extended DLVO model was used to analyse the curves. We found the surface-induced hydration force exhibits biphasic behaviour with the surface density of dissociated hydrophilic sulfonic acid (charged) groups. At de-protonated sulfonic acid group densities smaller and larger than ~ 6.0×10^{17} m^{-2} (which is ~ 10-fold less than predicted in EW 1100 g/mol Nafion® when fully hydrated in neutral water), we observe hydration forces extending up to 1 Å and 10 Å, respectively. Our results suggest that water molecules and ions residing in the ionic channels of Nafion® experience different hydration forces depending on the degree of de-protonation of the sulfonic acid groups.

The results in this chapter are being prepared for submission to Physical Chemistry Chemical Physics.

Author contributions

The work in this Chapter is a collaborating work with Prof. Dr. Markus Valtiner and Laila Moreno Ostertag (Ph.D. student) at Interface Chemistry and Surface Engineering, Max-Planck-Institut für Eisenforschung GmbH, D-40237 Düsseldorf, Germany. The contributions to the work are demonstrated bellow:

X.L, K.F.D, S.H.P (from MPIP), L.M.O and M.V. (from MPIE) designed the experiments. X.L established the method for preparing the model system, conducted the contact angel measurements and did surface-enhanced Raman scattering measurements. Laila did all the AFM force-distance (approach) measurements and did the XPS measurements. L.M.O, M.V, X.L and S.H.P analysed the data of the AFM force-distance (approach) measurements.

6.1 Experimental

6.1.1 Preparation of the surfaces

We functionalized the Au-substrates with self-assembled monolayers in different thiol-ethanol solutions (Table 6.1). Two types of thiol – R-SO_3Na (90%, SIGMA-ALDRICH Chemie GmbH) and R-CH_3 (R = $HS(CH_2)_3$-) (99%, SIGMA-ALDRICH Chemie GmbH) were dissolved in ethanol (Analytical standard, SIGMA-ALDRICH Chemie GmbH) to prepare the thiol-ethanol solutions. The mole concentration of each solution was 1 mM.

Table 6.1 Mole ratio (X) of R-SO_3Na in thiol – ethanol solutions

	1	2	3	4	5	6	7
X	0	0.2	0.4	0.5	0.6	0.8	1

where R = $HS(CH_2)_3$-

Different Au-substrates were prepared for different measurements in terms of characterizing the properties of the surfaces. Methods for preparing the Au-substrates and the measurements characterizing the surfaces on respective functionalized Au-substrates are shown in Table 6.2.

Table 6.2 Preparation of the Au-substrates

Au-substrate	Methods	Purposes
Annealed Au (40) / Mica	The Au layer (40 nm) was sputter coated on Mica and was subsequently cleaned with piranha (volumetric ratio of H_2O_2 and H_2SO_4 = 1:3), MilliQ water and was dried with N_2 gas. The Au (40) / Mica substrates were flame	Static contact angle

	annealed to make an atomically flat surface.	
Roughened Au/glass	200 nm Au was deposited onto a cleaned glass slide via physical vapor deposition (PVD). The Au(200)/glass was roughened under electrochemical condition, where 0.1 M KCl solution was used and a linear potential sweep oxidation-reduction cycle (ORC) was applied to the substrates. 25 ORC cycles were applied for roughening the Au surface. [125]	Surface enhanced Raman scattering spectroscopy
Au/glue/glass	200 nm Au was deposited onto a clean cleavage Mica sheet via physical vapor deposition (PVD). A glass slide (1 cm × 1 cm) subsequently cleaned with concentrate sulfuric acid, rinsed with MilliQ H_2O, dried by N_2 gas, and then rinsed with pure ethanol (Analytical standard, SIGMA-ALDRICH Chemie GmbH) following by drying with N_2 gas. A cleaned glass slide (1 cm × 1 cm) was glued to the Au (200)/Mica using UV-active glue	XPS; Atomic force measurement

	(CONTGB-g, Budget Sensors, Bulgaria). The glass/glue/A(200)/Mica was left under UV-light for 12 h for curing the glue. Then we pealed the Mica off the glass/glue/Au(200)/Mica and made an atomically smooth Au surface. [126]	

6.1.2 Static contact angle

The macroscale hydrophobicity of the surface was characterized using static contact angle measurement, where 4 µL sessile (MilliQ H_2O) drop the SAM and the drop shape was analysist using the analysis system DSA 10. The contact angles were obtained by fitting the drop contour with Young-Laplace equation. The contact angle decreases with increasing X indicating that increasing the mole ratio of R-SO_3Na in the thiol-ethanol solutions results in increasing numbers of hydrophilic sulfonic acid groups on the surface.

6.1.3 Surface-enhanced Raman scattering (SERS) spectroscopy

The SERS active Au-substrates were prepared by electrochemically roughening an Au coated glass slide (Table 6.2). The thickness of the pristine Au layer on the glass slide is 200 nm. Surfaces with particular surface densities of sulfonic acid groups were prepared by immersing the roughened Au-substrates in the thiol-ethanol solution. The microscale distribution of sulfonic acid groups in the surfaces were characterized using surface enhanced Raman scattering (SERS) spectroscopy. We prepared the surface with different number of sulfonic acid groups on a SERS-active substrate. SERS maps were taken on a Bruker Senterra Raman microscope with an excitation wavelength of 785 nm. The laser power used in all experiment was 1 mW. A 50 × air objective (NA 0.75, OLUMPUS) was used to focus the laser onto the sample and collect the scattering signal. The x × y (11 × 11) pixels spatial images were captured from three different spots of each sample. The step size between two neighboring pixels was 0.2 µm in both x- and y- axis. All spectra were obtained with 10 s acquisition time. Backgrounds of all spectra were subtracted using an iteration-polynomial algorithm with a polynomial order of 2. [127]

6.1.4 X-ray photoelectron spectroscopy (XPS)

XPS was used to determine the thickness of self-assembled monolayer (SAM) on the Au-substrate. We used a PHI Quantera II instrument at a passing energy of 16 eV with a 24 W power. With a typical attenuation length λ of ~2 nm, the thickness T_{SAM} according to:

$$I = I_0\, e^{-\frac{T_{SAM}}{\lambda\, sin\theta}}$$

where I is the sample intensity and I_0 is the reference intensity measured from bared Au substrate; θ is the incident angle of X-ray. The thickness of was ~ 6.2 Å.

6.1.5 Atomic force microscopy force-distance (approach) measurements

Atomically flat Au/glue/glass substrates and Au-coated AFM tips (CONTGB – G, Budget sensors, Bulgaria) were immersed in 1 mM thiol-ethanol solutions with various mole ratio of R-SO_3Na (Table 6.1) to prepare surface with different surface density of sulfonic acid groups on both the substrates and the tips. Prior to the preparation, the tips were cleaned in subsequently in H_2SO_4, H_2O, H_2O and ethanol for 1 min per step. After the preparation, the surfaces on the substrate were rinsed thoroughly with ethanol to remove additional thiol molecules physically absorbing to the surfaces; the functionalized tips were carefully and subsequently rinsed with ethanol, hexane, ethanol, hexane and ethanol to remove the physically adsorbing thiol molecules.

Au substrate and Au coated tip were functionalized in the identical thiol-ethanol solution, and the interactions between the surfaces in water at pH = 1 were probed by using atomic force microscopy. AFM force curve was recorded on a JPK Nanowizard (JPK Instruments, Germany) at a sample rate of 4500 Hz. The spring constant of the used cantilevers was determined using the thermal noise method of which the value is in the range between 250 and 500 pN/nm. In a typical experiment, two sets, each containing 100 deflection-displacement curves measured from different spots, were recorded. The curves were converted into force-relative distance profiles consisting two sections: 1) extended section and 2) retract section. The extension (approach) curves are analysed and were fit to the extended DLVO model.

6.2 Characterization of the surfaces

Thiol-ethanol solutions were prepared according to Table 6.1, and surfaces with a particular surface densities of sulfonic acid groups were prepared by immersing an atomically flat Au-substrate in the appropriate thiol solution (see section 6.1.1). The surface density of sulfonic acid groups was qualitatively determined by static contact angle measurements (Figure 6.1a). The contact angle decreases with the increasing X_{SO_3}, indicating an increasing hydrophilicity of the surface, resulting from elevated numbers of hydrophilic sulfonic acid groups. To quantify the distribution of sulfonic acid groups on the surface, we used the same coating protocol on roughened gold surfaces, which were then used for surface enhanced Raman scattering (SERS) spectroscopy. SERS maps were acquired for different X_{SO_3} in 11 × 11 pixels with 0.2 × 0.2 μm^2 pixel dimensions (see section 6.1.3). Exemplary background-subtracted spectra are shown in Figure 6.1b for $X_{SO_3} = 0$ and $X_{SO_3} = 1$, which highlight spectral differences between the -CH_3 and -SO_3Na terminated thiols. The peak at 1060 cm^-

^{1} is assigned to the symmetric stretching vibration of sulfonic acid groups v(SO_3^-) [30] and that at 1095 cm^{-1} is the aliphatic carbon chain (ethyl group) vibration v(C-C) only existing in aliphatic carbon chains. [128] The intensity of the two peaks (I(C-C) and I(SO_3^-)) were obtained by integrating the wavenumber ranges denoted grey boxes in Figure 1b. The relative amount of CH_3/SO_3 was quantified as the ratio Q = I(C-C) / I(SO_3^-).

Images of Q for the surface prepared from the thiol-ethanol solution with $X_{SO_3} = 0$, 0.5, and 1 are shown in Figure 6.1b. Three different locations on these samples clearly show that Q decreases with X_{SO_3}, as expected, and none of surfaces show any microscale heterogeneity or phase separation (within our optical resolution ~ 400 nm). Figure 6.1b (black) shows the average Q value for each surface coating – computed by averaging R from all pixels in three images per surface (N = 121 per image) – decreases almost linearly with increasing X_{SO_3}. Characterization of the surfaces using SERS quantitatively showed that the surface density of sulfonic acid groups can be controlled by tuning the mole ratio X_{SO_3} in the thiol solution, and the distribution of the sulfonic acid groups are homogeneous to within our optical resolution.

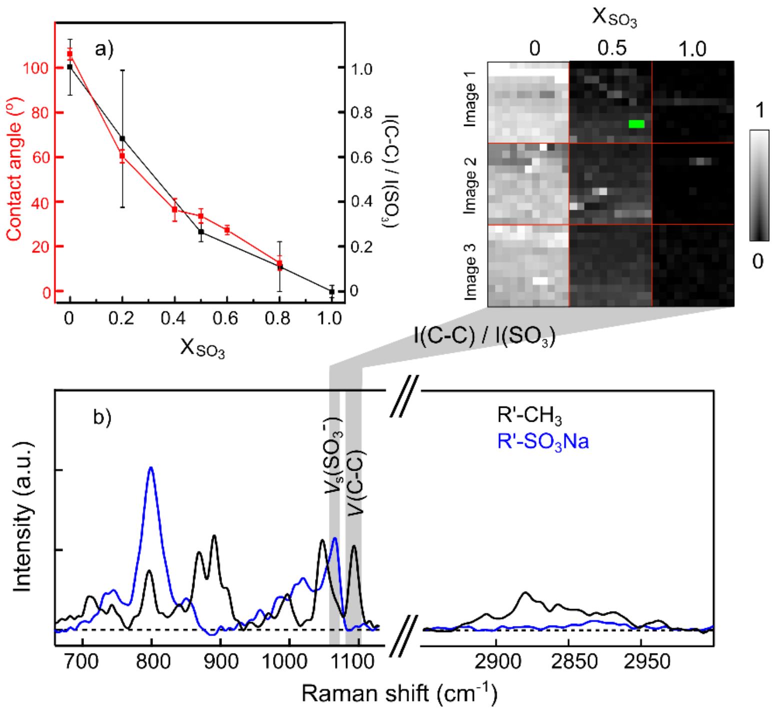

Figure 6.1 a) contact angle (red) decrease with increasing mole ratio (X_{SO_3}); relative intensity Q (black) = I(C–C) / I(SO_3) as function of X_{SO_3}. b) SERS spectra on difference surfaces: pure R’-CH_3 (dark) and pure R’-SO_3Na (blue); inset, distribution of Q = I(C-C) / I(SO_3) in pure R’-CH_3 ($X_{SO_3} = 0$), R’-SO_3Na ($X_{SO_3} = 0.5$) and pure R’-SO_3Na ($X_{SO_3} = 1$). The brighter the color, the higher the relative intensity Q with more contribution of R’–CH_3. The three images (denoted as image 1, image 2, image 3) were taken from three different spots in each sample. Error bars for I(C–C) / I(SO_3Na) in a) denote the standard deviation from averaging the relative intensities of three different images. Error bars for contact angles denote the standard deviation from average 3 experiments for each sample. R’ = (Au)–S(CH_2)$_3$–.

6.3 Force-distance curves and the extended DLVO model

To quantify the effect of dissociated sulfonic acid density on hydration forces and water structure, we used solution AFM force-distance measurements. In an attempt to mimic the cylindrically (or planar [14]) symmetry of the ionic channels, we immersed the Au-coated AFM cantilever together with the atomically smooth Au-substrate in the same thiol coating solution. As the tip was brought into contact with the substrate, this scenario approximates the channel structure in Nafion ionic channels as the tip is brought into contact with the substrate (Figure 6.2a and see experimental details in section 6.1.5). Force-distance approach curves were recorded during AFM cantilever approach in pH = 1 water. The force evolution with decreasing cantilever tip-substrate distance reflects the interactions between the surfaces and molecules in the solution, including water molecules and ions. As shown in Figure 6.2b, distinct force-distance curves profiles were observed for the surfaces with a different X_{SO_3}.

The force profile from the system with $X_{SO_3} = 0$ (Figure 6.2b, black) is attractive in over nearly the whole relative distance range prior to contact while that with $X_{SO_3} = 0.4$ (Figure 6.2b, grey) is attractive from approximately 1.5 nm to 4 nm. The surfaces coated with $X_{SO_3} = 1$ (Figure 6.2b, light grey) exhibits repulsive forces over the entire approach. The distinct force evolution of different surfaces indicates differing contributions to the total force (F_{tot}), which can be modelled as a sum of the van der Waals force, the electrostatic double-layer force, and a hydration force. These contributions to the F_{tot} are described by an extended DLVO as: [129]

$$F_{tot} = -\frac{R}{6} A(D_r) + \frac{4\pi\lambda_D\sigma^2 R}{\varepsilon\varepsilon_0} \left(e^{-\frac{D_r}{\lambda_D}} + e^{-\frac{2D_r}{\lambda_D}}\right) - 4\pi\gamma R H_y e^{-\frac{D_r}{\lambda_{H_y}}} \qquad \text{Eq 6.1}$$

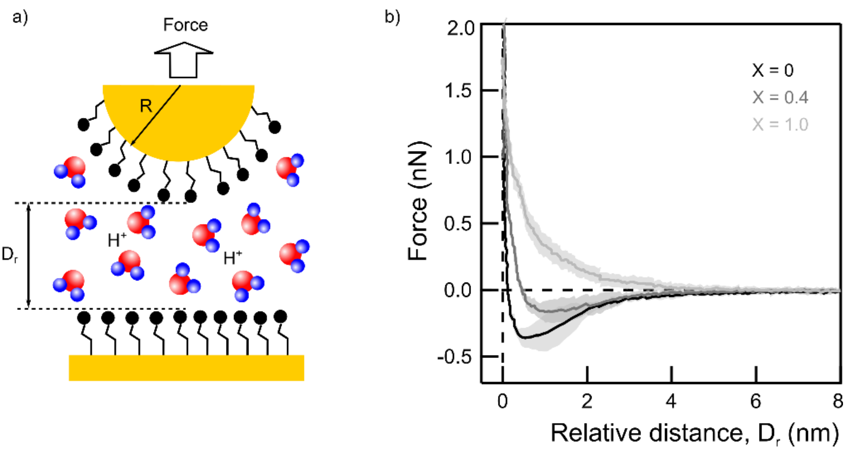

Figure 6.2 a) Schematic of the experimental setup. The force resulting from the interaction of the two surfaces – the Au AFM tip and the Au-substrate in HCl solution at pH = 1 was as the tip was approaching the substrate. The surface on the tip was kept the same as that on the substrate. b) The force versus relative distance of the tip and the substrate measured in HCl solution at pH = 1 during the approach of the tip to the substrate. Different surfaces have been prepared by varying the mole ratio (X_{SO_3}) of R-SO_3^- in the thiol-ethanol solutions: black to grey denotes increasing X_{SO_3}. The curve for each surface was obtained by averaging 15 curves measured from different spots of the respective sample.

where $\frac{R}{6}A(D_r)$ quantifies the Van der Waals force, $\frac{4\pi\lambda_D\sigma^2 R}{\varepsilon\varepsilon_0}(e^{-\frac{D_r}{\lambda_D}}+e^{-\frac{2D_r}{\lambda_D}})$ quantifies the electric double layer force and $-4\pi\gamma R H_y e^{-\frac{D_r}{\lambda_{Hy}}}$ quantifies the hydration force believed to originate from the removal of water molecules near the surface. [130] An excellent review of DLVO theory is given by Israelachvili [129] and other [131]. In Eq 6.1, R is the radius of the tip; γ = 45 mJ/m^2 is the hydrophobic tension; [129] σ is the charge density of the surface; D_r is the distance between the tip and surface (Figure 6.1a), Hydra H_y and Hydra decay length λ_{H_y} are parameters to characterize the hydration force; λ_D = 9.6133 × 10^{-10} m is the Debye length of pH=1 water; [129] ε = 8.85 x 10^{-12} F/m is the permittivity of vacuum and ε_0 = 78.3 F/m is the dielectric constant of water. The Hamaker constant $A(D_r)$ in Eq 6.1 is described as:

$$A(D_r) = \frac{A_0}{{D_r}^2} + 2\frac{\sqrt{A_0 A_1}}{(D_r + T_{SAM})} + \frac{A_1}{(D_r + 2T_{SAM})} \qquad \text{Eq 6.2}$$

where A_0= 4.5 × 10^{-21} J quantifies interaction between hydrocarbons and A_1 = 400 × 10^{-21} J quantifies the interaction between Au-tip/Au-substrate across the hydrocarbon layers; [129] T_{SAM} is the thickness of SAM and the value in this work has been determined by the XPS (see section 6.1.4).

The average force-distance curve for each different X_{SO_3} was fit with the extended DVLO model with three free parameters: the charge density (σ) in the diffuse double layer, the hydration parameter (H_y) and the hydration decay length (λ_{H_y}). The variation region for the three free parameters were constrained as: 1) σ is negative (is fixed to 0 for X_{SO_3} = 1); 2) H_y was allowed to vary in the region between -1 to 1; 3) λ_{H_y} is constrained to be non-negative. All other parameter, except for the radius of the tip R being allowed to vary between 8 nm to 40nm, were fixed.

Fit curves (red) for each system with different X_{SO_3} are shown in Figure 6.3. It is clear that the fitting is accurate for all but the lowest X_{SO_3} values. The fit curve for $X_{SO_3} = 1$ (Figure 6.3a) can only reconstruct the force at the long-range distance region (longer than 2 nm). The significantly large deviation for $X_{SO_3} = 0$ at the short-range distance may arise from additional short-ranged repulsive force in addition to the forces described in the extended DLVO model in this work.

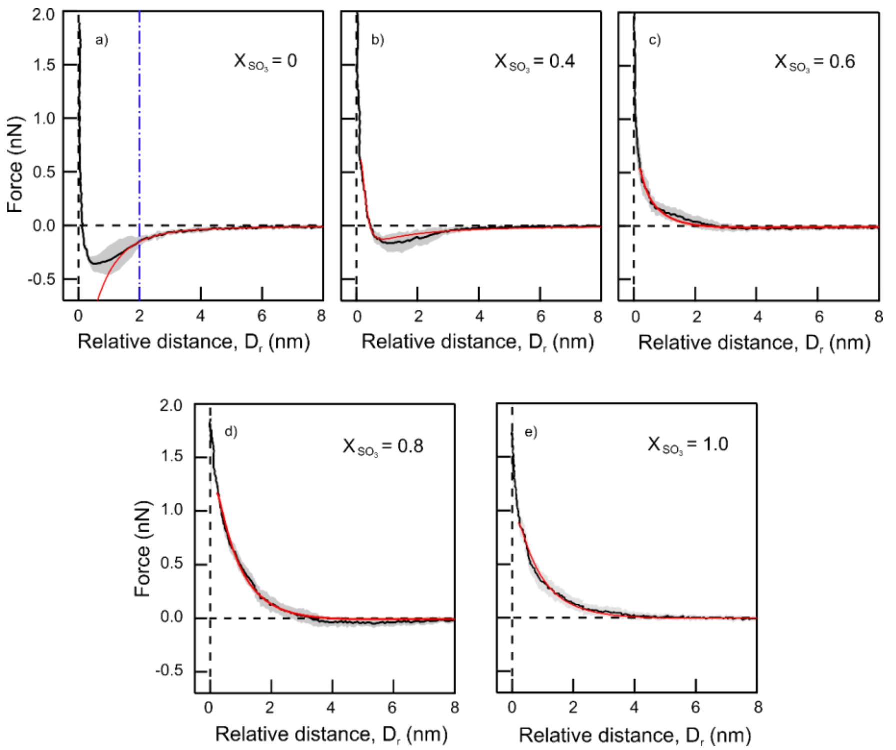

Figure 6.3 The experimental average force-distance curve (black) and fitting curve (red) to the extended DLVO model for a) $X_{SO_3} = 0$; b) $X_{SO_3} = 0.4$; c) $X_{SO_3} = 0.6$; d) $X_{SO_3} = 0.8$; e) $X_{SO_3} = 1$. For a) $X_{SO_3} = 0$, the DLVO model only reconstructed the long-range forces (only fitting the relative distance range from infinite to 2 nm).

The σ, H, and λ_{Hy} from the fit were plotted as a function of X_{SO_3}. As expected, the charge density in the diffuse double layer was negative and the magnitude appeared to increase nearly linearly with $X_{SO_3} = 0$ as σ [mC/m^2] $= -62.7 \times X_{SO_3}$ (Figure 6.4a). Given Assuming the charge density in the diffuse double layer to be about a factor of 2 smaller than the surface charge density [132], we inferred the -SO_3^- (dissociated sulfonic acid) molar surface density by assuming each SO_3^- carries one elementary charge, which yields an -SO_3^-

surface density C_s [m^{-2}] = $(7.8 \times 10^{17}) \times X_{SO_3}$. When the surface charge density was largest ($X_{SO_3} = 1$), the surface density of $-SO_3^-$ groups was ~ 7.2×10^{17} m^{-2} (and 7.8×10^{17} m^{-2} from the linear relation), which is nearly 10-fold lower than that the previously reported molar density of SO_3X self-assembled monolayers. The likely reason for this discrepancy is because the pKa of sulfonic acid groups on the surface is distinctly higher than that in a aqueous solution (pKa_{sol} ~ -2), [133, 134] and the acidic water (pH = 1) used in the measurements apparently suppressed the dissociation of the sulfonic acid groups. Similar to the charge density, parameters quantifying the hydration forces, H_y and λ_{H_y}, are plotted in Figure 6.4b and Figure Figure 6.4c. We found that with increasing X_{SO_3}, H_y is negative and gets smaller in magnitude while λ_{H_y} appears to have a step like response. When X_{SO_3} is less than 0.5, $\lambda_{H_y} \sim 1$ Å and increases to 10 Å with X_{SO_3} greater than 0.5, demonstrating that the hydration structure is strongly affected by the amount of SO_3^- on the surface.

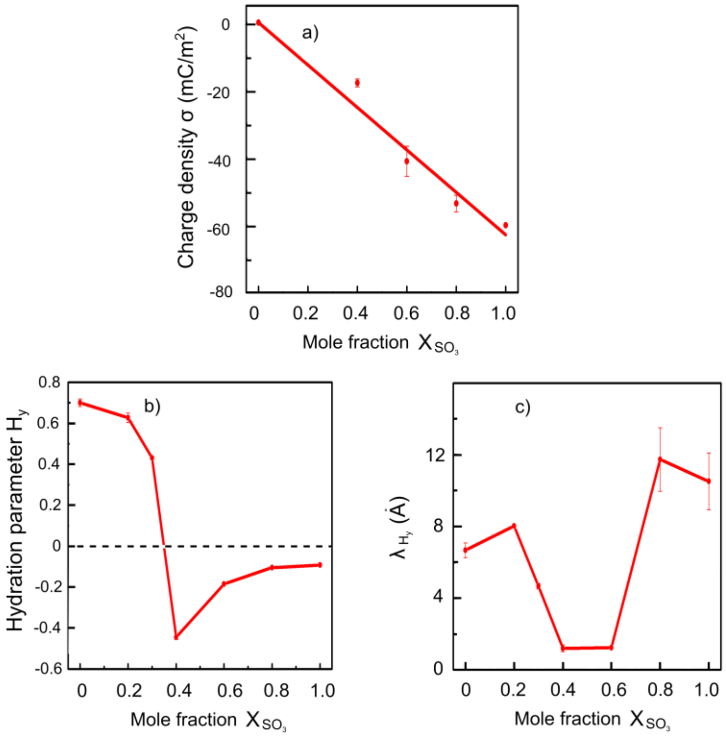

Figure 6.4 a) The charge density of the surface linearly increases with X_{SO3}; the relationship between the charge density and X_{SO_3} was obtained by fit the data to a linear function with σ = 0 for X_{SO_3} = 0 and was described as σ = -62.7 × X_{SO_3} (mC/m^2). b) and c) Hydration parameters H_y (b) and hydration decay length λ_{H_y} (c) as function of X_{SO_3}.

6.4 Estimating the surface charge density of the ionic channels in Nafion® membranes

We estimated the charge surface density of the ionic water channels in commercial Nafion® membranes as explained below. [13, 86] The surface density C_N of commercial Nafion® membranes - Nafion® 212 (N212) and Nafion® 117 (N117), each with an equivalent weight of 1100 g/mol (1 g of each dry Nafion® membrane exhibits 1/1100 mol $-SO_3H$ groups) [80, 81]. The $-SO_3$ groups are assumed to distribute within cylindrical ionic water channels in the Nafion membranes [13], and the surface density C_N [#/m^2] of $-SO_3H$ groups is written as $C_N = \#(SO_3H)/A$, where A is the surface area of the cylindrical channel. A is given as 2 × V × (1/L + 1/r), where V is the volume of the channel, L is the total length of all the water channels and r is the radius of the water channels. Assuming L >> r, we obtained $A \approx 2 \times V \times (1/r)$. Then, the surface density of $-SO_3H$ in the ionic channel of a Nafion® membrane is given as:

$$C_N \approx \frac{\#(SO_3H)}{2 \times V \times \frac{1}{r}}$$

It has been reported that a dry Nafion membrane with EW 1100 g/mol absorbs approximately 26 wt% when fully hydrated in liquid water. [41, 110] In other words, 1 g of the dry Nafion® membrane takes up 0.26 g of water when the membrane is fully hydrated. Therefore, the volume of water in the fully hydrated membrane is calculated as $0.26/\rho_{H_2O}$ where ρ_{H_2O} is the density of water in the membrane. For simplicity, we assume the ρ_{H_2O} equals that of bulk water density (10^3 kg/m^3). Assuming the volume of water channel equal to the volume of the water in the membrane, V can be written as $V = 0.26/\rho_{H_2O}$. The

#(SO_3H) is given as 1/1100 [mol] × N_A [mol^{-1}] for 1 g of dry Nafion® membrane. In our previous work [86] we have found that the water volume in the fully hydrated N212 is identical to that in the N117. However, the average radius (r) of the ionic channels in N212 and in N117 is ~ 2.3 nm and 2.0 nm, respectively. [24, 121] Therefore, we obtained C_N(N212) = 2.4 × 10^{18} m^{-2} and the C_N(N117) = 2.1 × 10^{18} m^{-2}. As the -SO_3H groups have been reported to be all deprotonated in the fully hydrate2.3/2.0

d Nafion® membranes [30], we obtained the surface charge density C_s for N212 and N117 as 2.4 × 10^{18} m^{-2} and 2.1 × 10^{18} m^{-2} mol/m^2 respectively..

6.5 Surface charge density affects hydration force

We developed a model system based on self-assembly of thiol-functionalized surfaces with varying ratio of CH_3 and SO_3Na groups and created surfaces capable of supporting different charge densities in a repeatable and predictable way. Measuring AFM tip-surface force-distance curves on thiol-functionalized Au surfaces with varying degrees of SO_3 coverage (X_{SO_3}) allowed us to extract parameters of the hydration force and charge density. Our motivation for this study was to understand how the surface density of SO_3^- affects hydration forces and water structuring in Nafion membranes as means to understand the downstream effects on transport properties. Therein, Figure 6.5 shows a plot of the hydration force parameters, H_y and λ_{H_y} as function of surface density of (SO_3^-). In Figure 6.4, we showed that the hydration decay length λ_{H_y} showed two plateaus for different (X_{SO_3}), and Figure 6.5 shows that the inflection point corresponds to an SO_3^- surface density of 7.2 × 10^{17} m^{-2}. At charge densities greater than this value, λ_{H_y} = 10 Å, almost an order of magnitude larger than that with C_s lower than 7.2 × 10^{17} m^{-2}. The results indicate that a surface with larger surface charge manifests a long-range and strong effect on the structuring of water molecules and ions near the surface.

Based on the equivalent weight of typical Nafion® membranes (1100 g / mol SO_3) and the measured size for ionic channels, [80, 81] we estimated the SO_3^- surface density in the ionic channels for a fully (pH 7) hydrated membrane (details in section 6.4). Our calculation shows that for Nafion®, the SO_3^- surface density is ~ 2.4×10^{18} m^{-2}, which is about 10-fold larger than the C_s of all the surfaces in this work (Figure 6.5). As the hydration parameter and hydration decay length saturate when the surface charge density reaches 6.0×10^{17} m^{-2}, we surmise that the surface of ionic channels in Nafion® membranes exhibits similar values for the hydration parameter and hydration decay length as those in the saturated region of C_s from our experiment.

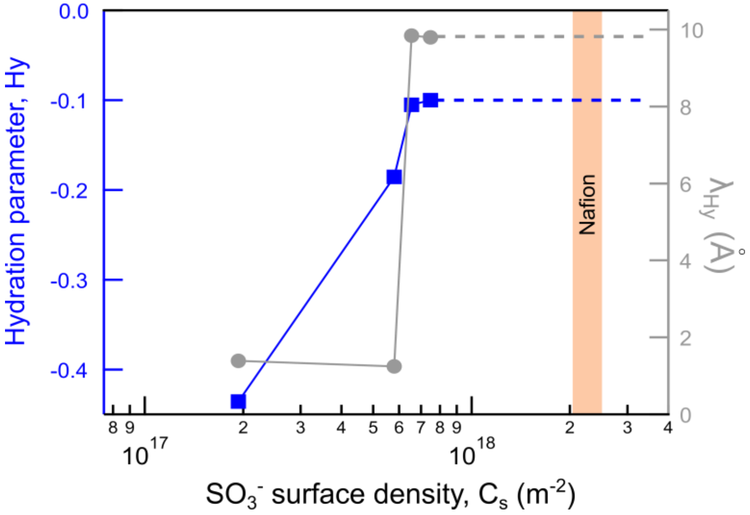

Figure 6.5 Hydration parameter H_y (blue, squares) and λ_{H_y} (gray, circles) with respect to the surface charge density C_s. The orange area denotes the surface charge density of the ionic channels in fully hydrated Nafion® membranes.

Certainly, as PEFMCs often operate with differing degrees of hydration, the SO_3^- surface density may decrease. Therefore, we hypothesize that the step change in hydration force parameters at lower SO_3^- surface density may correlate with very different transport rates and in the membranes.

6.6 Conclusions

We established a model surface to mimic the surface of ionic channels in Nafion® membranes. By varying the surface density of sulfonic acid (and methyl) groups and measuring the force arising from the interactions between identically-coated surfaces in acidic solution, we found that surfaces with an SO_3^- surface density higher than 6.0×10^{17} m^{-2} exhibit long-range hydration forces with decay length of ~ 10 Å. The hydration force is hydrophilic, and its amplitude saturates when the SO_3^- surface density is higher than 6.0×10^{17} m^{-2}. An estimated calculation for fully hydrated Nafion® (EW = 1100 g/mol) ionic channels shows that the SO_3^- surface density is 10-fold larger than that accessed in our experiments, suggesting that water feels a long-range and hydrophilic interaction from the channel surfaces under hydrated.

CHAPTER 7

FUTURE DIRECTIONS

In my project, I have investigated the chemical constitution of water in fully hydrated Nafion membranes and probed the water transport in different PEM membranes using nonlinear Raman spectroscopy. The structuring of water in the nanoscale-structured ionic water channels is affected by the surface charge density of the channels. I found that a nanoscale structure with a larger fractional concentration of under-coordinated water in Nafion membranes leads to faster macroscale water transport in the membranes.

Future studies, in terms of water transport in PEMs under real running condition of PEMFC, determination of water diffusivity in different membrane materials, as well as investigation of the degradation mechanism of the membrane, are exciting next steps directly accessible based on my work. An experimental plan for each work will be briefly described below.

7.1 Water transport in an operating PEMFC

There is a discrepancy between the hydration state of the PEM in the microfluidic cell in this project and that in a real PEMFC operation. In the real running condition of a PEMFC, the PEM is never fully hydrated; instead, the hydration state of the PEM is adjusted by the relative humidity of the hydrogen gas (the fuel) at the anode electrode of the PEMFC and is affected by the water content produced by the electrochemical reaction at the cathode electrode of the PEMFC. Water transport in a PEM at different hydration states should be investigated in order to approach the operating condition of a PEMFC, and this requires modification of the microfluidic cell used in this project.

Instead of directing a water flow onto the PEM, humidified gas should be used. The new microfluidic cell can be designed as shown in Figure 7.1. [48] The H_2O/D_2O exchange experiment will be conducted by switching the H_2O-humidified gas to D_2O-humidified gas. Identical relative humidity (RH) is required for both of the humidified gases to reduce the swelling of the sample under investigation. In addition, the RH of the gas can be controlled by mixing the wet gas bubbled through liquid water with dry gas, and the RH will be monitored with a hygrometer. [135]

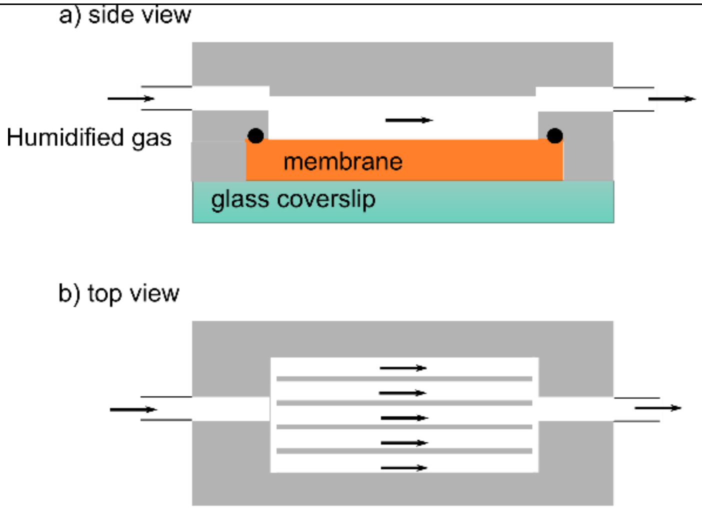

Figure 7.1 Schematic of the microfluidic cell using humidified gas. Gray, Perspex side with multiple channels carved into it; the ribs are designed for reducing the floating and drifting of the membrane.

7.2 Water diffusivity in different membrane materials

The method measuring H_2O/D_2O exchange by CARS can be used to probe water diffusivity in membrane materials other than PEM membranes where water transport is critical. One example is anion exchange membranes, and quantifying the water diffusivity in these membranes is very important in their application in separation science. I have worked with two types of experimental anion exchange membranes (shown below) – poly (benzimidazole)-based membranes (PBI) and poly (phenylene oxide)-base membranes (QPPO) and performed preliminary measurements on water diffusivity.

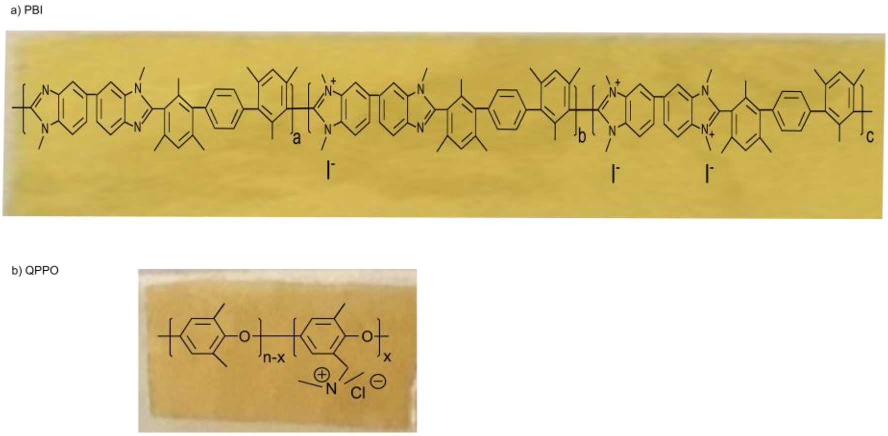

Figure 7.2 Molecular structure of anion exchange membranes: a) PBI; b) QPPO.

The inferred water diffusivity of these different membranes along with N212 and N117 is shown in Figure 7.3. The PBI membrane exhibits the smallest water diffusivity while N117 exhibits the fastest. One can, in principle, measure the water diffusivity in a wide variety of membrane materials using the method in this project and create a database of water diffusivity within the membranes. The database will benefit the evaluation of water transport properties in novel membrane materials and guide the membrane development for different applications including PEMFC [100], AEMFC [136], and for instance, vanadium flow battery (an energy storage system) [137].

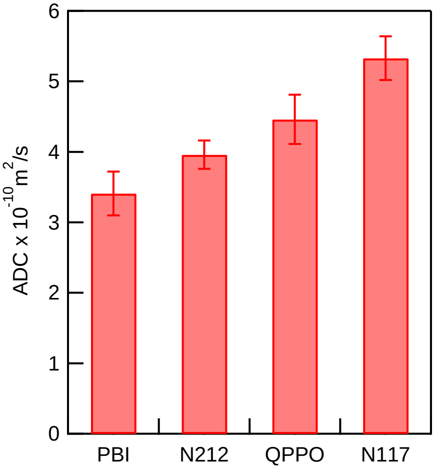

Figure 7.3 Water diffusivity in different membrane materials: PBI and QPPO are anion exchange membrane; N212 and N117 are proton exchange membranes.

7.3 Degradation of membranes

The degradation of the PEM, another critical issue for PEMFCs, was completely outside the scope of the work in this thesis. One has to suppress the degradation of PEM in order to obtain a long lifetime of the PEMFC. [138] The degradation mechanism must be elucidated in order to prevent or suppress the degradation. Vibrational Raman scattering spectroscopy can provide chemical information regarding the degradation of the materials. Molecular information can be obtained to determine the mechanism of the degradation in the PEM and could principally be done under in situ operation conditions.

BIBLIOGRAPHY

[1] Y. Wang, K. S. Chen, J. Mishler, S. C. Cho, and X. C. Adroher, "A review of polymer electrolyte membrane fuel cells: Technology, applications, and needs on fundamental research," (in English), *Applied Energy,* vol. 88, no. 4, pp. 981-1007, Apr 2011.

[2] T. Yoshida and K. Kojima, "Toyota MIRAI Fuel Cell Vehicle and Progress Toward a Future Hydrogen Society," *Interface magazine,* vol. 24, no. 3, pp. 45-49, 2015.

[3] W. Dai *et al.*, "A review on water balance in the membrane electrode assembly of proton exchange membrane fuel cells," *International Journal of Hydrogen Energy,* vol. 34, no. 23, pp. 9461-9478, 2009.

[4] S. Tsushima and S. Hirai, "In situ diagnostics for water transport in proton exchange membrane fuel cells," *Progress in Energy and Combustion Science,* vol. 37, no. 2, pp. 204-220, 2011.

[5] L. Carrette, K. a. Friedrich, and U. Stimming, "Fuel Cells - Fundamentals and Applications," *Fuel Cells,* vol. 1, pp. 5-39, 2001.

[6] C. R. Buie *et al.*, "Water management in proton exchange membrane fuel cells using integrated electroosmotic pumping," *Journal of Power Sources,* vol. 161, no. 1, pp. 191-202, 2006.

[7] D. E. Curtin, R. D. Lousenberg, T. J. Henry, P. C. Tangeman, and M. E. Tisack, "Advanced materials for improved PEMFC performance and life," *Journal of Power Sources,* vol. 131, pp. 41-48, 2004.

[8] L. Li, J. Zhang, and Y. Wang, "Sulfonated poly(ether ether ketone) membranes for direct methanol fuel cell," *Journal of Membrane Science,* vol. 226, pp. 159-167, 2003.

[9] F. Wang, M. Hickner, Y. S. Kim, T. A. Zawodzinski, and J. E. McGrath, "Direct polymerization of sulfonated poly(arylene ether sulfone) random (statistical) copolymers: candidates for new

proton exchange membranes," (in English), *Journal of Membrane Science,* vol. 197, no. 1-2, pp. 231-242, Mar 15 2002.

[10] C. H. Lee, H. B. Park, Y. M. Lee, and R. D. Lee, "Importance of Proton Conductivity Measurement in Polymer Electrolyte Membrane for Fuel Cell Application," *Industrial & Engineering Chemistry Research,* vol. 44, no. 20, pp. 7617-7626, 2005.

[11] J. P. Owejan, J. J. Gagliardo, J. M. Sergi, S. G. Kandlikar, and T. A. Trabold, "Water management studies in PEM fuel cells, Part I: Fuel cell design and in situ water distributions," *International Journal of Hydrogen Energy,* vol. 34, no. 8, pp. 3436-3444, 2009.

[12] T. D. Gierke, G. E. Munn, and F. C. Wilson, "The Morphology in Nafion Perfluorinated Membrane Products, as Determined by Wide-Angle and Small-Angle X-Ray Studies," (in English), *Journal of Polymer Science Part B-Polymer Physics,* vol. 19, no. 11, pp. 1687-1704, 1981.

[13] K. Schmidt-Rohr and Q. Chen, "Parallel cylindrical water nanochannels in Nafion fuel-cell membranes," *Nature Materialser,* vol. 7, pp. 75-83, 2008.

[14] K.-D. Kreuer and G. Portale, "A Critical Revision of the Nano-Morphology of Proton Conducting Ionomers and Polyelectrolytes for Fuel Cell Applications," *Advanced Functional Materials,* vol. 23, pp. 5390-5397, 2013.

[15] M. Fujimura, T. Hashimoto, and H. Kawai, "Small-angle X-ray-scattering study of perfluorinated ionomer membranes. 1. Origin of two scattering maxima," *Macromolecules,* vol. 14, pp. 1309-1315, 1981.

[16] M. Fujimura, T. Hashimoto, and H. Kawai, "Small-Angle X-ray Scattering Study of Perfluorinated Ionomer Membranes. 2. Models for the Ionic Scattering Maximum," *Macromolecules,* vol. 15, pp. 135-144, 1982.

[17] G. Gebel and J. Lambard, "Small-Angle Scattering Study of Water-Swollen Perfluorinated Ionomer Membranes," *Macromolecules,* vol. 30, pp. 7914-7920, 1997.

[18] G. Gebel, "Structural evolution of water swollen perfluorosulfonated ionomers from dry membrane to solution," *Polymer,* vol. 41, pp. 5829–5838, 2000.

[19] G. Gebel and O. Diat, "Neutron and X-ray Scattering: Suitable Tools for Studying Ionomer Membranes," *Fuel Cells,* vol. 5, pp. 261-276, 2005.

[20] H. G. Haubold, T. Vad, H. Jungbluth, and P. Hiller, "Nano structure of NAFION: a SAXS study," (in English), *Electrochimica Acta,* vol. 46, no. 10-11, pp. 1559-1563, Mar 15 2001.

[21] M. H. Kim, C. J. Glinka, S. A. Grot, and W. G. Grot, "SANS study of the effects of water vapor sorption on the nanoscale structure of perfluorinated sulfonic acid (NAFION) membranes," *Macromolecules,* vol. 39, pp. 4775-4787, 2006.

[22] N. H. Jalani and R. Datta, "The effect of equivalent weight, temperature, cationic forms, sorbates, and nanoinorganic additives on the sorption behavior of Nafion®," *Journal of Membrane Science,* vol. 264, no. 1-2, pp. 167-175, 2005.

[23] W. Y. Hsu and T. D. Gierke, "Ion transport and clustering in nafion perfluorinated membranes," *Journal of Membrane Science,* vol. 13, pp. 307-326, 1983.

[24] A. Kusoglu, K. T. Cho, R. A. Prato, and A. Z. Weber, "Structural and transport properties of Nafion in hydrobromic-acid solutions," *Solid State Ionics,* vol. 252, pp. 68-74, 2013.

[25] B. Dreyfus, G. Gebel, P. Aldebert, M. Pineri, M. Escoubes, and M. Thomas, "Distribution of the "micelles" in hydrated perfluorinated ionomer membranes from SANS experiments," *Journal de Physique,* vol. 51, no. 12, pp. 1341-1354, 1990.

[26] F. I. Allen, L. R. Comolli, A. Kusoglu, M. A. Modestino, A. M. Minor, and A. Z. Weber, "Morphology of hydrated as-cast Nafion revealed through cryo electron tomography," *ACS Macro Letters,* vol. 4, 2015.

[27] H. W. Rollins *et al.,* "Nanoscale metal sulfides in perfluorinated ionomer membranes," (in English), *Journal of Materials Chemistry,* vol. 10, no. 9, pp. 2081-2084, 2000.

[28] M. Falk, "An Infrared Study of Water in Perfluorosulfonate (Nafion) Membranes," (in English), *Canadian Journal of Chemistry-Revue Canadienne De Chimie,* vol. 58, no. 14, pp. 1495-1501, 1980.

[29] C. K. Knox and G. A. Voth, "Probing Selected Morphological Models of Hydrated Nafion Using Large-Scale Molecular Dynamics Simulations," *The Journal of Physical Chemistry B,* vol. 114, no. 9, pp. 3205-3218, 2010.

[30] A. Gruger, R. André, T. Schmatko, and P. Colomban, "Nanostructure of Nafion® membranes at different states of hydration An IR and Raman study," *Vibrational Spectroscopy,* vol. 26, pp. 215-225, 2001.

[31] N. B. Calthup, L. H. Daly, and S. E. Wiberley, *Introduction to infrared and Raman spectroscopy*. ACADAMIC PRESS, INC. (LONDON) LTD. 2nd, 1975.

[32] S. Quezado, J. C. T. Kwak, and M. Falk, "An infrared study of water-ion interactions in perfluorosulfonate (Nafion) membranes," *CAN. J. CHEM.*, vol. 62, pp. 958-967, 1984.

[33] Y. Sone, P. Ekdunge, and D. Simonsson, "Proton conductivity of Nafion 117 as measured by a four-electrode AC impedance method," (in English), *Journal of the Electrochemical Society,* vol. 143, no. 4, pp. 1254-1259, Apr 1996.

[34] Q. Zhao, P. Majsztrik, and J. Benziger, "Diffusion and interfacial transport of water in Nafion," *Journal of Physical Chemistry B,* vol. 115, pp. 2717-2727, 2011.

[35] T. Takamatsu, M. Hashiyama, and A. Eisenberg, "Sorption Phenomena in Nafion Membranes," *Journal of Applied Polymer Science*, vol. 24, pp. 2199-2220, 1979.

[36] D. T. Hallinan and Y. A. Elab, "Diffusion and Sorption of Methanol and Water in Nafion Using Time-Resolved Fourier Transform Infrared-Attenuated Total Reflectance Spectroscopy," *J. Phys. Chem. B* vol. 111, pp. 13221-13230, 2007.

[37] H. L. Yeager and A. Steck, "Cation and Water Diffusion in Nation Ion Exchange Membranes: Influence of Polymer Structure," *J. Electrochem. Soc.* , vol. 128, pp. 1880-1884, 1981.

[38] A. Goswami, A. Acharya, and A. K. Pandey, "Study of Self-Diffusion of Monovalent and Divalent Cations in Nafion-117 Ion-Exchange Membrane," 2001.

[39] G. Suresh, Y. Scindia, A. Pandey, and A. Goswami, "Self-diffusion coefficient of water in Nafion-117 membrane with different monovalent counterions: a radiotracer study," *Journal of Membrane Science,* vol. 250, no. 1-2, pp. 39-45, 2005.

[40] E. M. Davis, C. M. Stafford, and K. A. Page, "Elucidating Water Transport Mechanisms in Nafion Thin Films," *ACS Macro Letters,* vol. 3, no. 10, pp. 1029-1035, 2014.

[41] Q. Duan, H. Wang, and J. Benziger, "Transport of liquid water through Nafion membranes," *Journal of Membrane Science,* vol. 392-393, pp. 88-94, 2012.

[42] D. T. Hallinan, M. G. De Angelis, M. Giacinti Baschetti, G. C. Sarti, and Y. A. Elabd, "Non-Fickian Diffusion of Water in Nafion," *Macromolecules,* vol. 43, no. 10, pp. 4667-4678, 2010.

[43] S. Tsushima, K. Teranishi, and S. Hirai, "Water diffusion measurement in fuel-cell SPE membrane by NMR," *Energy,* vol. 30, no. 2-4, pp. 235-245, 2005.

[44] M. Klein, J.-C. Perrin, S. Leclerc, L. Guendouz, J. Dillet, and O. Lottin, "Anisotropy of Water Self-Diffusion in a Nafion Membrane under Traction," *Macromolecules,* vol. 46, no. 23, pp. 9259-9269, 2013.

[45] G. Suresh, A. K. Pandey, and A. Goswami, "Self-diffusion coefficients of water in Nafion-117 membrane with multivalent counterions," *Journal of Membrane Science,* vol. 284, no. 1-2, pp. 193-197, 2006.

[46] S. C. Yeo and a. Eisenberg, "Physical Properties and Supermolecular Structure of Perfluorinated Ion-Containing (Nafion) Polymers.," *Journal of Applied Polymer Science,* vol. 21, pp. 875-898, 1977.

[47] S. Motupally, A. J. Becker, and J. W. Weidnera, "Diffusion of Water in Nafion 115 Membranes," *Journal of The Electrochemical Society,* vol. 147, pp. 3171-3177, 2000.

[48] Y. Tabuchi, R. Ito, S. Tsushima, and S. Hirai, "Analysis of in situ water transport in Nafion® by confocal micro-Raman spectroscopy," *Journal of Power Sources,* vol. 196, no. 2, pp. 652-658, 2011.

[49] M. Hara, J. Inukai, K. Miyatake, H. Uchida, and M. Watanabe, "Temperature dependence of the water distribution inside a Nafion membrane in an operating polymer electrolyte fuel cell. A micro-Raman study," *Electrochimica Acta*, vol. 58, pp. 449-455, 2011.

[50] M. Hara *et al.*, "Micro-Raman study on water distribution inside a Nafion membrane during operation of polymer electrolyte fuel cell," *Electrochimica Acta,* vol. 82, pp. 277-283, 2012.

[51] H. Ericson *et al.*, "Confocal Raman Spectroscopic Investigations of Fuel Cell Tested Sulfonated Styrene Grafted Poly(vinylidene fluoride) Membranes," *Journal of The Electrochemical Society,* vol. 149, no. 2, p. A206, 2002.

[52] H. Matic, A. Lundblad, G. r. Lindbergh, and P. Jacobsson, "In Situ Micro-Raman on the Membrane in a Working PEM Cell," *Electrochemical and Solid-State Letters,* vol. 8, no. 1, p. A5, 2005.

[53] P. Huguet, A. Morin, G. Gebel, S. Deabate, A. K. Sutor, and Z. Peng, "In situ analysis of water management in operating fuel

cells by confocal Raman spectroscopy," *Electrochemistry Communications,* vol. 13, no. 5, pp. 418-422, 2011.

[54] K. Kunimatsu, B. Bae, K. Miyatake, H. Uchida, and M. Watanabe, "ATR-FTIR study of water in Nafion membrane combined with proton conductivity measurements during hydration/dehydration cycle," *J Phys Chem B,* vol. 115, no. 15, pp. 4315-21, Apr 21 2011.

[55] S. Naudy, F. Collette, F. Thominette, G. Gebel, and E. Espuche, "Influence of hygrothermal aging on the gas and water transport properties of Nafion® membranes," *Journal of Membrane Science,* vol. 451, pp. 293-304, 2014.

[56] S. Ochi, O. Kamishima, J. Mizusaki, and J. Kawamura, "Investigation of proton diffusion in Nafion®117 membrane by electrical conductivity and NMR," *Solid State Ionics,* vol. 180, no. 6-8, pp. 580-584, 2009.

[57] H. Wang *et al.*, "Nafion-bifunctional silica composite proton conductive membranes," *Journal of Materials Chemistry,* vol. 12, no. 4, pp. 834-837, 2002.

[58] S. Slade, S. A. Campbell, T. R. Ralph, and F. C. Walsh, "Ionic Conductivity of an Extruded Nafion 1100 EW Series of Membranes," *Journal of The Electrochemical Society,* vol. 149, no. 12, p. A1556, 2002.

[59] A. Farrukh *et al.,* "Polymer brush functionalized SiO2 nanoparticle based Nafion nanocomposites: a novel avenue to low-humidity proton conducting membranes," *Polym. Chem.,* vol. 6, no. 31, pp. 5782-5789, 2015.

[60] J. Ostrowska and A. Narebska, "Infrared Study of Hydration and Association of Functional-Groups in a Perfluorinated Nafion Membrane .1.," (in English), *Colloid and Polymer Science,* vol. 261, no. 2, pp. 93-98, 1983.

[61] M. Laporta, M. Pegoraro, and L. Zanderighi, "Perfluorosulfonated membrane (Nafion): FT-IR study of the state of water with increasing humidity," *Physical Chemistry Chemical Physics,* vol. 1, pp. 4619-4628, 1999.

[62] D. E. Moilanen, I. R. Piletic, and M. D. Fayer, "Tracking Water's Response to Structural Changes in Nafion Membranes," *J. Phys. Chem. A,* vol. 110, pp. 9084-9088, 2006.

[63] D. E. Moilanen, I. R. Piletic, and M. D. Fayer, "Water Dynamics in Nafion Fuel Cell Membranes: the Effects of Confinement and Structural Changes on the Hydrogen Bond

Network," *J Phys Chem C Nanomater Interfaces,* vol. 111, no. 25, pp. 8884-8891, 2007.

[64] M. D. Fayer and N. E. Levinger, "Analysis of Water in Confined Geometries and at Interfaces," *Annual Review of Analytical Chemistry,* vol. 3, pp. 89-107, 2010.

[65] I. R. Piletic, D. E. Moilanen, D. B. Spry, N. E. Levinger, and M. D. Fayer, "Testing the core/shell model of nanoconfined water in reverse micelles using linear and nonlinear IR spectroscopy," *J. Phys. Chem. A* vol. 110, pp. 4985-4999, 2006.

[66] D. B. Spry, A. Goun, K. Glusac, D. E. Moilanen, and M. D. Fayer, "Proton Transport and the Water Environment in Nafion Fuel Cell Membranes and AOT Reverse Micelles," *Journal of the American Chemical Society,* vol. 129, pp. 8122-8130, 2007.

[67] P. W. Majsztrik, M. B. Satterfield, A. B. Bocarsly, and J. B. Benziger, "Water sorption, desorption and transport in Nafion membranes," *Journal of Membrane Science,* vol. 301, no. 1-2, pp. 93-106, 2007.

[68] A. C. Albrecht, "On the Theory of Raman Intensities," *The Journal of Chemical Physics,* vol. 34, no. 5, pp. 1476-1484, 1961.

[69] J. P. R. Day *et al.*, "Quantitative Coherent Anti-Stokes Raman Scattering (CARS) Microscopy," *The Journal of Physical Chemistry B,* vol. 115, pp. 7713-7725, 2011.

[70] Y. Liu, Y. J. Lee, and M. T. Cicerone, "Fast extraction of resonant vibrational response from CARS spectra with arbitrary nonresonant background," *Journal of Raman Spectroscopy,* vol. 40, no. 7, pp. 726-731, 2009.

[71] R. W. Boyd, *Nonlinear Optics*, 3 ed. ACADAMIC PRESS.

[72] Y. Liu, Y. J. Lee, and M. T. Cicerone, " Broadband CARS spectral phase retrieval using a time-domain Kramers-Kronig transform," *Optics Letters,* vol. 34, no. 9, pp. 1363-1365, 2009.

[73] C. H. Camp, Y. J. Lee, and M. T. Cicerone, "Quantitative, comparable coherent anti-Stokes Raman scattering (CARS) spectroscopy: correcting errors in phase retrieval," *Journal of Raman Spectroscopy,* pp. n/a-n/a, 2015.

[74] J. Felten, H. Hall, J. Jaumot, R. Tauler, A. de Juan, and A. Gorzsás, "Vibrational spectroscopic image analysis of biological material using multivariate curve resolution–

alternating least squares (MCR-ALS)," *Nature Protocols,* vol. 10, pp. 217-240, 2015.

[75] A. de Juan, J. Jaumot, and R. Tauler, "Multivariate Curve Resolution (MCR). Solving the mixture analysis problem," *Anal. Methods,* vol. DOI:10.103, p. x, 2014.

[76] O. Alter, P. O. Brown, and D. Botstein, "Singular value decomposition for genome-wide expression data processing and modeling," *Proceedings of the National Academy of Sciences,* vol. 97, pp. 10101-10106, 2000.

[77] D. W. Marquardt, "An Algorithm for Least-Squares Estimation of Nonlinear Parameters," *Journal of the Society for Industrial and Applied Mathematics,* vol. 11, pp. 431-441, 1963.

[78] K. Levenberg, "A method for the solution of certain non-linear problems in least squares," *Quarterly of Applied Mathematics,* vol. 2, pp. 164-168, 1944.

[79] M. K. Transtrum and J. P. Sethna, "Improvements to the Levenberg-Marquardt algorithm for nonlinear least-squares minimization," *arXiv preprint arXiv:1201.5885,* p. 32, 2012.

[80] Dupont. Nafion® Membranes N115,N117,N1110 Datasheet [Online].

[81] Dupont. Nafion® Membranes NR211 and NR212 Datasheet [Online].

[82] S. P. Sutera and R. Skalak, "The History of Poiseuille's Law," *Annual Review of Fluid Mechanics,* vol. 25, pp. 1-20, 1993.

[83] G. m. Mala, and Li, D., "Flow Characteristics of Water in Microtubes," *International Journal of Heat and Fluid Flow,* vol. 20, pp. 142-148, 1999.

[84] J. Crank, *The mathematics of diffusion*, second ed. 1975, p. 414.

[85] D. T. Hallinan and Y. a. Elabd, "Diffusion of Water in Nafion Using Time-Resolved Fourier Transform Infrared - Attenuated Total Reflectance Spectroscopy," pp. 4257-4266, 2009.

[86] X. Ling, M. Bonn, S. H. Parekh, and K. F. Domke, "Nanoscale Distribution of Sulfonic Acid Groups Determines Structure and Binding of Water in Nafion Membranes," *Angewandte Chemie - International Edition,* vol. 55, pp. 4011-4015, 2016.

[87] F. O. Libnau, A. A. Christy, and O. M. Kvalheim, "Determination of the Equilibrium Constant and Resolution of the HOD Spectrum by Alternating Least-Squares and Infrared Analysis," *Appl. Spectrosc.,* vol. 49, pp. 1431-1437, 1995.

[88] K. F. Domke *et al.*, "Tracing catalytic conversion on single zeolite crystals in 3D with nonlinear spectromicroscopy," *J Am Chem Soc,* vol. 134, no. 2, pp. 1124-9, Jan 18 2012.

[89] Q. Du, E. Freysz, and Y. R. Shent, "Surface Vibrational Spectroscopic Studies of Hydrogen Bonding and Hydrophobicity," *Science,* vol. 264, pp. 826-828, 1994.

[90] Q. Du, R. Superfine, E. Freysz, and Y. R. Shen, "Vibrational Spectroscopy of Water at the Vapor Water Interface," (in English), *Physical Review Letters,* vol. 70, no. 15, pp. 2313-2316, Apr 12 1993.

[91] Y. T. Lee and Y. R. Shen, "Studies with crossed laser and molecular beams," *Physics Today,* vol. 33, no. 11, p. 52, 1980.

[92] P. N. Perera, K. R. Fega, C. Lawrence, E. J. Sundstrom, J. Tomlinson-Phillips, and D. Ben-Amotz, "Observation of water dangling OH bonds around dissolved nonpolar groups," *Proc Natl Acad Sci U S A,* vol. 106, no. 30, pp. 12230-4, Jul 28 2009.

[93] S. A. Corcelli and J. L. Skinner, "Infrared and Raman line shapes of dilute HOD in liquid H_2O and D_2O from 10 to 90 ^oC," *Journal of Physical Chemistry A,* vol. 109, no. 28, pp. 6154-6165, 2005.

[94] K. D. Kreuer, "On the development of proton conducting polymer membranes for hydrogen and methanol fuel cells," (in English), *Journal of Membrane Science,* vol. 185, no. 1, pp. 29-39, Apr 15 2001.

[95] S. S. Jang, V. Molinero, C. Tahir, and W. A. Goddard, "Nanophase-segregation and transport in Nafion 117 from molecular dynamics simulations: Effect of monomeric sequence," (in English), *Journal of Physical Chemistry B,* vol. 108, no. 10, pp. 3149-3157, Mar 11 2004.

[96] M. T. McDonnell and D. J. Keffer, "Intrinsic relationships between proton conductivity and nanopore size and functionalization," *Microporous and Mesoporous Materials,* vol. 177, pp. 17-24, 2013.

[97] R. Devanathan, "Recent developments in proton exchange membranes for fuel cells," *Energy & Environmental Science,* vol. 1, no. 1, pp. 101-119, 2008.

[98] J. Song, O. H. Han, and S. Han, "Nanometer-scale water- and proton-diffusion heterogeneities across water channels in polymer electrolyte membranes," *Angew Chem Int Ed Engl,* vol. 54, no. 12, pp. 3615-20, Mar 16 2015.

[99] A. Kusoglu, M. A. Modestino, A. Hexemer, R. A. Segalman, and A. Z. Weber, "Subsecond Morphological Changes in Nafion during Water Uptake Detected by Small-Angle X-ray Scattering," *ACS Macro Letters,* vol. 1, no. 1, pp. 33-36, 2012.

[100] K. A. Mauritz and R. B. Moore, "State of understanding of Nafion," *Chem. Rev.,* vol. 104, pp. 4535-4585, 2004.

[101] S. J. Paddison, R. Paul, and J. Thomas A. Zawodzinski, "A Statistical Mechanical Model of Proton and Water Transport in a Proton Exchange Membrane," *Journal of The Electrochemical Society,* vol. 147, no. 2, pp. 617-626, 2000.

[102] A. Vishnyakov and A. V. Neimark*, "Molecular Dynamics Simulation of Microstructure and Molecular Mobilities in Swollen
Nafion Membranes," *J. Phys. Chem. B* vol. 105, pp. 9586-9594, 2001.

[103] J.-J. J. Max and C. Chapados, "Isotope effects in liquid water by infrared spectroscopy," *The Journal of chemical physics,* vol. 116, p. 4626, 2002.

[104] SOLVAY. Aquivion® E87-05s perfluorosulfonic acid [Online].

[105] SOLVAY. Aquivion® E98-05 perfluorosulfonic acid [Online].

[106] Chemours. Nafion TM Ion Exchange Materials NE1035 [Online].

[107] J. E. Hensley, J. D. Way, S. F. Dec, and K. D. Abney, "The effects of thermal annealing on commercial Nafion® membranes," *Journal of Membrane Science,* vol. 298, no. 1-2, pp. 190-201, 2007.

[108] S. Izvekov and G. A. Voth, "Car-Parrinello molecular dynamics simulation of liquid water: New results," *Journal of Chemical Physics,* vol. 116, pp. 10372-10376, 2002.

[109] H. A. Every, M. A. Hickner, J. E. McGrath, and T. A. Zawodzinski, "An NMR study of methanol diffusion in polymer electrolyte fuel cell membranes," *Journal of Membrane Science,* vol. 250, pp. 183-188, 2005.

[110] T. A. Zawodzinski *et al.*, "Water Uptake by and Transport Through Nafion® 117 Membranes," *Journal of The Electrochemical Society,* vol. 140, p. 1041, 1993.

[111] L. Shen and Z. Chen, "Critical review of the impact of tortuosity on diffusion," *Chemical Engineering Science,* vol. 62, pp. 3748-3755, 2007.

[112] G. E. Walrafen, "Raman Spectral Studies of HDO in H2O," *The Journal of Chemical Physics,* vol. 48, no. 1, pp. 244-251, 1968.

[113] L. G. Longsworth, "The mutual diffusion of light and heavy water," *Journal of Physical Chemistry,* vol. 64, no. 12, pp. 1914-1917, 1960.

[114] R. Mills, "Self-diffusion in normal and heavy water in the range 1-45.deg.," *Journal of Physical Chemistry,* vol. 77, pp. 685-688, 1973.

[115] T. A. Ho, D. V. Papavassiliou, L. L. Lee, and A. Striolo, "Liquid water can slip on a hydrophilic surface.," *Proceedings of the National Academy of Sciences of the United States of America,* vol. 108, pp. 16170-5, 2011.

[116] C. Sendner, D. Horinek, L. Bocquet, and R. R. Netz, "Interfacial water at hydrophobic and hydrophilic surfaces: slip, viscosity, and diffusion," *Langmuir,* vol. 25, no. 18, pp. 10768-81, Sep 15 2009.

[117] N. C. Holmes, W. J. Nellis, W. B. Graham, and G.E.Walrafen, "Spontaneous Raman Scattering from Shocked Water," *Physical review letters,* vol. 55, pp. 20-23, 1985.

[118] A. Kalra, S. Garde, and G. Hummer, "Osmotic water transport through carbon nanotube membranes," *Proceedings of the National Academy of Sciences,* vol. 100, pp. 10175-10180, 2003.

[119] J. K. Holt *et al.*, "Fast Mass Transport Through Sub–2-Nanometer Carbon Nanotubes," *Science,* vol. 312, pp. 1034-1037, 2006.

[120] C. Ding, H. Zhang, X. Li, H. Zhang, C. Yao, and D. Shi, "Morphology and electrochemical properties of perfluorosulfonic acid ionomers for vanadium flow battery applications: effect of side-chain length," *ChemSusChem,* vol. 6, no. 7, pp. 1262-9, Jul 2013.

[121] A. Kusoglu, A. Hexemer, R. C. Jiang, C. S. Gittleman, and A. Z. Weber, "Effect of compression on PFSA-ionomer morphology and predicted conductivity changes," (in English), *Journal of Membrane Science,* vol. 421, pp. 283-291, Dec 1 2012.

[122] J. Karo, A. Aabloo, J. O. Thomas, and D. Brandell, "Molecular Dynamics Modeling of Proton Transport in Nafion and Hyflon Nanostructures," *J. Phys. Chem. B,* vol. 114, pp. 6056-6064, 2010.

[123] D. Brandell, J. Karo, A. Liivat, and J. O. Thomas, "Molecular dynamics studies of the Nafion, Dow and Aciplex fuel-cell polymer membrane systems," *J Mol Model,* vol. 13, no. 10, pp. 1039-46, Oct 2007.

[124] E. O. Potma, W. P. d. Boeij, P. J. M. v. Haastert, and D. A. Wiersma, "Real-time visualization of intracellular hydrodynamics in single living cells," *Proceedings of the National Academy of Sciences,* vol. 98, no. 4, pp. 1577-1582, 2001.

[125] Z. Q. Tian, B. Ren, and D. Y. Wu, "Surface-enhanced Raman scattering From noble to transition metals and from rough surfaces to ordered nanostructures," *Journal of Physical Chemistry B,* vol. 106, no. 37, pp. 9463-9483, 2002.

[126] M. Valtiner, K. Kristiansen, G. W. Greene, and J. N. Israelachvili, "Effect of surface roughness and electrostatic surface potentials on forces between dissimilar surfaces in aqueous solution," *Adv Mater,* vol. 23, no. 20, pp. 2294-9, May 24 2011.

[127] J. Zhao, H. Lui, D. I. McLean, and H. Zeng, "Automated Autofluorescence Background Subtraction Algorithm for Biomedical Raman Spectroscopy," *Applied Spectroscopy,* vol. 61, no. 11, pp. 1225-1232, 2007.

[128] G. Socrates, *Infrared and Raman Characteristic Group Frequencies: Tables and Charts*, Third ed. Wiley, 2004, p. 366.

[129] J. Israelachvili, *Intermolecular and surface forces*, Third Edition ed. Elsevier Academic Press, 2011.

[130] C. Eun and M. L. Berkowitz, "Origin of the hydration force: Water-mediated interaction between two hydrophilic plates," *Journal of Physical Chemistry B,* vol. 113, no. 40, pp. 13222-13228, 2009.

[131] M. Hermansson, "The DLVO theory in microbial adhesion," *Colloids and Surfaces B: Biointerfaces* vol. 14, no. 1-4, pp. 105–119, 1999.

[132] D. Wiley and G. F. Weihs, "Surface Charge Density," in *Encyclopedia of membranes*, E. Drioli and K. Giorno, Eds. Berlin, Hiedelberg: Springer, 2016.

[133] J. F. Smalley, K. Chalfant, S. W. Feldberg, T. M. Nahir, and E. F. Bowden, "An Indirect Laser-Induced Temperature Jump Determination of the Surface p K a of 11-Mercaptoundecanoic

Acid Monolayers Self-Assembled on Gold," *The Journal of Physical Chemistry B,* vol. 103, no. 10, pp. 1676-1685, 1999.

[134] M. C. Leopold, J. A. Black, and E. F. Bowden, "Influence of Gold Topography on Carboxylic Acid Terminated Self-Assembled Monolayers," *Langmuir 2005,* vol. 18, no. 4, pp. 978-980, 2002.

[135] C. D. Hatch, J. S. Wiese, C. C. Crane, K. J. Harris, H. G. Kloss, and J. Baltrusaitis, "Water adsorption on clay minerals as a function of relative humidity: application of BET and Freundlich adsorption models," *Langmuir,* vol. 28, no. 3, pp. 1790-803, Jan 24 2012.

[136] X. Luo, A. Wright, T. Weissbach, and S. Holdcroft, "Water permeation through anion exchange membranes," *Journal of Power Sources,* 2017.

[137] T. Mohammadi, S. C. Chieng, and M. Skyllas Kazacos, "Water transport study across commercial ion exchange membranes in the vanadium redox flow battery," *Journal of Membrane Science,* vol. 1997, no. 2, pp. 151-159, 1997.

[138] V. O. Mittal, H. Russell Kunz, and J. M. Fenton, "Is H2O2 Involved in the Membrane Degradation Mechanism in PEMFC?," *Electrochemical and Solid-State Letters,* vol. 9, no. 6, pp. A299-A302, 2006.

APPENDIX A

IGOR CODES FOR CCLS

```
#pragma rtGlobals=3		// Use modern global access method and strict wave access.
#include <Global Fit 2>
variable/G V_FitTol
V_FitTol=0.00001 //the global variables to set the tolerance to break the iteration.

Function getGfit(nC, epsi, paral, name,s_Ns)
string name
variable paral
variable s_Ns //s_Ns=1, process the raw spectra; s_Ns=2, process the Normalized spectra
variable nC, epsi //nC indicates the number of components;
variable nD //nD is the number of data spectra
variable i, j;
variable k;
variable points
NVAR V_FitTol=V_FitTol
	gettingData(name,s_ns)
	wave/T datasets1
	wave/T datasets2
	wave Wvpoints
	points=Wvpoints[0]
	wave Int_max
```

```
nD=(dimsize(datasets1,0))
make/o/n=(0,((points)+nC)) Fits //save the resultant coefs
make/o/n=(0,(nD*nC+(points))) matrixInitG //save the initial guess
for the coefs
//*****test wave:
FitFuncnames************************************//
make/o/T/n=3 FitFuncnames //a test wave containing a list of fit
functions: FfunN
        FitFuncnames[0]="Fit2D1"; //fit with 2 components of which
one component is deduced
        FitFuncnames[1]="Fit3D1";
        FitFuncnames[2]="Fit4D1";
//***** test wave: Datasets
************************************//
        nD=(dimsize(datasets1,0))
        make/T/o/n=(nD,2) datasets
        string tdatasets
        tdatasets="datasets"+num2str(S_NS)
        wave/T w01=$(tdatasets)
                Datasets[][0]= w01[p]
                Datasets[][1]= "_calculated_"
//*****wave Coefdatasetlinkage:
***********************************//
        SetDimLabel 1,0,'f()',coefdatasetlinkage // 1=col, 0 or 1 = No
of Col, string=label, wavename
        SetDimLabel 1,1,first,coefdatasetlinkage
        SetDimLabel 1,2,last,coefdatasetlinkage
        SetDimLabel 1,3,N,coefdatasetlinkage
        Coefdatasetlinkage[][0]=(nC-2) // 0 = R0 in fitFuncnames,
which is Fit2D1, points+2 coef
        for (i=0;i<2;i+=1)
                for(j=0; j<nD; j+=1)
                Coefdatasetlinkage[j][i+1]=((points-1))*(i+j)+j
```

```
		endfor
	endfor
	Coefdatasetlinkage[][3]=(points)+nC//numbers of coef.
	variable LinkC;	//linkC is the col number in the Coefdatasetlinkage.
	linkC=(dimsize(Coefdatasetlinkage,1));

		for(i=4;i<linkC;i+=1)
			Coefdatasetlinkage[0][i]=i-4
		endfor
	for(j=0;j<nC;j+=1

		for (i=1; i<nD;i+=1)
			Coefdatasetlinkage[i][j+4]=linkC-4+(i-1)*nC+j
		endfor
	endfor
	for (j=(4+nC); j<linkC;j+=1)
		for (i=1; i<nD; i+=1)

	Coefdatasetlinkage[i][j]=Coefdatasetlinkage[0][j]
				endfor
	endfor
	Get_initalG_Weights(nC, nD)
	wave iniGW, iniGspec1
	wave bulk
	k=(nC*nD+(points))
	//****test wave: coefNames
	 make/o/t/n=(k) coefNames
	//*****test wave: constraintwave,
	make/o/T/n=(0)	ConstraintWave	//the non-negative constraints, K>0, a TEXT wave
		string strConstraint
		string strSum
```

```
        string tempstr
if (nC<=4)
    for(i=0;i<nC;i+=1)
        strConstraint="K"+num2str(i)+" >="+" 0"
        insertpoints/M=0 (DimSize(constraintwave,0)),1,
constraintwave
        constraintwave[DimSize(constraintwave,0)-
1][]=strConstraint
        strConstraint="K"+num2str(i)+"
<="+num2str(Int_max[0]^(abs(S_NS-2)))
        insertpoints/M=0 (DimSize(constraintwave,0)),1,
constraintwave
        constraintwave[DimSize(constraintwave,0)-
1][]=strConstraint
    endfor
for(i=nC;i<((points+nC-1));i+=1)
    strConstraint="K"+num2str(i)+" >="+" 0"
    insertpoints/M=0 (DimSize(constraintwave,0)),1,
constraintwave
    constraintwave[DimSize(constraintwave,0)-1][]=strConstraint

endfor
for (i=0;i<(nD-1);i+=1) //nD: Numbers of spectra -1
    for(j=0;j<nC;j+=1) //nC: numbers of components
        strConstraint="K"+num2str(nC+points+i*nC+j)+"
>="+" 0"
         insertpoints/M=0 (DimSize(constraintwave,0)),1,
constraintwave
        constraintwave[DimSize(constraintwave,0)-
1][]=strConstraint
        strConstraint="K"+num2str(nC+points+i*nC+j)+"
<="+" 1"
```

```
                insertpoints/M=0        (DimSize(constraintwave,0)),1,
constraintwave
                constraintwave[DimSize(constraintwave,0)-
1][]=strConstraint
        endfor
endfor
        elseif (nC>4)
                for (j=0;j<(nC-1);j+=1) //constraint the non-negativity:
K0, K1, K2 are non-negative
                        strConstraint="K"+num2str(j)+" >="+" 0"
                        insertpoints/M=0
(DimSize(constraintwave,0)),1, constraintwave
                        constraintwave[DimSize(constraintwave,0)-
1][]=strConstraint

                        strConstraint="K"+num2str(j)+"
<="+num2str(Int_max[0]^(abs(S_NS-2)))
                        insertpoints/M=0
(DimSize(constraintwave,0)),1, constraintwave
                        constraintwave[DimSize(constraintwave,0)-
1][]=strConstraint
                endfor
        endif
        make/o/T=1 Strwave
                for (i=0;i<nC;i+=1) //Sum of Fit weights from
spectrum 1
                        Strconstraint = "K"+num2str(0)
                        StrConstraint+="+ K"+num2str(i)
                endfor
                StrWave=Strconstraint + ">=0"               //non-
negative
                insertpoints/M=0        (DimSize(constraintwave,0)),1,
constraintwave
```

```
                constraintwave[DimSize(constraintwave,0)-
1][]=strwave
                StrWave=StrConstraint+"<=1" //sum is smaller than 1
                insertpoints/M=0        (DimSize(constraintwave,0)),1,
constraintwave
                constraintwave[DimSize(constraintwave,0)-
1][]=strWave
        variable nn
                for (i=0;i<(nD-1);i+=1)
                        for(nn=0;nn<nC;nn+=1)
                        Strconstraint = "K"+num2str((points)+0+i*nC)
                        StrConstraint+="+
K"+num2str(nC+(points)+nn+i*nC)
                        endfor
                        StrWave=Strconstraint + ">=0"
        //non-negative
                        insertpoints/M=0
(DimSize(constraintwave,0)),1, constraintwave
                        constraintwave[DimSize(constraintwave,0)-
1][]=strWave
                        StrWave=StrConstraint+"<=1" //sum is smaller
than 1
                         insertpoints/M=0
(DimSize(constraintwave,0)),1, constraintwave
                        constraintwave[DimSize(constraintwave,0)-
1][]=strWave
                endfor
//*****Coefwave, initial
guesses************************************//
        variable do1
        do1=0;
        for (do1=0;do1<paral;do1+=1)        //***** paral: # of initial
guess
```

```
make/o/n=(k,2) Coefwave
variable in1
Coefwave[0][0]=(0.6+enoise(0.1))
        for (j=1;j<nC;j+=1)
                Coefwave[j][0]=(1-Coefwave[0][0])/(nC-1)
        endfor
        for (in1=0;in1<(nD-1);in1+=1)
                for (i=0;i<nC;i+=1)

        Coefwave[nC+(points)+in1*nC+i][0]=Coefwave[i][0]
                endfor
        endfor
        //****specify the inital guess of the unkown component
spectrum with random values
        for (i=nC;i<((points)+nC);i+=1) //227 is the spectral points
                Coefwave[i][0]=0.01+(enoise(0.01))
        endfor
        SetDimLabel 1,1,Epsilon,Coefwave
        Coefwave[][1]=epsi
        make/o/n=((points)+nD*nC) InitalGuess
        duplicate/o/r=[0,((points)+nD*nC)][0] coefwave testG
        InitalGuess=testG[p][0]
         insertpoints/M=0 (DimSize(matrixInitG,0)),1, matrixInitG
         matrixInitG[DimSize(matrixInitG,0)-1][]=initalGuess[q]
        string errorName, En
        En = "En";
        string errorMessage, Em
        Em = "Em";
        variable maxIters
        string resultWavePrefix, RsltP
        RsltP="RsltP";
DoNewGlobalFit(FitFuncNames, DataSets, CoefDataSetLinkage,
CoefWave, coefNames, ConstraintWave,31, (points),1)
```

```
          string teststr="Coef_"+w01[0]
          wave Coef_test=$(teststr)
endfor
killwaves testG, initalGuess
End
Function gettingData(name, s_Ns)
          string name
          variable s_Ns
          String list;
          String theWave;
          list = Wavelist(name+"*",";","")
          variable i,j,numWaves;
          i=0;
          j=0;
          make/o/T/n=0 datasets1
          make/o/T/n=0 datasets2
          make/o/n=0 Wvpoints
          make/o/D/n=1 Int_Max, Int_temp
          Int_Max=0
          do
          theWave = StringFromList(i, list)
          insertpoints/M=0 (DimSize(datasets1,0)),1, datasets1
          datasets1[(DimSize(datasets1,0)-1)]= theWave
          if (strlen(theWave) == 0)
                    break
          endif
                    wave datawave=$(thewave)
                    insertpoints/M=0 (DimSize(Wvpoints,0)),1, Wvpoints
                    Wvpoints[(DimSize(Wvpoints,0)-1)]=
          (dimsize(datawave,0))
                    if(s_ns==2) //normalize the peak area to 1
                    string wName
                    wName="N"+thewave
```

```
                insertpoints/M=0 (DimSize(datasets2,0)),1, datasets2
                datasets2[(DimSize(datasets2,0)-1)]= wName

                make/o/n=(dimsize(datawave,0)) $wName

                wavestats/Q datawave
                wave w01=$wName
                w01=datawave/V_sum
                endif
                                                i+= 1
                j+=1
        while (1)                                       //      Loop
until break above
killwaves Int_temp
DeletePoints j,1, datasets1
End
```

Function Get_initalG_spec(spec1, bulk)

```
//*****inital guess for spectral component: IniGSpec****//
        wave spec1//1 spec from the batch data sets
        wave bulk// 1 known components
        duplicate/o spec1, rsd1, fit1
        Make/D/N=1/O W_coef //No. coefs
        Make/O/T/N=1 T_Constraints //No. constraints
                T_Constraints[0] = {"K0 > 0"} //the coeficient should
be non-negtive                                  W_coef[0] = {0.5}
                FuncFit/Q/NTHR=0  FitwithONEwave  W_coef  spec1
/X=bulk /D
         fit1=W_coef[0]*bulk[p]
        rsd1=spec1-fit1
        duplicate/o rsd1 test
        variable i
        for (i=0;i<(dimsize(rsd1,0)); i+=1)
                if (rsd1[i]>=0)
```

```
        test[i]=0
        elseif (rsd1[i]<0)
        test[i]=abs(rsd1[i])
        endif
    endfor
    variable ptest,ratio
    wavestats/q test
    ptest=x2pnt(test,V_maxloc)
    ratio=(spec1[ptest])/(fit1[ptest])
    fit1=fit1[p]*ratio
    rsd1=abs(spec1-fit1)
    duplicate/o rsd1 iniGSpec //IniGspec is the initial guess for the deduced components
    killwaves test, rsd1, fit1
End
```

```
Function Get_initalG_Weights(nC, nD)
    //*****initial guess for lstsqrfitting weights: IniGW****
    variable nC, nD //nC is the number of components, and nD is the number of data spectra
    variable i,noW;
    noW=(nC*nD);
    make/o/n=(noW) IniGW
    for (i=0;i<noW;i+=1)
        IniGW=500*abs(enoise(1,1)) //give non-negative random values to the test, 0<=test<=1
    endfor
End
```

```
Function Fit2D1(w,x) : FitFunc
    Wave w
    variable x
    wave bulk = root:blk
    variable point
    point = x2pnt(bulk,x)
```

```
		wave Nb = root:Wvpoints
		variable points
		points = Nb[0]
	wavestats/Q/R=[2,(points+1)] w
	return w[0]*bulk[point]*v_sum+w[1]*w[point+2]
End
```

Function Fit3D1(w,x) : FitFunc

```
	Wave w
	variable x
	wave bulk01 = root:bulk		//should be changed according to
the know components
	duplicate/o bulk01 bulk
	wavestats/Q bulk
	bulk/=V_sum
	duplicate/o dry01 dry
	wavestats/Q dry01
	dry/=V_sum
	variable point
		wave Nb = root:Wvpoints
		point = x2pnt(bulk,x)
		variable points
	points=Nb[0]
	//wavestats/Q/R=[3,229] w	//for oh region
	//return
w[0]*bulk[point]*v_sum+w[1]*dry[point]*v_sum+w[2]*w[point+3]
		wavestats/Q/R=[3,((points)+2)] w	//for od region
	return
w[0]*bulk[point]*V_sum+w[1]*dry[point]*v_sum+w[2]*w[point+3]
	End
```

Function Fit4D1(w,x) : FitFunc

```
	Wave w
	variable x
```

```
    wave bulk = root:blk
    wave dry = root:nonblk
    wave HOD = root:mix
    variable point
        bulk[0,229]=0
    wavestats/Q bulk
    bulk/=V_sum
        dry[219,394]=0
    wavestats/Q dry
    dry/=V_sum
        point = x2pnt(bulk,x)
        duplicate/o/R=[4,(dimsize(bulk,0))+3] w testspec
    testspec=abs(testspec)
    wavestats/Q testspec
    return w[0]*bulk[point]+w[1]*dry[point]+
w[2]*HOD[point]+w[3]*w[point+4]/V_sum
    End
```

SUMMARY

A well-operated proton exchange membrane fuel cell (PEMFC) requires an optimized water management system wherein the proton is efficiently transported in the proton exchange membrane (PEM) of the FC and the flooding at the cathode of the FC is avoided. The water transport in PEM plays a crucial role in the water management that greatly affects the performance of the PEMFC. Fast water transport (driven by the electro-osmotic drag) in the PEM from the anode of the PEMFC to cathode is required because it is closely related to the proton transport in the PEM; meanwhile, fast water transport driven by the concentration gradient from the cathode to the anode of the PEMFC can suppress or even prevent the flooding at the cathode. A PEM manifesting outstandingly faster water transport property is required, and knowing how the membrane structure determines the water transport is crucial for designing such a PEM.

In Chapter 4 of my thesis, we have studied the water structure in the hydrated proton exchange membranes. Two industry-standard commercial Nafion® membranes, Nafion® 212 (N212) and Nafion® 117 (N117), were studied. We spectrally distinguished the water subspecies in the Nafion® membranes and quantified the fractional contribution of each water subspecies. There are two types of water subspecies in the PEMs: 1) bulk water (bulkW) that hydrogen bonds to other surrounding water molecules and 2) nonbulk water (nonbulkW) that interacts strongly with the membrane structure. We found that the N117 has a larger amount of nonbulkW, exhibits a larger proton conductivity, and has a larger water mobility N212. The additional amount of the nonbulkW in N117 results from a modified nanoscale structure of the PEM where the ionic domains have a larger surface-to-volume ratio and a larger hydrophilic head group spacing compared to N212.

In Chapter 5, the diffusivity of the bulkW and the nonbulkW in Nafion® membranes were experimentally quantified in five different PEMs. We found that the diffusivity of the nonbulkW is 2.5-fold faster than the bulkW in all PEMs with different ratio between ADC(nonbulkW) and ADC(bulkW), depending both polymer chemistry. Interestingly, the overall water diffusivity in all membranes could be represented by a linear combination of the water subspecies weighted by the fractional contributions. Based on the results of Chapter 5, a clear design target for membrane manufacturing is provided: maximize the nonbulkW.

In Chapter 6, I established a model surface system to mimic the surface of the nanoscale water channels in Nafion® membranes. The concentration of the sulfonic acid groups in the surface was varied and the interactions between the water structure and these surfaces in acid solutions (HCl, pH =1) has been studied by AFM. The structure of water on the different surfaces at the molecular level was discussed.

As the final part of the thesis, Chapter 7 ideas for a modified flow cell design with which one could measure the water diffusivity in the membrane at different hydration states. Preliminary results of water diffusivity in different anion exchange membranes were shown showing that the CARS platform can be used to probe the water transport of different materials. Considering the experimental accessibility of the experimental and analytical platform, this is a powerful method to produce reliable results and compare the water transport properties of different membrane materials. Last but not least, I suggested using the vibrational Raman scattering spectroscopy to study the degradation of the PEMs in PEMFCs and provide a clear design target for making a PEM that sustain substantially long in the PEMFC.

SAMENVATTING

Een goed-functionerende protonuitwisselingsmembraanbrandstofcel (PEMFC) heeft een geoptimeerd watermanagementsysteem nodig waarin het proton efficiënt getransporteerd wordt in het protonuitwisselingsmembraan (PEM) van de brandstofcel en overstroming aan de kathode van de brandstofcel vermeden wordt. Het watertransport in het PEM speelt een cruciale rol in het watermanagement dat de prestatie van de PEMFC in grote mate beïnvloedt. Snel watertransport (aangedreven door de elektro-osmotische aantrekkingskracht) in het PEM van de anode van de PEMFC tot de kathode is nodig omdat het sterk gerelateerd is aan het protontransport in het PEM; tegelijkertijd kan snel watertransport aangedreven door de concentratiegradiënt van de kathode naar de anode van de PEMFC de overstroming aan de kathode onderdrukken of zelfs tegengaan. Een PEM met een sterk snellere watertransporteigenschap is benodigd, en de wetenschap hoe de membraanstructuur het watertransport bepaalt is cruciaal om zo'n PEM te ontwerpen.

In hoofdstuk 4 van mijn proefschrift hebben we de waterstructuur in gehydrateerde protonuitwisselingsmembranen bestudeerd. Twee industriestandaard commerciële Nafion® membranen, Nafion® 212 (N212) en Nafion® 117 (N117), werden bestudeerd. We hebben de waterondersoorten in de Nafion membranen spectroscopisch onderscheiden en de fractionele contributie van elke waterondersoort gekwantificeerd. Er zijn twee soorten water ondersoorten in de protonuitwisselingsmembranen: 1) bulk water (bulkW) dat waterstofbruggen vormt met andere omliggende watermoleculen en 2) niet-bulk water (niet-bulkW) dat sterk met de membraanstructuur interacteert. We hebben gevonden dat N117 een grotere hoeveelheid niet-bulkW heeft, een grotere protongeleidbaarheid laten zien en een grotere watermobiliteit. De toegevoegde hoeveelheid niet-bulkW in N117 is het resultaat van een gemodificeerde nanoschaalstructuur van het PEM waar de ionische domeinen een grotere oppervlakte-tot-volume verhouding en een grotere hydrofiele kopgroep tussenruimte in vergelijking met N212 hebben.

In hoofdstuk 5 werden de diffusiviteit van het bulkW en het niet-bulkW in Nafion membranen experimenteel gekwantificeerd in 5 verschillende protonuitwisselingsmembranen. We hebben gevonden dat de diffusiviteit van het niet-bulkW 2,5 keer sneller is dan het bulkW in alle protonuitwisselingsmembranen met een verschillende verhouding tussen de waargenomen diffusiecoëfficiënt (ADC) van niet-bulkW en bulkW, afhankelijk van polymeerchemie. Interessant is dat de globale waterdiffusiviteit in alle membranen gepresenteerd wordt door een lineaire combinatie van de waterondersoorten gewogen door hun fractionele contributies. Gebaseerd op de resultaten van hoofdstuk 5 wordt een duidelijk ontwerpdoel voor membraanproductie geboden: maximaliseer het niet-bulkW.

In hoofdstuk 6 heb ik een model oppervlaktesysteem tot stand gebracht om de oppervlakte van de nanoschaal waterkanalen in Nafionmembranen na te bootsen. De concentratie van sulfonzuurgroepen op de oppervlakte werd gevarieerd en de interactie tussen de waterstructuur en deze oppervlakten in zure oplossingen (HCl, pH = 1) werd bestudeerd met atoomkrachtmicroscopie (AFM). De structuur van water op de verschillende oppervlakten op de moleculaire schaal werd besproken.

In het laatste deel van het proefschrift, hoofdstuk 7, worden ideeën voor een gemodificeerd stromingscelontwerp waarmee de waterdiffusiviteit in het membraan bij verschillende hydratatiestaten gemeten kan worden. Voorlopige resultaten van waterdiffusiteit in verschillende anionuitwisselingsmembranen werden gepresenteerd die laten zien dat het CARS-platform gebruikt kan worden om het watertransport van verschillende materialen te onderzoeken. Wat de experimentele toegankelijkheid van dit experimentele en analytische platform betreft is dit een krachtige methode om betrouwbare resultaten te produceren en de watertransporteigenschappen van verschillende membraanmaterialen te vergelijken. Tenslotte stel ik voor om vibrationele Raman verstrooiingsspectroscopie te gebruiken om de degradatie van protonuitwisselingsmembranen in protonuitwisselingsmembraanbrandstofcellen te bestuderen en biedt een duidelijk ontwerpdoel om een PEM te maken dat substantieel langer standhoudt in een PEMFC.

ACKNOWLEDGEMENTS

It is a pleasure to thank those who made this thesis possible. I would like to thank the people below who have assisted to cherish my goal.

I would like to thank my supervisors. Katrin: thank you for giving me the opportunity to work on this project. You made me know that critical thinking is very important for a scientist, and encouraged me to criticize my work. Sapun: I lack words with which to express my thanks. I learned from you how to be critical and be respectful at the same time. You were very patient with me, and always tried to help. You taught me how to conduct myself as a professional. I always remind of what you said to me, “Xiao, you should behave as an adult”, whenever I meet tough issues. I feel very lucky to have you as my supervisor.

I want to express my gratitude to Mischa and the entire AK-Bonn department. Thank you all for providing such a nice department and assisting me in my project. Marc-Jan and Florian, thanks for designing all the magic devices and making my research life much easier. Laurie, I really appreciate all the support and help. Yuki, I admire you for your rigorous attitude towards science and your enthusiasm of hot pot. I cherish the advices and the encouragement from you these years.

I also would like to thank Rüdiger, Uwe and Doris from AK-Butt department, and to thank Anke from AK-Landfest department for all the technical and scientific supports. Along with the people from MPIP, I would like to thank Paola, Wolfgang and Masia for hosting me at Cardiff. Markus and Laila, it was nice to collaborate with you.

I am deeply grateful to the TERS group. Philipp, it was a pleasure and an honor to be your office mate. We followed the development of each other and I am so happy we both have survived. Amala, thank you for being my listener and supporter. Just keep in mind: do not feel scared; I am always here to help and support you. Leonie, I admire your rigorous attitude at experiments. It was always nice to talk with you about work and life. Natalia, thank you very much for you encouragement and help. I will treasure the time we spend together in the EC-lab. Ulmas: I would like to thank you for the discussions and helps. Jonas, thank you for your warm smile and being nice to me. Walter and Gabi, thanks for providing all the technical support. It was great spending time with you and learning from you.

It was an honor being part of the CARS group. Samet, thank you for training me to use the micro-Raman and assisting me in preparing samples. Nils and Will, thank you for guiding me to “drive” CARS and the effort on teaching me use Igor Pro. Mischa: I appreciated the comments from you. I bet you will become a “big” Mischa too. Sabine, it was nice to have you in the group. Frederik, thank you for being the friend, the critic, and the “nanny” of me these years. Yujen, I admire you for your ability of adapting to a new environment and thank you so much for the tasty food.

I own my special gratitude to all my friends from the FINON INT, Alexandra, Steffi, Amala, Diana, Michael, Juris, Carolina, Attilio, Naya, Marie, Alberto, Vitalijs and Siyuan. We become so strong and so united that nothing can beat us. Juris, I miss you so much.

I would like to thank all my Chinese friends at AK-Bonn. We went for lunch together and talked about almost everything including work, food and gossips. Qianli, thank you for spoon-feeding me the survival skills in Europe and giving me confidence to keep on going. Zuanming, thank you for showing me how to “look up to the sky and come down to earth”. Your optimistic attitude towards life definitely have had a very positive impact on my life. Liping, I appreciate you highly recommended many things to me which makes my life much easier. Xiaoming, thank you for teaching me swim and encouraging me to try new things. Hao, thank you for all the advices on how to improve my work and how to be mature. Peng, Shumei and Fujie, it was great to have you as my friends.

To 1222 (Linmei Liu, Shanshan Cai, Ruidong Liu, Jia Yang and Qiong Wu): Thank you for being my backup. The distance between China and any other country deepen the friendship between us. I feel lucky to have you. Along with 1222, I would like to express my appreciation to Chuankun Jia, Yuanhang Cheng, Wenyue Li and Yong Guan. I am looking forward to hosting another round-table meeting in the future.

Finally, I would like to thank my family, Zhantian, Leyun, Cheng and Dafang. Thank you for being supportive. Mum, although we have a conflict between what you expect from me and what I want, we still love each other. Dad, keep on being a happy-go-lucky man. Cheng, thank you for being the unique sister who understand me. Dafang, I think you should be the member of my family because you are my “da ma”. Thank you for being my friend these years and tracking the change of me.